INVESTIGATING OPTICAL ATOM TRAPS FOR BOSE-EINSTEIN CONDENSATE

By

PEYMAN AHMADI

Bachelor of Science
TABRIZ University
Tabriz, Iran
1996

Master of Science
Institute for Advanced Studies in Basic Science
Zanjan, Iran
1998

Submitted to the Faculty of the
Graduate College of the
Oklahoma State University
in partial fulfillment of
the requirements for
the Degree of
DOCTOR OF PHILOSOPHY
July, 2006

INVESTIGATING OPTICAL ATOM TRAPS FOR BOSE-EINSTEIN CONDENSATE

Thesis Approved:

Dr. Gil S. Summy

Thesis Advisor

Dr. Timothy M. Wilson

Dr. Paul A. Westhaus

Dr. Albert T. Rosenberger

Dr. Eric Abraham

Dr. Nicholas F. Materer

Dr. A. Gordon Emslie

Dean of the Graduate College

ACKNOWLEDGMENTS

It is a complicated feeling now that I finally completed my P.h.D work and am ready to enter a new phase of my life. It marks 5 years of my life being at OSU. The completion of this work would have not been possible without the encouragement and support of a number of people whom I was fortunate to know. I feel fortunate to have all of these people in my life. I sincerely appreciate their support and guidance over the years and wish to acknowledge their efforts for making my stay at OSU a remarkable memory.

My great thanks is to my advisor Dr. Gil Summy. He has provided me with endless technical and professional advise throughout my studies at OSU. The change from theoretical to experimental physics would have not been possible for me without the friendly atmosphere created by him in the lab. His knowledge has provided me with an education that goes far beyond atomic physics. I greatly appreciate his moral and financial support.

I would like to acknowledge the contribution of my dissertation committee members which includes: Dr. T.M. Wilson , Dr. A.T. Rosenberger, Dr. P. Westhaus, Dr. N. Materer, and specially Dr. E. Abraham from University of Oklahoma, whom has accepted the tiring task of driving from Norman.

Additionally, I want to thank the remaining faculty of the department of Physics for their individual contributions to my education. I would especially like to express my gratitude to Dr. Paul Westhaus who is always there to help us.

My colleagues in the basement tolerated my interruptions, have made my days in the lab happy and productive. I would like to thank Brian Timmons a knowledgable coworker whom instructed me through all the technical aspects of the instruments

and helped me to get a quick start at the beginning of my work. I want to thank Ghazal Behinaein and Vijayashankar Ramareddy that have worked with me in the lab. Each of them has contributed in some way to my education and this dissertation, it has been my privilege to work with them.

Also, I want to thank the department's staff members for their assistance during my time at OSU. Susan, Cindi and Stephanie have always been welcoming and patient with our never ending requests. We were also fortunate to have a skilled group of machinists in the instrument shop in the physics department at OSU lead by Mike Lucas. I appreciate the patient assistance provided by them while we were constructing our lab.

I want to especially thank my wife Ghazal. She has been an endless source of love and support. I am very proud of her for pursuing her doctorate degree in physics and working in the same field as I, lucky me! I hope I can be as supportive of her as she has been of me. Finally, I must thank my family. My parents encouraged me to pursue my education early on. I am glad I listened. Their perseverance and optimism were qualities I was fortune enough to inherit. Their absence has been hard to bare, but their love has always been with me. I am proud to dedicate this thesis to my wife and family.

TABLE OF CONTENTS

LIST OF FIGURES

CHAPTER 1

INTRODUCTION

In the history of science there are few people who were able to make a revolutionary change in our understanding of nature. Einstein is a man to whom physics owes much. One can hardly find an area of physics that has not benefited from his revolutionary ideas. One of the best known predictions made by him is Bose - Einstein condensation (BEC). Realization of BEC has became a great goal for physicists, worthy of the Nobel prize from the beginning.

The story starts when early attempts to calculate the Black body spectrum using classical statistical mechanics had failed, resulting in the catastrophe of the Rayleigh-Jeans law. In 1924 Satyendranath Bose found the correct way to evaluate the distribution of identical particles (such as Plancks radiation quanta) that allowed him to calculate the Planck spectrum using the method of statistical mechanics [1]. Einstein generalized Bose's new idea to identical particles with discrete energies. The result was Bose-Einstein (BE) statistical mechanics. The BE distribution is

$$N(E) = 1/(\exp(\beta(E-\mu)) - 1), \tag{1.1}$$

where $\beta = 1/\mathrm{k_B T}$, E is the energy of the particle and μ the chemical potential. Einstein applied the new concept of Bose statistics to an ideal sample of atoms or molecules that were at thermal equilibrium and trapped in a box. Based on this model he predicted that at sufficiently low temperatures the particles would accumulate in the lowest quantum state in the box, giving rise to a new state of matter with many unusual properties [2,3]. Conceptually, the effects of quantum statistics (which arise from the indistinguishability of the particles) arises if the mean inter-particle distance

$(V/N)^{1/3}$, where V is the volume of the system, in the system is comparable to the mean thermal wavelength of the particles λ_{dB},

$$\frac{V}{N} \approx \lambda_{dB}^3,$$

or $n\lambda_{dB}^3 \approx 1$, which is refered as the "phase space density" - the number of atoms within a volume λ_{dB}^3. The process of increasing the phase space to orders of unity is what we know today as Bose-Einstein condensation. An excellent review of the theoretical development of BEC is given by Griffin [4]. It took nearly 70 years for experimentalists to overcome various technical difficulties before BEC could emerge. The following list highlights some of the main breakthroughs of the field.

1) 1985: Migdall *et al.*, [5] demonstrated the idea of the magnetic trap.

2) 1986: Chu *et al.*, [6] demonstrated the first optically confined atoms.

3) 1987: First magneto optical trap (MOT) was realized [7] .

4) 1990: Successful loading of magnetic traps from a MOT [8] .

5) 1994: Successful demonstration of rf evaporative cooling [9,10].

6) 1995: Time Orbiting Potential (TOP) trap is demonstrated [11].

7) 1995: First observation of BEC.

It was in 1995 that Eric Cornell, Carl Wieman [12] and co-workers at JILA in a remarkable series of experiments produced BEC in a dilute gas of Rubidium atoms using a TOP trap. Shortly thereafter Wolfgang Ketterle [13] and co-workers at MIT created a BEC in sodium atoms also in a magnetic trap. An interesting review of the historical development of laser cooling and the achievement of BEC can be found in review articles by Phillips [14] and Cornell *et al.*,[15].

In a different approach, all-optical methods of reaching the BEC phase transition have been pursued since the early days of laser cooling. Despite many impressive developments beyond the limits set by Doppler cooling, including polarization gradient cooling [16], velocity selective coherent population trapping [17], Raman cooling [18–20], and evaporative cooling in optical dipole traps [21–25], the best results for phase space density was a factor of 10 away from the BEC transition [24,25]. Hence optical traps

have played only an auxillary role in BEC experiments. The MIT group used a magnetic trap with an optical dipole to reversibly condense a magnetically confined cloud of atoms restoratively cooled to just above the BEC transition [26]. Additionally, Bose condensates created in magnetic traps have been successfully transferred to shallow optical traps for further studies [27–30]. However, it was Chapman's group at Georgia Tech. that announced the first observation of a BEC using all optical methods in 2001 [31]. Soon after the Grimms' group at Innsbruck condensed Cesium atoms using all optical methods [32]. More recently, invention of the compressible crossed dipole trap technique [33] for creating BEC has streamlined achieving BEC using all-optical techniques. Overall Bose-Einstein condensation has been realized by more than 50 groups around the word now and promises to revolutionize many areas of physics.

1.1 Organization

The following chapters describe the first work carried out in the BEC laboratory at Oklahoma State University. The main goal of the research was to create Bose-Einstein condensate of Rb87 atoms using an all optical method. To achieve this goal it was necessary to develop a strong understanding of laser cooling and trapping techniques of neutral atoms in addition to constructing the experimental apparatus. Having this in mind the dissertation is organized in the following way.

In Chapter 2 a review of the physics of laser cooling and trapping of neutral atoms is presented. The theory behind the magneto-optical trap and evaporative cooling will also be explained. The theoretical concepts of noninteracting Bosons will be reviewed in Chapter 3. Here the thermodynamic properties of a BEC in an external harmonic trap and its experimental relevance will be discussed. The chapter ends by reviewing the properties of an interacting Bosonic system.

Chapter 4 is dedicated to a detailed discussion of the technical aspects of the experimental set up. This includes a discussion on the vacuum chamber and the optical system. The chapter continuous by describing the stabilization of the diode

lasers and a description of the dipole trap and how it can be realized. The chapter concludes with the observation of the BEC using the designed experimental apparatus.

Chapter 5 is dedicated to presenting a study on the loading of optical traps. It starts by introducing a theoretical model which is followed by an experimental investigation. Based on this study the concept of time averaged optical traps is introduced. The conclusion is that the time averaged traps can be used to reduce the problem of low efficiency of dipole trap loading.

In Chapter 6 a new method to tailor the trap shape is demonstrated. The chapter starts by showing that spherical aberration can alter the potential shape near the focus of a lens. The new pattern for the beam is such that it produces local intensity minima along the propagation direction capable of trapping atoms. In the remander of this chapter the experimental results of loading these local minima will be presented. The chapter concludes with proposals for several applications for spherical aberration micro-optical traps.

CHAPTER 2

TECHNIQUES TO COOL AND TRAP NEUTRAL ATOMS

This chapter is dedicated to explaining the theoretical details of our approach to realize a Bose-Einstein condensate. In general, the following steps are the " ABC " of making a BEC,

A) preparing a source of cold atoms,

B) loading atoms into a magnetic or far-off-resonant optical trap,

C) Selectively removing the atoms with high energies to reduce the trapped cloud's temperature.

For step A almost all of the research groups use a magneto-optical trap (MOT)[7]. This trap utilizes a clever combination of magnetic fields and laser light to trap and cool the atoms. However, there are limits on the lowest temperature and highest phase space densities achievable with a MOT and these are far away from the conditions necessary to realize a BEC. Step B and C should be taken to break these limits and achieve the BEC transition. There are two different approaches to step B. In one method a magnetic trap and in another one a far-off-resonant-optical trap (FORT) is used. Both share the advantage that they do not have any near resonant laser beam to heat the atoms via spontaneous emission. We have used the second method and therefore will study it through the rest of this thesis.

It is clear by glancing through steps A, B and C that having a knowledge of light-matter interactions is important. Therefore, we start this chapter by reviewing the concepts of laser cooling followed by a simple explanation of the working principles of a MOT. Finally we study step C in Section 3.

2.1 Concepts of Laser cooling

The idea of cooling neutral atoms using an off-resonant laser beam was introduced by Hänsch and Schawlow [34] in 1975. They showed that a low-density gas can be cooled by illuminating it with intense, quasi-monochromatic light tuned to the low-frequency side of a resonance line. To understand this process let us consider the situation of a two level atom interacting with an electromagnetic wave. The force on the atom is defined as the expectation value of the quantum mechanical force operator [35],

$$\hat{F} = -\frac{\partial \hat{H}}{\partial z}. \tag{2.1}$$

Where $\hat{H}$ is the Hamiltonian. The expectation value of this operator on an ensemble of atoms is given by,

$$< \hat{F} >= Tr(\hat{\rho}\hat{F}). \tag{2.2}$$

Where $\hat{\rho}$ is the density matrix and its time evolution is given by,

$$\frac{d\hat{\rho}}{dt} = -\frac{i}{\hbar}[\hat{H}, \hat{\rho}]. \tag{2.3}$$

Therefore we need to determine the Hamiltonian, $\hat{H}$, before explicitly calculating the force on the atoms by the laser field. Our starting point towards this goal is the Schrödinger equation,

$$(i\hbar\frac{\partial}{\partial t} - \hat{H})\Psi = 0, \tag{2.4}$$

where,

$$\hat{H} = \hat{H}_{rad} + \frac{\sum_{j=1}^{jmax}[\hat{p}_j + \frac{e_j}{c}A(R_j)]^2}{2m_j} + \sum_{j=1}^{jmax} V(R_1, ..., R_{jmax}), \tag{2.5}$$

where p is the particle's momentum, A is the magnetic vector potential and V is the particle-particle interaction potential. The first term is the energy operator of the noninteracting electromagnetic field,

$$\hat{H}_{rad} = \sum_{k,\lambda} \hbar\omega_k a^{\dagger}_{k,\lambda} a_{k,\lambda},$$

where the sum is over a complete set of the electromagnetic creation and annihilation operators. A laser with a 1-eV photon, a single mode flux of 1 mWcm^{-3} and a typical coherence volume of 1 cm^3 has about 10^5 photons in the field,

$$N = \frac{\text{flux}}{\hbar\omega}\frac{V}{c} \approx \frac{10^{-3}\text{Wcm}^{-3}}{1\text{eV}}\frac{1\text{cm}^3}{3\times 10^{10}\text{cms}^{-1}} \approx 2\times 10^5.$$

This very high quantum number makes it reasonably accurate to describe the laser light as a classical electromagnetic field. This reduces the problem to a semiclassical one. Therefore, we use the interaction representation where the time evolution due to the field energy is absorbed into the wave function,

$$\Psi = \exp(-i\frac{H_{rad}t}{\hbar})\Psi_1.$$

Substituting this definition into Eq. 2.5 we get,

$$(i\hbar\frac{\partial}{\partial t} - \hat{H}_1(t))\Psi_1 = 0,$$

where

$$\hat{H}_1(t) = \frac{\sum_{j=1}^{jmax}[\hat{p}_j - \frac{e_j}{c}A(R_j)]^2}{2m_j} + \sum_{j=1}^{jmax} V(R_1,...,R_{jmax}). \tag{2.6}$$

The particle coordinate in Eq. (2.6) can be transformed into a center-of-mass coordinate, $\mathbf{R}$, and relative coordinate r_i, such that, $\mathbf{R_i} = \mathbf{R} + \mathbf{r_i}$ and the vector potential $A(\mathbf{R_i}, t)$ is then a function of this coordinate through the factor $\exp(\pm i\mathbf{k}.(\mathbf{R}+\mathbf{r_i}))$. The relative coordinate, $\mathbf{r_i}$, is usually limited to the size of the atom in all matrix elements and thus we will replace the exponential factor with unity, since,

$$< \mathbf{k}.\mathbf{r}_i > \simeq k\alpha_0 \simeq \alpha_F \simeq \frac{1}{137}.$$

This is the dipole approximation that is applicable to all of the laser beams. Therefore, the center of mass coordinate couples to the laser through the remaining factor $\exp(\pm i\mathbf{k}.\mathbf{R})$. $\mathbf{R}$ in terms of the nuclear and electron coordinates is given by,

$$\begin{aligned}
\mathbf{R} &= (M_N\mathbf{R}_N + \sum_{i=1}^{Z} m\mathbf{R}_i)/M_a, \\
\mathbf{r_i} &= \mathbf{R_i} - \mathbf{R_N}, \\
M_a &= M_N + Zm,
\end{aligned}$$

where M_N is the nuclear mass and M_a is the atomic mass, m the electron mass, Z is the electron number, $\mathbf{R_N}$ and $\mathbf{R_i}$ are the nuclear and electrons positions respectively. With these variables the Hamiltonian of Eq. (2.6) in the dipole approximation becomes (we have dropped the subscript on $\hat{H}_1$),

$$\hat{H}(t) = \frac{\hat{P}_r}{2M_a} + \frac{1}{2\mu}\sum_{i=1}^{Z}[\hat{p}_i - \frac{e}{c}A(\mathbf{R},t)]^2 + \frac{1}{M_N}\sum_{i>j=1}^{Z}[p_i - \frac{e}{c}A(\mathbf{R},t)].[\hat{p}_j - \frac{e}{c}A(\mathbf{R},t)] + V(\mathbf{r},\mathbf{R}), \tag{2.7}$$

where μ is the reduced mass. The Hamiltonian can be written as,

$$\hat{H}(t) = [\frac{\hat{P}_r}{2M_A} + \frac{Ze^2}{2\mu c^2}A^2(\mathbf{R},t)] + [\frac{1}{2\mu}\sum_{i=1}^{Z}\hat{p}_i^2 + \frac{1}{M_N}\sum_{i>j=1}^{Z}\hat{p}_i\hat{p}_j + V(\mathbf{r},\mathbf{R})] + [\frac{e}{\mu c}A(\mathbf{R},t).\sum_{i=1}^{Z}\hat{p}_i]. \tag{2.8}$$

For a plane wave the vector potential is related to the electric field as,

$$A(\mathbf{R},t) = \frac{cE_0}{\omega}\cos(\omega t - \mathbf{k}.\mathbf{R}), \tag{2.9}$$

where E_0 is the amplitude of the electric field, then

$$A^2(\mathbf{R},t) = \frac{c^2}{2\omega^2}E_0^2(\mathbf{R}) + \frac{c^2}{2\omega^2}E_0^2(\mathbf{R})\cos(2(\omega t - \mathbf{k}.\mathbf{R})), \tag{2.10}$$

since the atomic mass is too large to respond to the rapid change of the second term, its effect on the center of mass motion is negligible. On the other hand, a fast atom moving at 10^7 cm/sec travels 10^{-9} cm in a typical period of internal atomic motion of 10^{-16} sec. Therefore, the external condition, $E_0(\mathbf{R})$ can be treated as constant or adiabatically changing. This reduces the first term in Eq. (2.10) to a constant which represents the energy stored in the electromagnetic field. It can be absorbed in the wave function as a constant phase. In the atom reference frame the Hamiltonian can be rewritten as,

$$\hat{H}(t) = \frac{1}{2\mu}\sum_{i=1}^{Z}[p_i - \frac{e}{c}A(\mathbf{R},t))]^2 + \frac{1}{M_N}\sum_{i>j=1}^{Z}[p_i - \frac{e}{c}A(\mathbf{R},t)].[p_j - \frac{e}{c}A(\mathbf{R},t)] + V(\mathbf{r},\mathbf{R}), \tag{2.11}$$

Now in order to absorb the electromagnetic energy as a phase factor in the wave-function let us use a gauge transformation,

$$\Psi' = e^{i\phi}\Psi$$

such that Ψ' satisfies a new Hamiltonian which does not have the A^2 term. Substituting Ψ' in the Shrödinger equation we get,

$$[i\hbar\frac{\partial}{\partial t} - (e^{-i\phi}He^{i\phi} - \hbar\dot{\phi})]\Psi' = 0, \tag{2.12}$$

Now to remove the A^2 term we define ϕ as [36],

$$\phi = \frac{Ze^2}{2mc^2\hbar}(\frac{M_a}{M_N})\int_{-\infty}^{t} dt' A^2(\mathbf{R}, t'), \tag{2.13}$$

where m is the electron mass. This reduces the Hamiltonian given by Eq. (2.11) into,

$$\hat{H}'(t) = \frac{1}{2\mu}\sum_{i=1}^{Z}\hat{p}_i + \frac{1}{M_N}\sum_{i>j=1}^{Z}\hat{p}_i.p_j + \frac{e}{mc}\frac{M_a}{M_N}A(\mathbf{R}, t).\sum_{i=1}^{Z}\hat{p}_i + V(\mathbf{r}, \mathbf{R}), \tag{2.14}$$

The coupling of the matter field to the electromagnetic field is only in the term $A(t).p$. Hence the Hamiltonian of the system can be written as,

$$\hat{H}' = \hat{H}_0 + \hat{H}_1,$$

where $\hat{H}_0$ is the atomic unperturbed Hamiltonian and $\hat{H}_1 = (e/mc)A(t).\sum_i \hat{p}_i$ is the interaction Hamiltonian. Now that we have derived the interaction Hamiltonian we focus the discussion to the case of a two level atom with a single electron where the interaction Hamiltonian can be further simplified. For such a case the interaction Hamiltonian is given by, $\hat{H}_1 = (e/mc)A(t).\hat{p}$. Since for any $\hat{H}_0 = \hat{P}^2/2m + V(\mathbf{R})$ it is true that,

$$[\hat{\mathbf{R}}, \hat{H}_0] = \frac{i\hbar}{m}\hat{P}, \tag{2.15}$$

then we find that,

$$< e|\hat{P}|g >= im(\omega_e - \omega_g) < e|\hat{\mathbf{R}}|g >, \tag{2.16}$$

where $|e>$ and $|g>$ are the excited and ground state wave-functions of the two level atom with $\hbar\omega_e$ and $\hbar\omega_g$ their energies. Substituting Eq. (2.16) into Eq. (2.15) the elements of the perturbation Hamiltonian are given by,

$$H_{1eg}(t) = -\frac{e}{ic}A(t).(\omega_e - \omega_g) < e|\hat{\mathbf{R}}|g > . \tag{2.17}$$

On the other hand, for the electric field we have (only -ω is used in order to satisfy energy conservation),

$$\begin{aligned} E &= -\frac{1}{c}\frac{\partial A}{\partial t} \\ &= -\frac{1}{c}\frac{\partial}{\partial t}(A_0 e^{-i\omega t}) \\ &= \frac{i\omega}{c}A_0 e^{(-i\omega t)} \\ &= \frac{i\omega}{c}A(t), \end{aligned} \tag{2.18}$$

where ω is the laser frequency. Substituting Eq. (2.19) into the perturbation Hamiltonian we get,

$$H_{1eg} = -\mathbf{E}.\mu(\frac{\omega_e - \omega_g}{\omega}), \tag{2.19}$$

where $\mu = e < e|\hat{\mathbf{R}}|g >$ is the induced dipole moment. Obviously parity conservation is going to set the diagonal elements of the perturbation Hamiltonian to zero. However, Eq. (2.19) can be simplified further if we note that the ratio in this equation is very close to unity in the case of the nearly resonant laser beams in which we are interested. Finally, using all of this information the Hamiltonian can be written as,

$$H = \begin{pmatrix} \hbar\omega_g & -\mu.E(t) \\ -\mu.E^*(t) & \hbar\omega_e \end{pmatrix}. \tag{2.20}$$

The time variation of the elements of the density matrix is given by,

$$\frac{d}{dt}\begin{pmatrix} \rho_{11} & \rho_{12} \\ \rho_{21} & \rho_{22} \end{pmatrix} = -\frac{i}{\hbar}\begin{pmatrix} -\mu.(E(t)\rho_{21} - E^*(t)\rho_{21}^*) & -\hbar\omega_0\rho_{21}^* + \mu.E(t)(\rho_{11} - \rho_{22}) \\ \hbar\omega_0\rho_{21} - \mu.E(t)(\rho_{11} - \rho_{22}) & \mu.(E(t)\rho_{21} - E^*(t)\rho_{21}^*) \end{pmatrix}. \tag{2.21}$$

Where we have used the fact that $\rho_{12} = \rho_{21}^*$ and $\omega_0 = \omega_e - \omega_g$. We can reduce these equations to,

$$\frac{d\rho_{21}}{dt} = -\frac{\rho_{21}}{T_2} - i\omega_0\rho_{21} + i\frac{\mu E^*(t)}{\hbar}(\rho_{11} - \rho_{22}) \tag{2.22}$$

$$\frac{d}{dt}(\rho_{11} - \rho_{22}) = -\frac{(\rho_{11} - \rho_{22}) - (\rho_{11} - \rho_{22})_0}{\tau} + 2i\frac{\mu}{\hbar}\left(E(t)\rho_{21} - E^*(t)\rho_{21}^*\right) \tag{2.23}$$

Where the first parts in the equations are introduced to account for the effect of collisions and spontaneous emission in the evolution of the density matrix with T_2 and τ for their time constants respectively (see Yariv[37] for more details). If we assume that $\rho_{21} = \sigma_{21}(t)\ \exp\ (-i\omega t)$ and $E(t) = E_0(R)\ \cos(\omega t)$ then

$$\begin{aligned} \dot{\sigma}_{21} &= -\frac{\sigma_{21}}{T_2} + i(\omega - \omega_0)\sigma_{21} + i\frac{\mu E_0}{2\hbar}(\rho_{11} - \rho_{22}) \\ &+ i\frac{\mu E_0}{2\hbar}(\rho_{11} - \rho_{22})e^{2i\omega t} \end{aligned} \tag{2.24}$$

$$\begin{aligned} \dot{\rho}_{11} - \dot{\rho}_{22} &= \frac{(\rho_{11} - \rho_{22}) - (\rho_{11} - \rho_{22})_0}{\tau} + \frac{2i\mu E_0}{\hbar}(\sigma_{21} - \sigma_{21}^*) \\ &+ \frac{2i\mu E_0}{\hbar}(\sigma_{21}e^{-2i\omega t} - \sigma_{21}^* e^{2i\omega t}), \end{aligned} \tag{2.25}$$

where the index 0 indicates the initial value of the $\rho_{11} - \rho_{22}$. We ignore the terms with high frequencies in the last result because they average to zero (Rotating Wave Approximation). The steady state solution (time variation of the parameters is zero) for the variables is,

$$2\mathrm{Im}(\sigma_{21}) = \frac{\Omega\ T_2}{1 + \delta^2 T_2^2 + \Omega^2\ T_2\tau} \tag{2.26}$$

$$2\mathrm{Re}(\sigma_{21}) = \frac{\delta\ \Omega\ T_2^2}{1 + \delta^2\ T_2^2\ + \Omega^2\ T_2\ \tau} \tag{2.27}$$

$$\rho_{11} - \rho_{22} = \frac{1 + \delta^2\ T_2^2}{1 + \delta^2\ T_2^2\ + \Omega^2\ T_2\ \tau} \tag{2.28}$$

$$\tag{2.29}$$

Where $\Omega = \frac{\mu E_0}{\hbar}$ is the Rabi frequency, $\delta = (\omega - \omega_0)$ and $(\rho_{11} - \rho_{22})_0 = 1$. Using $\rho_{11} + \rho_{22} = 1$, one can explicitly calculate ρ_{11} and ρ_{22}. Now we are ready to calculate the force operator from Eq. (2.20),

$$\hat{F} = -\frac{\partial \hat{H}}{\partial R} = \begin{pmatrix} 0 & \mu\frac{\partial \hat{E}}{\partial R} \\ \mu(\frac{\partial \hat{E}}{\partial R})^* & 0 \end{pmatrix}, \tag{2.30}$$

Where we have assumed that the electric field's amplitude is constant all over the interaction region. From Eq. (2.2) we have,

$$F = \mathrm{Tr}(\hat{\rho}\hat{F}) = 2\hbar \mathrm{Re}(\rho_{12}(\frac{\partial \hat{E}}{\partial R})^*). \tag{2.31}$$

For a travelling wave the electric field is given by,

$$E = \frac{E_0}{2}(e^{i(kz-\omega t)} + c.c.). \tag{2.32}$$

Substituting this expression for the electric field in Eq. (2.31) we get the force as,

$$F = \hbar \mathrm{Re}(\rho_{12}\frac{ikE_0}{2}(e^{i(kz-\omega t)} - c.c.)). \tag{2.33}$$

Using Eq. (2.27) the force on the atom in a travelling wave is given by,

$$F = \frac{\hbar k}{2}\frac{\Omega^2\ T_2}{1+\delta^2 T_2^2 + \Omega^2\ T_2\tau}. \tag{2.34}$$

In calculating the last result the rotating wave approximation causes the positive frequency component of E(z) to drop. For atoms moving with a velocity $\mathbf{v}$, there is a Doppler shift in the frequency in the atom's moving reference frame and hence the detuning will be ,

$$\delta + \mathbf{k}.\mathbf{v}. \tag{2.35}$$

By placing this general detuning into Eq. (2.34) we get the following expression for the force on a moving atom,

$$F = \frac{\hbar k}{2}\frac{\Omega^2\ T_2}{1+(\delta+\mathbf{k}.\mathbf{v})^2\ T_2^2 + \Omega^2\ T_2\tau}. \tag{2.36}$$

Now let us consider two counter propagating beams in the z direction, from Eq. (2.36) we have,

$$F = \frac{\hbar k}{2}\frac{\Omega^2\ T_2}{1+(\delta+kv_z)^2\ T_2^2 + \Omega^2\ T_2\tau} - \frac{\hbar k}{2}\frac{\Omega^2\ T_2}{1+(\delta-kv_z)^2\ T_2^2 + \Omega^2\ T_2\tau}, \tag{2.37}$$

where v_z is the velocity component in the z direction and k is the wavevector. Therefore, the velocity dependent force is given by $F = -\beta v_z$ where the damping coefficient is,

$$\beta = \hbar k^2 \frac{2\Omega^2 T_2^3 \delta}{(1+(\delta+kv_z)^2\ T_2^2 + \Omega^2\ T_2\tau)(1+(\delta-kv_z)^2\ T_2^2 + \Omega^2\ T_2\tau)}. \tag{2.38}$$

This equation can be interpreted in the low light intensity limit as follows[38]. With light detuned below resonance, atoms travelling towards one laser beam see it Doppler shifted upward, closer to resonance. Since such atoms are travelling away from the other laser beam they see its frequency Doppler shifted further downward, hence further out of resonance. Atoms therefore scatter more light from the beam counter propagating to their velocity and thus their velocity is lowered. This is the damping mechanism called optical molasses. Note that this force is velocity dependent and therefore non-conservative. This force is an important tool in laser cooling. By using pairs of beams in three orthogonal directions the atoms will feel a damping force where the beams intersect that will slow them in three dimensions.

One may think that such a pure damping force would reduce the atomic velocities without limit and hence the temperature would go to absolute zero. Since this violates thermodynamic's third law, something has been left out of our description. In fact we have ignored the quantum momentum exchanged at each scattering between the atom and photon. Because of the recoil effect during the absorption and emission of photons, each atom has a statistical movement comparable to the Brownian motion. If the laser frequency ω was tuned to the resonance frequency ω_0 of the atomic transition, the net damping force would be zero (see Eq. (2.38)). Although the time average of the atomic velocity $\langle v \rangle$ would not change, the mean value of $\langle v^2 \rangle$ would increase due to diffusion and the atoms would be heated. The optical cooling for $\omega - \omega_0 < 0$ must compensate for this statistical heating caused by the photon scattering. If the velocity of the atoms has decreased to $v < \gamma/k$ the detuning $\omega - \omega_0$ of the laser frequency must be smaller than the homogeneous line width of the atomic transition γ, in order to stay in resonance. This puts a lower limit of

$$\hbar\gamma < k_B T_{min}$$

or

$$T_D = \frac{\hbar\gamma}{2k_B} \tag{2.39}$$

on the temperature (Doppler limit) if the recoil energy $E_r = \hbar\omega^2/(2M_a c^2)$ is smaller than the uncertainty $\hbar\gamma$ of the homogeneous linewidth. The Doppler limit is typically several hundred μK. However, lower temperatures than T_D have been observed [39]. These sub-Doppler temperatures have been attributed to the multiplicity of sublevels that make up an atomic state [40,41]. In fact there is another limiting temperature usually refer to as the recoil limit. The recoil limit corresponds to the energy that a single photon transfer to an atom after scattering. That is,

$$T_r = \frac{\hbar^2 k^2}{M_a k_B}, \tag{2.40}$$

where k is the laser wave vector and M_a is the atomic mass. This temperature is typically a few μK. Therefore, temperatures in the range of a few tens of μK are achievable with optical molasses techniques.

Now let us expand our imagination and assume that we can come up with an arrangement such that ω_0 is also a linear function of the z displacement. The detuning becomes $\delta \pm k\mathrm{v}_z \pm \alpha\mathrm{z}$ and the net force can be written as,

$$F = -\beta v_z - \frac{\alpha\beta}{k} z. \tag{2.41}$$

This equation shows that this assumption leads to a spatially dependent force where an appropriate choice of α can lead to a trapping force. Therefore, by proper manipulation of the atom-radiation field interaction one can cool as well as trap the atoms.

2.2 Magneto Optical Trap (MOT)

In the previous section we saw that the radiative interaction can provide cooling. In the following we will show that an appropriate inhomogeneous magnetic field leads to the trapping force discussed in the previous section. This mechanism is the working principle of a Magneto Optical Trap (MOT) which is the most popular approach for setting up an apparatus for trapping neutral atoms.

To understand the operation of the MOT consider a simple system of atomic transitions with the scheme of $J_g = 0$ to $J_e = 1$. To further simplify the model let us assume that the atomic motion is only in the z-direction and it is exposed to a linearly inhomogeneous magnetic field $B = B(z) = B_0 z$. This magnetic field splits the excited state into its three Zeeman components. Adding two counter-propagating laser beams of opposite circular polarization, each detuned below the zero field atomic resonance completes the requirements for making the MOT. This situation is shown pictorially in Fig. 2.1. Because of the Zeeman shift, the excited state $M_e = +1$ is shifted up for $B > 0$, where as the state with $M_e = -1$ is shifted down. At z', in Fig. 2.1 the magnetic field tunes the $\Delta M = -1$ transition closer to resonance and the $\Delta M = +1$ transition further out of resonance. Since the polarization of the laser beam incident from the right is chosen to be σ^- and correspondingly for the other beam σ^+, more light is scattered from the σ^- beam than from the σ^+ beam. Thus the atoms are driven towards the center of the trap where the magnetic field is zero. On the other side of the center of the trap, the roles of the $M_e = +1$ and $M_e = -1$ states are reversed and now more light is scattered from the σ^+ beam, again driving the atoms towards the center. This design of the magnetic field and the polarization of light provides both cooling and trapping forces. A 3D extension of this process leads to trapping the atoms at the zero magnetic field region. MOT was first demonstrated in 1987 [7].

2.3 Evaporative Cooling

In Chapter 1 it was mentioned that to observe the condensation transition, phase space densities of the order of 1 are required. Such a transition can not be observed for dense systems where the strong atom-atom interactions makes the condensate extremely unstable. This restriction has directed the research efforts towards dilute systems where the atom-atom interactions are considerably weakened. This naturally requires a reduction in the temperature to increase the phase space density.

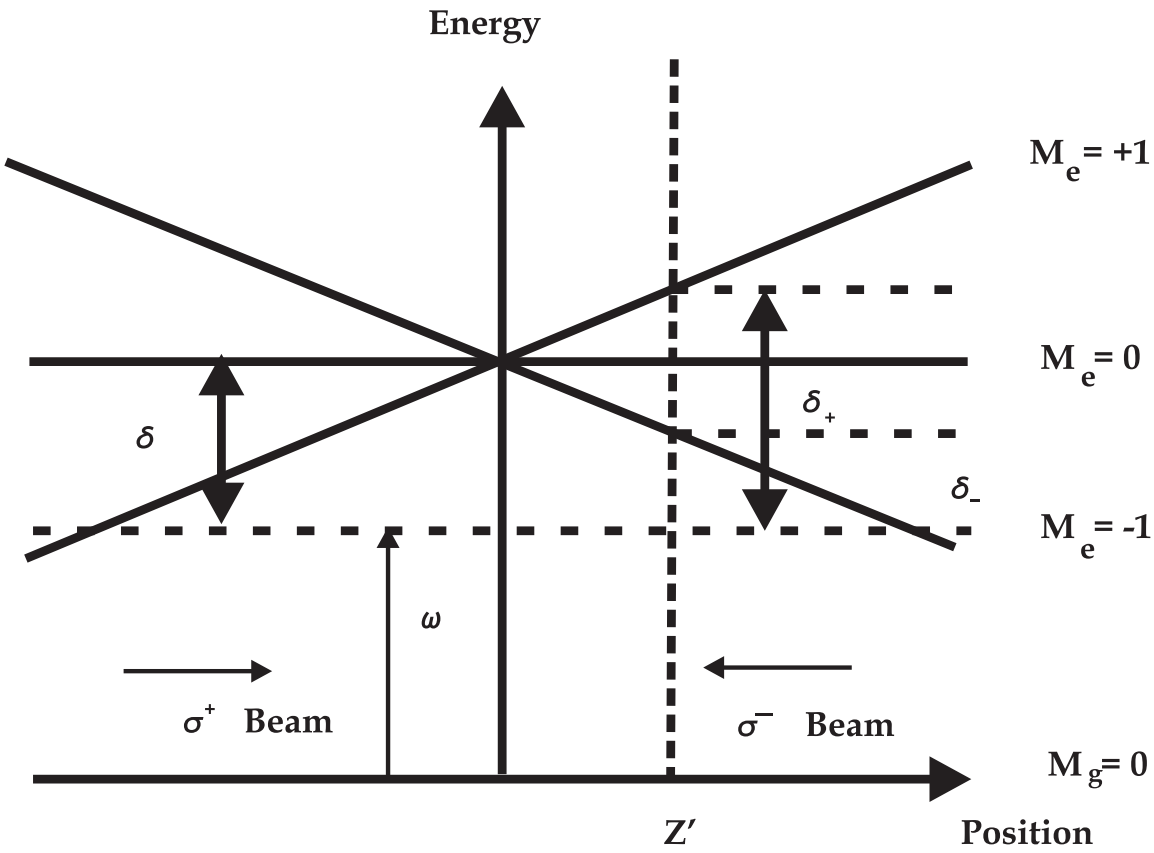

Figure 2.1. The Zeeman splitting for atoms in the $J_g = 0$ to $J_e = 1$ scheme as a function of z-displacement in the presence of an inhomogeneous magnetic field.

In the early days of laser cooling there was a great hope that this would be one of the possible routes to reach the desired conditions for a BEC transition. However, conventional laser cooling methods typically result in trapped atomic clouds with densities of 10^{10}cm^{-3} to 10^{11}cm^{-3}. As we saw in the previous section, in these traps the temperature is limited by the recoil limit of polarization-gradient cooling. Furthermore, the density is limited by absorption and radiation trapping of the cooling light [42], by excited state collisions [43], and eventually by level shifts due to the resonant dipole interactions [44]. All of the above mentioned phenomena limit the maximum achievable phase space density to $10^{-5} - 10^{-4}$. A breakthrough on the problem occurred in 1985, when Harald Hess [45] suggested evaporative cooling as an efficient way to cool trapped atoms [46,47]. His idea was based on the preferential removal of those atoms from a confined sample with energy higher than the average, followed by re-thermalization of the remaining atoms by elastic collisions. His original suggestion focused on trapped atomic hydrogen, but in 1994 the technique was extended to alkali atoms by combining evaporative cooling with laser cooling [48]. Very soon, evaporative cooling showed its dramatic potential by becoming the key technique to achieve BEC [12,49,50]. Obviously, evaporative cooling of atomic gases requires an environment for the atoms which insulate them from the "hot world". Therefore, a wall-free confinement of the atomic cloud would be ideal. However, since the evaporative cooling must cool the atoms below the recoil limit, none of the elements of the MOT can be used. Mainly two methods are used to provide such conditions for the atomic cloud, magnetic fields or far-off-resonant optical fields.

Far off-resonant optical dipole traps (FORTs) [51] rely on the principle that an off-resonant laser beam attracts or repels atoms depending on whether it is red or blue detuned. The trap depth depends on the laser intensity divided by the detuning, where as the spontaneous rate of light scattering scales as the intensity divided by the square of the detuning. Therefore, heating due to the spontaneous scattering is considerably suppressed as the detuning is increased [52]. For the purpose of this

chapter we ignore the FORT loading and study only the physics of evaporative cooling. In the later chapters we will give a more complete treatment of the properties of optical traps and their loading characteristics.

The process of evaporative cooling has been the subject of several theoretical studies. Since evaporative cooling is a relatively simple classical process its theoretical foundation is well established. The first comprehensive model of evaporative cooling was presented by Doyle and coworkers [53,54]. They derived a set of coupled differential equations which described various cooling, heating and loss processes. They also included adiabatic change of the potential during the cooling process. Luiten *et al.* [55] modelled evaporative cooling with a kinetic theory and a numerical solution of the Boltzman equation. Davis *et al.* [56] approximated the evaporative cooling as a discrete series of truncation and rethermalization processes and arrived at simple analytical results. Monte Carlo trajectory techniques were developed by Holland *et al.* [57], and Wu and Foot [58], to directly simulate the evaporation process. However, most of the dynamics of evaporative cooling is model independent and follows from simple considerations. In the following we use a scaling law approach motivated by the work of O'Hara *et al.* [59] to see the effect of the evaporation and lowering the potential on increasing the phase space density.

Let us take the zero of energy to be at the bottom of the trap. The evaporating atoms will have an average energy of $U + \alpha K_B T$, where $\alpha = (\eta - 5)/(\eta - 4)$ [59] and η is the ratio of trap depth to thermal energy. The energy loss rate is then

$$\dot{E} = \dot{N}(U + \alpha K_B T) \tag{2.42}$$

where $\dot{N}$ is the rate at which atoms evaporate from the trap. As the trap depth is adiabatically lowered at a rate $\dot{U}$, it changes the total energy of the trap. The atoms vibrate in a harmonic potential, and therefore $E/2$ is the average potential energy. The potential energy then changes at a rate $\frac{\dot{U}}{U}\frac{E}{2}$ and the total energy obeys the evolution equation

$$\dot{E} = \dot{N}(U + \alpha K_B T) + \frac{\dot{U}}{U}\frac{E}{2}. \tag{2.43}$$

In the classical limit, $E = 3NK_BT$ is the total energy of the trapped gas. Therefore Eq. (2.43) can be rewritten as

$$3NK_B\dot{T} = \dot{N}(U + \alpha K_BT - 3K_BT) + \frac{1}{2}\frac{\dot{U}}{U}3NK_BT \tag{2.44}$$

Solving this equation with a fixed value for η i.e $\dot{U} = \eta K_B\dot{T}$, the number of trapped atoms as a function of trap depth is given by,

$$\frac{N}{N_i} = (\frac{U}{U_i})^{\frac{3}{2(\eta'-3)}}, \tag{2.45}$$

where i refers to the initial condition at $t = 0$ and $\eta' = \eta+\alpha$. The phase space density in the classical regime is

$$\rho = \frac{N(h\nu)^3}{(K_BT)^3} \tag{2.46}$$

where $\nu(t) \propto \sqrt{U}$ is the geometric mean of the trap oscillation frequencies. Using Eq.(2.45) we get

$$\frac{\rho}{\rho_i} = (\frac{U_i}{U})^{\frac{3(\eta'-4)}{2(\eta'-3)}} = (\frac{N_i}{N})^{\eta'-4}. \tag{2.47}$$

The important feature of Eq. (2.47) is the increase in the phase space density even though particles leave the trap. This is the key point to understanding why evaporative cooling followed by a lowering of the potential depth helps to increase the phase space density. Figure 2.2 is a plot of Eq. (2.47) for $\rho_i = 3 \times 10^{-3}$ and shows that lowering the well depth by a factor of 85, a reasonable factor for optical traps, yields a phase space density of unity. The initial phase space density that we have used in plotting Fig. 2.2 is approximately the same as the phase space density in an optical trap immediately after loading from a MOT. The phase space density versus number of atoms given by Eq. (2.47) is shown in Fig. 2.3. Therefore, as far as an experimentalist is concerned, the scaling laws show that one can start from the initial values present in an optical trap and use evaporative cooling to increase the phase space density and still have enough atoms to observe the BEC transition. All of these discussions are valid under the condition that the re-thermalization, determined by the elastic collision rate, is faster than the time scale over which the potential changes.

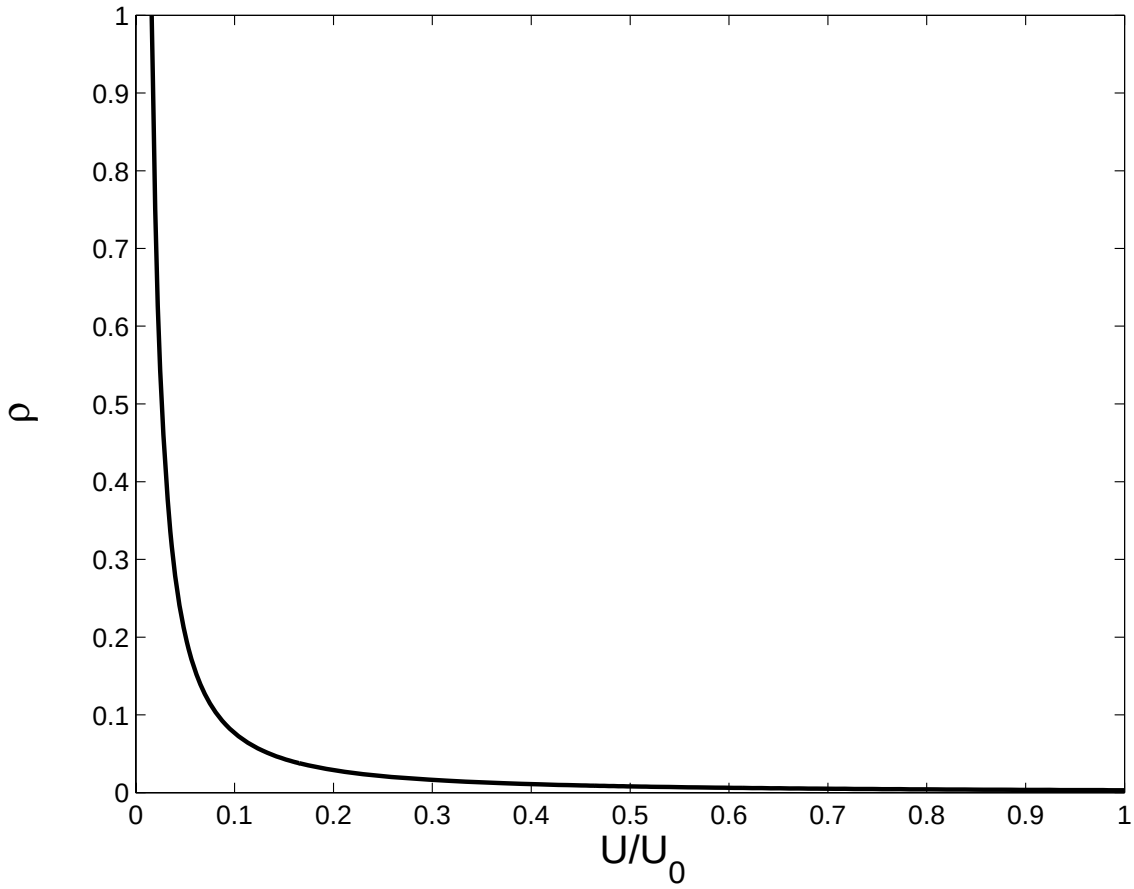

Figure 2.2. Phase space density versus potential depth with $\eta = 10$.

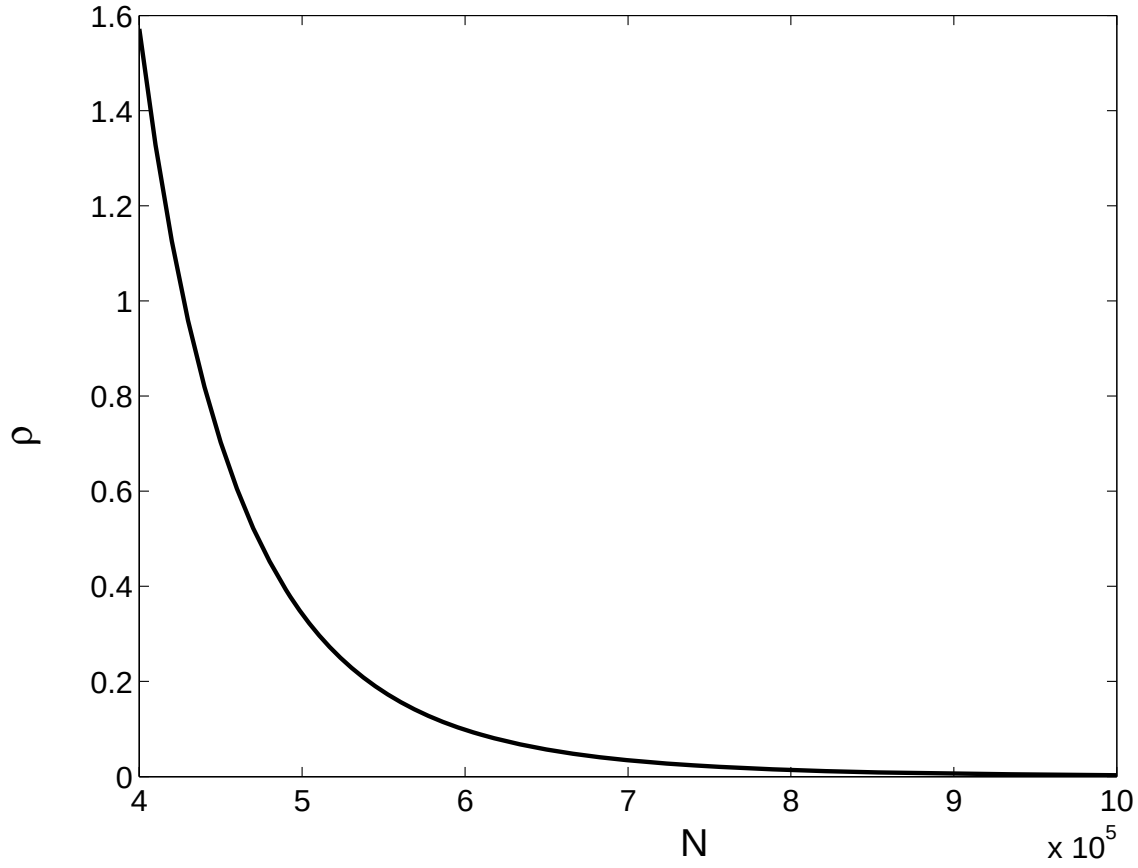

Figure 2.3. Phase space density versus number of atoms in the trap with $\eta = 10$.

The collision rate is given by $\gamma = n_0 \bar{v} \sigma$, where $\bar{v} = \sqrt{3K_B T/M}$, n_0 is the peak density, and σ is the scattering cross section. Since $n_0 = \rho/\lambda_{dB}^3$ and $\lambda_{dB} \propto T^{-1/2}$ then $\gamma \propto \rho T^2$. Therefore,

$$\frac{\gamma_f}{\gamma_i} = (\frac{U_f}{U_i})^{\eta'/2(\eta'-3)} \tag{2.48}$$

Figure 2.4 shows the evolution of the scattering rate versus trap depth for $\eta = 10$. For the numbers used in this section, this figure shows that the elastic scattering rate reduces by a factor of over 20 at the end of the process. Ultimately this determines the speed of the evaporative cooling. Now that we are convinced that evaporative cooling is capable of increasing the phase space density despite the loss of some atoms, we explain our set up for realizing all-optical BEC.

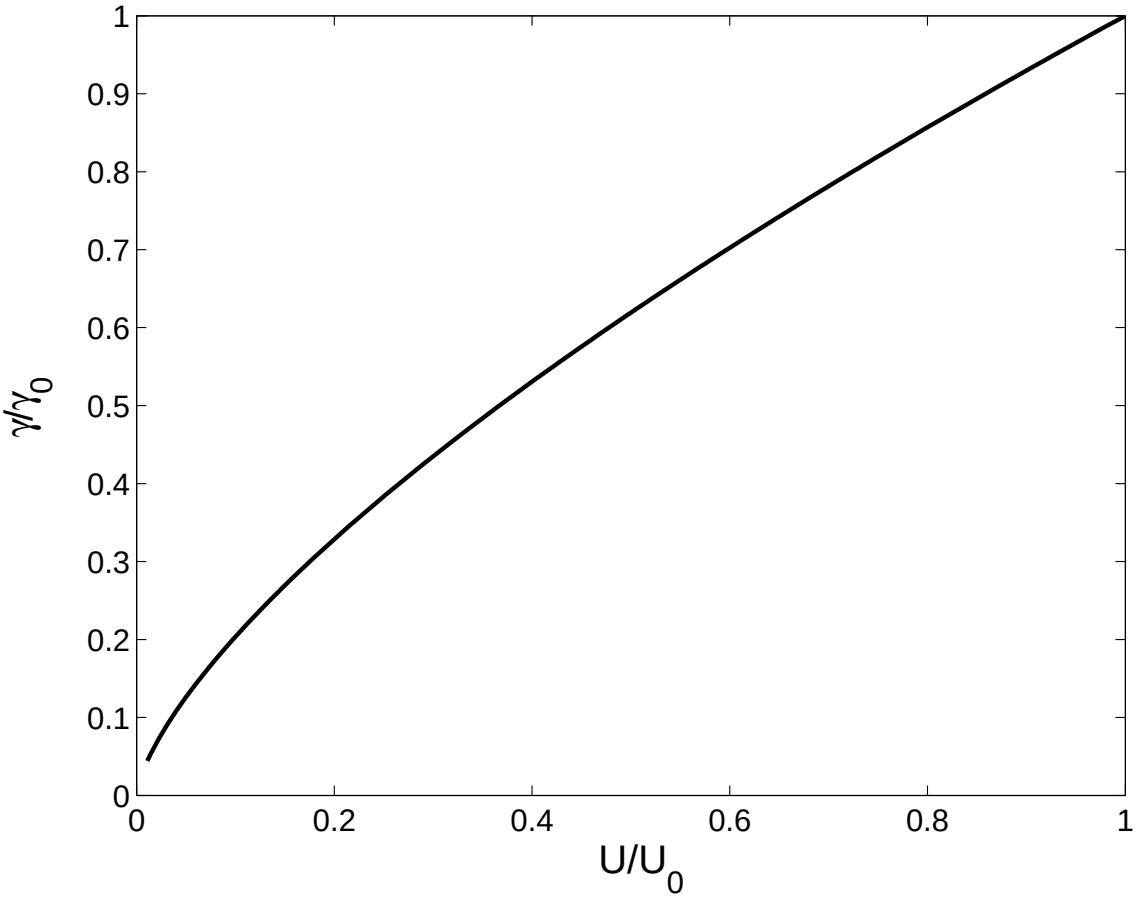

Figure 2.4. Scattering rate versus trap depth with $\eta = 10$.

CHAPTER 3

THE IDEAL BOSE GAS IN A HARMONIC TRAP

As mentioned earlier, Einstein used noninteracting bosons in a box as the basis for his prediction of BEC. The first step in reproducing his theory for particles of mass m is approximating the confining potential with a quadratic form (this formula will be justified later),

$$V_{ext}(r) = \frac{m}{2}(\omega_x^2 x^2 + \omega_y^2 y^2 + \omega_z^2 z^2). \tag{3.1}$$

Where ω_x, ω_y and ω_z are the trap frequencies in x, y and z directions. It is straightforward to study a system of noninteracting particles confined in this way. The many-body Hamiltonian is the sum of single particle Hamiltonians whose eigenvalues have the form,

$$\epsilon_{n_x n_y n_z} = (n_x + \frac{1}{2})\hbar\omega_x + (n_y + \frac{1}{2})\hbar\omega_y + (n_z + \frac{1}{2})\hbar\omega_z. \tag{3.2}$$

The ground state of N noninteracting bosons confined by the harmonic potential is obtained by putting all the particles in the lowest single-particle state $n_x = n_y = n_z = 0$,

$$\phi(r_1, ..., r_N) = \Pi\phi_0(r_i) \tag{3.3}$$

where

$$\phi_0(r_i) = (\frac{m\omega_{ho}}{\pi\hbar})^{3/4} \exp(-\frac{m}{2\hbar}(\omega_x x_i^2 + \omega_y y_i^2 + \omega_z z_i^2)) \tag{3.4}$$

and we define

$$\omega_{ho} = (\omega_x\omega_y\omega_z)^{1/3}. \tag{3.5}$$

The density distribution then becomes $n(r) = N|\phi_0(r)|^2$. The size of the BEC is characterized by the harmonic oscillator length

$$a_{ho} = (\frac{\hbar}{m\omega_{ho}})^{1/2}. \tag{3.6}$$

In the current experiments, a_{ho} has a typical value of the order of 1 μm. At finite temperatures, only a fraction of the atoms occupy the ground state and the rest are distributed in the excited states. A rough estimate for the atomic cloud's size can be obtained by assuming $\mathrm{k_B}T >> \hbar\omega_{ho}$. Where T is the cloud's thermal temperature, and taking the density of the thermal cloud of atoms to be given by a classical Boltzmann distribution

$$n_{cl} \propto \exp(-\frac{V_{ext}}{k_B T}). \tag{3.7}$$

Then if $V_{ext} = \frac{1}{2}m\omega_{ho}^2 r^2$, the width of the gaussian is

$$R_T = a_{ho}(\frac{2k_B T}{\hbar\omega_{ho}})^{1/2} \tag{3.8}$$

which is greater than a_{ho}. Therefore we expect BEC to show up with the appearance of a sharp peak in the central region of the density distribution. The Fourier transform of the wave function specifies that the momentum distribution of the atoms in the condensate will have a width proportional to a_{ho}^{-1}. Therefore, BEC appears as a peak in both coordinate and momentum spaces. Using these properties Anderson *et al.* [12] have developed a method to observe the condensate. We will discuss the methods to detect BEC in the coordinate space in a separate section. In the case of the momentum distribution one lets the condensate expand freely, by switching off the trap, and measures the density of the expanded cloud with light absorption. For non-interacting particles the expansion is ballistic and the imaged spatial distribution of the expanding cloud can be directly related to the initial momentum distribution.

The interaction between the atoms can significantly modify the shape of the observed momentum distribution. It is very important to study this effect in detail as it is the situation encountered in the experiment. We will return to this point after reviewing the thermodynamics of the trapped bosons at finite temperatures.

3.1 Thermodynamics of BEC in an external potential

In the grand canonical ensemble the total number of particles is given by,

$$N = \sum_{n_x n_y n_z} (\exp([\beta(\epsilon_{n_x n_y n_z} - \mu)] - 1))^{-1} \tag{3.9}$$

and the total energy is given by

$$E = \sum_{n_x n_y n_z} \epsilon_{n_x n_y n_z} (\exp([\beta(\epsilon_{n_x n_y n_z} - \mu) - 1]))^{-1} \tag{3.10}$$

where μ is the chemical potential and $\beta = (k_B T)^{-1}$. Below a given critical temperature, T_c, the population of the lowest state becomes macroscopically occupied. This is the definition of BEC. The calculation of the critical temperature, the fraction of particles in the lowest state (condensate fraction), and the other thermodynamic quantities, start from Eqs. (3.9) and (3.10) with the appropriate spectrum of eigen energies. Since the system is inhomogeneous the statistics of the trapped particles is not trivial. As a first step let us find the density of states Ω. The number of states in volume d^3r with the magnitude of momentum between p and $p + dp$ is,

$$\Omega(p) d^3r dp = \frac{d^3r d^3p}{h^3} = \frac{d^3r 4\pi p^2 dp}{h^3}. \tag{3.11}$$

If we ignore the particle-particle interaction, the energy of a particle is given by,

$$\epsilon = \frac{p^2}{2m} + U(r). \tag{3.12}$$

By this definition we can rewrite Eq. (3.11) as,

$$\Omega(\epsilon) d\epsilon = \frac{d^3r}{4\pi^2\hbar^3} (2m)^{3/2} \sqrt{\epsilon - U}. \tag{3.13}$$

Integrating this equation over the available volume for the particle gives the expression for the density of states

$$\rho(\epsilon) = \frac{(2m)^{3/2}}{4\pi^2\hbar^3} \int_{V_\epsilon} \sqrt{\epsilon - U} d^3r. \tag{3.14}$$

For a system of N bosonic particles the occupation number $n(\epsilon)$ of particles in an energy ϵ with degeneracy g_ϵ is given by

$$n(\epsilon) = \frac{g_\epsilon}{exp(\frac{\epsilon-\mu}{k_B T}) - 1}. \tag{3.15}$$

Using Eqs. (3.14) and (3.15) the total number of particles in a bosonic gas is given by

$$N = N_0 + \int_0^\infty n(\epsilon)\rho(\epsilon)d\epsilon. \tag{3.16}$$

Here the number of particles in the ground state N_0 is written separately because according to Eq. (3.14), $\rho(U) = 0$. The total energy of the system is

$$E(T) = \int_0^\infty \epsilon n(\epsilon)\rho(\epsilon)d\epsilon, \tag{3.17}$$

and the heat capacity is

$$C(T) = \frac{\partial E(T)}{\partial T} = \frac{1}{k_B T}\int_0^\infty \frac{\epsilon\rho(\epsilon)}{g_\epsilon}[\mu'(T) + \frac{\epsilon-\mu}{T}]n(\epsilon)^2 \exp[\frac{\epsilon-\mu}{k_B T}]d\epsilon, \tag{3.18}$$

where $\mu'(T) = \frac{\partial \mu}{\partial T}$. This relation indicates that to evaluate $C(T)$ we need $\mu(T)$ which one can relate to N. To go any further we need to have the form of the potential. We will justify later that in our experiments the potential can be approximated with a power law. Therefore we consider the potential to be [60],

$$U(r) = \epsilon_1|\frac{x}{a}|^p + \epsilon_2|\frac{y}{b}|^l + \epsilon_3|\frac{z}{c}|^q, \qquad r^2 = x^2 + y^2 + z^2. \tag{3.19}$$

Applying this potential in Eq. (3.14) the density of states is given by

$$\rho(\epsilon) = [\frac{2\pi(2m)^{3/2}}{h^3}]\frac{abc}{\epsilon_1^{1/p}\epsilon_2^{1/l}\epsilon_3^{1/q}}\epsilon^\eta F(p,l,q), \tag{3.20}$$

where $\eta = 1/p + 1/l + 1/q + 1/2$ and $F(p,l,q)$ is defined by,

$$F(p,l,q) = [\int_{-1}^1 (1-X^p)^{1/2+1/q+1/l}dX][\int_{-1}^1 (1-X^l)^{1/2+1/q}dX][\int_{-1}^1 (1-X^q)^{1/2}dX]. \tag{3.21}$$

Therefore,

$$N = N_0 + \int_0^\infty \left(\frac{(2m)^{3/2}}{4\pi^2\hbar^3}\right)\frac{abc}{\epsilon_1^{1/p}\epsilon_2^{1/l}\epsilon_3^{1/q}}\epsilon^\eta F(p,l,q)\frac{1}{\exp(\frac{\epsilon-\mu}{k_B T}) - 1}d\epsilon. \tag{3.22}$$

N_0 is zero and μ goes to zero at T_c, therefore the last equation can be written as,

$$N = \frac{(2m)^{3/2}}{4\pi^2\hbar^3}\frac{abc}{\epsilon_1^{1/p}\epsilon_2^{1/l}\epsilon_3^{1/q}}F(p,l,q)(k_BT_c)^{\eta+1}Q \tag{3.23}$$

where Q is given by

$$Q = \int_0^\infty \frac{x^\eta dx}{e^x - 1} \tag{3.24}$$

and so the critical temperature for a system with N bosons is,

$$k_B\ T_c = [\frac{4\pi^2\hbar^3}{(2m)^{3/2}}\ \ \frac{N}{abc}\ \ \frac{\epsilon_1^{1/p}\epsilon_2^{1/l}\epsilon_3^{1/q}}{F(p,l,q)\ Q(\eta)}]^{\frac{1}{\eta+1}}. \tag{3.25}$$

The ratio of bosons in the ground state to the total number of particles for $T < T_c$ is,

$$\frac{N_0}{N} = 1 - \left(\frac{T}{T_c}\right)^{\eta+1}. \tag{3.26}$$

Eq. (3.25) clearly shows the effect of a change in the geometry of the potential on critical temperature. To make this point clear let us study the effect of a far off resonant field (like a CO_2 laser beam in the case of Rb87) on a atom. If the atom has the polarizability α_g then the atom-field interaction energy is,

$$U = -\frac{1}{2}\alpha_g|E|^2 \tag{3.27}$$

where E is the electric field of a gaussian beam propagating in the z direction and is given by,

$$E(x,y,z) = E_0\frac{w_0}{w(z)}e^{\frac{-(x^2+y^2)}{w(z)}}e^{ik\frac{x^2+y^2}{2R(z)}}e^{i(kz-\omega t-\phi(z))} \tag{3.28}$$

where

$$w(z) = w_0\left(1 + (\frac{z}{z_R})^2\right)^{1/2} \qquad\qquad and\ \ z_R = \frac{\pi w_0^2}{\lambda}.$$

Here w_0 is the beam waist, $R(z)$ the radius of curvature of the beam and z_R is the Rayleigh length. Then

$$|E|^2 = \frac{E_0^2\exp\left(\frac{-2(x^2+y^2)}{w_0^2(1+(\frac{z}{z_R})^2)}\right)}{1+(\frac{z}{z_R})^2}. \tag{3.29}$$

Experimentally we can focus a CO_2 laser beam down to about 50 μm so that the BEC will have a dimension around a few microns. Therefore the Rayleigh length is large compared to the BEC dimensions and we can approximate the potential as,

$$U = -\frac{1}{2}\alpha_g E_0^2(1 - \frac{2x^2}{w_0^2} - \frac{2y^2}{w_0^2} - \frac{z^2}{z_R^2}). \tag{3.30}$$

Redefining the potential as $U = U_1 - U_{01}$ with $U_{01} = \frac{1}{2}\alpha_g E_0^2$ we get

$$U_1 = U_{01}(\frac{2x^2}{w_0^2} + \frac{2y^2}{w_0^2} + \frac{z^2}{z_R^2}). \tag{3.31}$$

Comparing this form of the potential with the general form given by Eq. (3.19) one reads

$$\epsilon_1 = \epsilon_2 = \epsilon_3 = U_0, \qquad p = l = q = 2, \qquad a = b = \frac{w_0}{\sqrt{2}}, c = z_R$$

Therefore T_c for this potential can be found from

$$k_B T_c = [\frac{h^3}{2\pi(2m)^{3/2}} \frac{2N}{w_0^2 z_R} \frac{U_0^{3/2}}{F(2,2,2)Q(2)}]^{1/3}. \tag{3.32}$$

Now let us consider a second laser beam propagating in the y direction. The amplitude of this beam is given by,

$$|E|^2 = \frac{E_{02}^2 \exp \frac{-2(x^2+z^2)}{w_0^2(1+(\frac{y}{z_R})^2)}}{1 + (\frac{y}{z_R})^2} \tag{3.33}$$

where E_{02} is the amplitude of the second beam's electric field. Using the same approximation to expand this field one can write the total potential in the region where the two beams overlap as,

$$U = U_1 + U_2 = (U_{01} + U_{02})\frac{2x^2}{w_0^2} + (\frac{U_{02}}{z_R^2} + \frac{2U_{01}}{w_0^2})y^2 + (\frac{2U_{02}}{w_0^2} + \frac{U_{01}}{z_R^2})z^2. \tag{3.34}$$

Again the comparison of this result with Eq. (3.19) specifies the potential characteristics as,

$$\epsilon_1 = \epsilon_2 = \epsilon_3 = U_{01}, \qquad p = l = q = 2. \tag{3.35}$$

$$a = \frac{w_0}{\sqrt{2(1+D)}} \tag{3.36}$$

$$b = \frac{w_0 z_R}{\sqrt{2z_R^2 + Dw_0^2}} \tag{3.37}$$

$$c = \frac{w_0 z_R}{\sqrt{w_0^2 + 2Dz_R^2}} \tag{3.38}$$

where D is the ratio of U_{02} over U_{01}. These parameters are clearly different from the one beam configuration but of the same order. Therefore it is possible to realize a BEC using only one beam with a different critical temperature[61].

3.2 Many particle interacting Bosonic system

So far we have seen the effect of statistics on the low temperature properties of an ideal bosonic gas. The main result is that the ground state contains all the particles at $T = 0$. This requires reformulation of the perturbation theory for such systems. In the following we shall briefly discuss the theory [62]. For this situation let us assume that the ground state of N bosons is given by

$$|\Phi_0(N)>=|N,000> \tag{3.39}$$

where zeros are the occupation number of the excited states and the particles are in a box with volume V with periodic boundary conditions. Having many particles in the ground state averages the momentum of the system to zero. If the creation and destruction operators $\hat{a}_0^\dagger$ and $\hat{a}_0$ for the zero momentum mode are applied to the ground state we get,

$$\hat{a}_0|\Phi_0(N)>=N^{1/2}|\Phi_0(N-1)>, \qquad \hat{a}_0^\dagger|\Phi_0(N)>=(N+1)^{1/2}|\Phi_0(N+1)> \tag{3.40}$$

Since it is generally preferable to deal with intensive variables we shall introduce the operators,

$$\hat{\xi_0} \equiv V^{-1/2}\hat{a}_0, \qquad \hat{\xi_0^\dagger} \equiv V^{-1/2}\hat{a}_0^\dagger \tag{3.41}$$

which have the following properties

$$[\hat{\xi_0}, \hat{\xi_0^\dagger}] = V^{-1}$$

$$\hat{\xi_0}|\Phi_0(N)>=(\frac{N}{V})^{1/2}|\Phi_0(N-1)>$$

$$\hat{\xi_0^\dagger}|\Phi_0(N)>=(\frac{N+1}{V})^{1/2}|\Phi_0(N+1)>.$$

In the thermodynamic limit $N \longrightarrow \infty, V \longrightarrow \infty$ then $[\hat{\xi_0}, \hat{\xi_0^\dagger}] = 0$ and therefore it is reasonable to treat the raising and lowering operators as c numbers. This idea was first introduced by Bogoliubov [63]. In an interacting system the inter-particle potential energy reduces the occupation of the ground state. Thus the ground state expectation value of $\hat{N}$ is less than the total particle number. This can be understood as follows, let us write the boson's field operator as

$$\hat{\psi}(x) = \xi_0 + \Sigma_k' V^{-1/2} e^{ik.x} \hat{a}_k = \xi_0 + \hat{\phi}(x) = n_0^{1/2} + \hat{\phi}(x) \tag{3.42}$$

where prime means omit the $k = 0$. Let us study the effect of this representation on the Hamiltonian. The interaction part of $\hat{H}$ is

$$\hat{V} = \frac{1}{2} \int d^3x d^3x' \hat{\psi}^\dagger(x) \hat{\psi}^\dagger(x') V(x - x') \hat{\psi}(x') \hat{\psi}(x). \tag{3.43}$$

Which has the following terms

$$\begin{aligned}
E_0 &= \frac{1}{2} n_0^2 \int d^3x d^3x' V(x - x') \qquad (3.44)\\
\hat{V}_1 &= \frac{1}{2} n_0 \int d^3x d^3x' V(x - x') \hat{\phi}(x') \hat{\phi}(x)\\
\hat{V}_2 &= \frac{1}{2} n_0 \int d^3x d^3x' \hat{\phi}^\dagger(x') \hat{\phi}^\dagger(x) V(x - x')\\
\hat{V}_3 &= 2\frac{1}{2} n_0 \int d^3x d^3x' \hat{\phi}^\dagger(x') V(x - x') \hat{\phi}(x)\\
\hat{V}_4 &= 2\frac{1}{2} n_0 \int d^3x d^3x' \hat{\phi}^\dagger(x) V(x - x') \hat{\phi}(x)\\
\hat{V}_5 &= 2\frac{1}{2} n_0^{1/2} \int d^3x d^3x' \hat{\phi}^\dagger(x') \hat{\phi}^\dagger(x) V(x - x') \hat{\phi}(x)\\
\hat{V}_6 &= 2\frac{1}{2} n_0^{1/2} \int d^3x d^3x' \hat{\phi}^\dagger(x') V(x - x') \hat{\phi}(x') \hat{\phi}(x)\\
\hat{V}_7 &= \frac{1}{2} \int d^3x d^3x' \hat{\phi}^\dagger(x') \hat{\phi}^\dagger(x) V(x - x') \hat{\phi}(x') \hat{\phi}(x)
\end{aligned}$$

Since the Bogolibov description dominates the operators $\hat{a}_0$ and $\hat{a}_0^\dagger$ entirely, all remaining destruction operators annihilate the ground state, therefore becoming the

vacuum state. Consequently the number operator is defined by,

$$\hat{N} = N_0 + \int d^3x \hat{\phi}^\dagger(x)\hat{\phi}(x) = N_0 + \Sigma'_k \hat{a}_k^\dagger \hat{a}_k. \tag{3.45}$$

Where N_0 is a c number. $\hat{N}$ no longer commutes with the Hamiltonian since the various interaction terms alter the number of particles in the condensate. As a result the total number of particles is no longer a constant of motion and must instead be determined through the subsidiary condition

$$N = N_0 + \Sigma'_k < \hat{a}_k^\dagger \hat{a}_k >, \tag{3.46}$$

where the brackets denote the ground state expectation value in the interacting system. We therefore return to the original $\hat{H} = \hat{T} + \hat{V}$ where $\hat{a}_0$ and $\hat{a}_0^\dagger$ are still operators. Let us introduce the grand canonical hermitian operator,

$$\hat{K} = \hat{H} - \mu\hat{N} = \int d^3x \hat{\psi}^\dagger(x)[T-\mu]\hat{\psi}(x) + \frac{1}{2}\int d^3x d^3x' \hat{\psi}^\dagger(x)\hat{\psi}^\dagger(x')V(x-x')\hat{\psi}(x')\hat{\psi}(x) \tag{3.47}$$

This operator has a complete set of eigenfunctions $|\psi_j\rangle$ and commutes with $\hat{N}$. It is impossible to find an exact solution for this many particle hamiltonian. Therefore we assume that an assembly of bosons is condensed whenever the ensemble average $\langle\hat{\psi}(x)\rangle$ remains finite in the thermodynamic limit. Now we introduce the notation

$$\Psi(x) = \langle\hat{\psi}(x)\rangle \tag{3.48}$$

and the deviation operator

$$\hat{\phi}(x) = \hat{\psi}(x) - \Psi(x). \tag{3.49}$$

The c number function $\Psi(x)$ is frequently known as the condensate wave function. In the system under consideration the interaction is weak and most of the particles are in the condensate. Therefore the operator $\hat{\phi}(x)$ may be considered a small correction to $\Psi(x)$. If we expand $\hat{K}$ in powers of $\hat{\phi}(x)$ and its complex conjugate operator up to the second order we get

$$\hat{K} = K_0 + \hat{K}_l + \hat{K}'$$

where

$$K_0 = \int d^3x\Psi(x)[T-\mu]\Psi(x) + \frac{1}{2}\int d^3x d^3x' V(x-x')|\Psi(x)|^2|\Psi(x')|^2 \tag{3.50}$$

$$\begin{aligned}
\hat{K}_l &= \int d^3x\hat{\phi}^\dagger(x)[T-\mu+\int d^3x' V(x-x')|\Psi(x')|^2]\hat{\phi}(x) \qquad (3.51)\\
&+ \int d^3x[T-\mu+\int d^3x' V(x-x')|\Psi(x')|^2]\Psi^*(x)\hat{\phi}(x)\\
\hat{K}' &= \int d^3x\hat{\phi}^\dagger(x)[T-\mu]\hat{\phi}(x) + \int d^3x d^3x' V(x-x')[|\Psi(x')|^2\hat{\phi}^\dagger(x) \qquad (3.52)\\
&+ \Psi^*(x)\Psi(x')\hat{\phi}^\dagger(x')\hat{\phi}(x) + \frac{1}{2}|\Psi^*(x)\Psi^*(x')\hat{\phi}(x')\hat{\phi}(x)\\
&+ \frac{1}{2}\hat{\phi}^\dagger(x)\hat{\phi}^\dagger(x')\Phi(x')\Phi(x)]
\end{aligned}$$

This result can be simplified if $\Psi(x)$ satisfies the following equation [64,65]

$$[T(x)-\mu]\Psi(x) + \int d^3x V(x-x')|\Psi(x')|^2\Psi(x) = 0. \tag{3.53}$$

Therefore the effective $\hat{K}_{eff}$ is

$$\hat{K}_{eff} = K_0 + \hat{K}'.$$

Which can be used to construct

$$\hat{\rho}_{eff} = \frac{e^{-\beta\hat{K}_{eff}}}{\mathrm{Tr}(e^{-\beta\hat{K}_{eff}})}, \tag{3.54}$$

where the ensemble average of any operator is

$$\langle\hat{D}\rangle = \mathrm{Tr}(\hat{\rho}_{eff}\hat{\phi}(x)).$$

Let us assume that the inter-particle potential is a delta function. Then Eq. (3.53) reduces to the well known Gross-Pitaevski (GP) equation [66,67],

$$-(\frac{\hbar^2\nabla^2}{2m}+\mu)\Psi(x) + g|\Psi(x)|^2\Psi(x) + V(x)\Psi(x) = 0, \tag{3.55}$$

where the coupling constant g is related to the scattering length a through

$$g = \frac{4\pi\hbar^2 a}{m}. \tag{3.56}$$

Eq. (3.55) specifies the condensate wave function for an interacting system of bosons. The validity of the GP approximation is based on the condition that the s-wave scattering length is much smaller than the average distance between atoms and that the number of atoms in the condensate is larger than 1.

In general to solve the GP equation one should appeal to numerical methods. The numerical solution of the time independent GP equation is easy to obtain [68]. For a time dependent GP equation we have

$$i\hbar\frac{\partial\Psi(x,t)}{\partial t} = -(\frac{\hbar^2\nabla^2}{2m} + \mu)\Psi(x,t) + g|\Psi(x)|^2\Psi(x,t) + V(x)\Psi(x,t). \tag{3.57}$$

Among the different methods for solving the GP equation we will review the Fast Fourier Transform (FFT) technique, also known as the split step method. In this approach, to find a numerical solution for a GP equation H is expressed as the sum of a kinetic part $\hat{T}$ and a potential part $\hat{V}$. Using the propagation operator we have,

$$\Psi_n(x,t+dt) = \exp(-i\frac{\delta t(\hat{T}+\hat{V})}{\hbar})\Psi_n(x,t) \tag{3.58}$$

We know that the potential operator is diagonal in configuration space while the kinetic operator is diagonal in momentum space. It is therefore effective to split the exponential operator into potential and kinetic parts and operate separately in position space and momentum space. It can be shown that [69]

$$\exp(-i\frac{\delta t(\hat{T}+\hat{V})}{\hbar}) = \exp(-i\frac{\delta t\hat{V}}{2\hbar})\exp(-i\frac{\delta t\hat{T}}{\hbar})\exp(-i\frac{\delta t\hat{V}}{2\hbar}) + O(\delta t^3). \tag{3.59}$$

This expansion is refered to as a half-step potential expansion. The potential operator is easy to apply and corresponds to a phase factor of the wave function in position space. The kinetic part is also a phase factor but in momentum space. Therefore we add $\exp(-i\hat{V}\delta t/2\hbar)$ to the wave function at jth spacial point to get

$$f_n^j = \exp(-i\delta t\frac{\hat{V}_{ext}^j + g|\psi_n^j|^2}{2\hbar})\Psi_n^j, \tag{3.60}$$

here we split the potential into the external potential term and the particle-particle interaction potential term. In the next step a FFT of the f_n^j takes it to the momentum

space where the kinetic part in the half step expansion is a phase factor, therefore we have,

$$F_{n+1}^{k} = \exp(i\frac{\pi^2 k^2 \delta t}{2\hbar^2 L^2})FFT(f_n^j), \tag{3.61}$$

where k denotes the momentum step and $2L$ is the size of the spacial grid. The inverse Fourier transform takes F_{n+1}^{k} back to the coordinate space where the first part of the half-potential step is a phase factor and finally we have,

$$\Psi_{n+1}^{j} = \exp(-i\frac{\delta t(V_{ext}^{j}) + g|\Psi_n^j|^2)}{2\hbar})FFT^{-1}(F_{n+1}^{k}). \tag{3.62}$$

This can be continued to complete the solution of a GP equation in one dimension. By using numerical methods one can generalize this technique to solve GP equations in multi-dimensions.

CHAPTER 4

EXPERIMENTAL APPARATUS

This chapter is organized in a manner that gives a step by step tour of the setup developed in our laboratory for atom trapping and laser cooling. This part starts with selecting an appropriate atom source for the experiment followed by an explanation of the vacuum system. Optical setup including the working principles of diode lasers and their associated optics is explained in details at the end.

4.1 Vacuum system

The heart of the BEC experiments is the vacuum chamber where atoms are collected and cooled to the condensation temperature. Accurate planning of the vacuum chamber is needed since an ultra-high vacuum with a large amount of optical access to the chamber is essential for the experiment. Our vacuum chamber consisted of a six-way cross with an octagonal multi-port chamber attached to one of its flanges. All components were stainless steel and are shown in Fig. 4.1. Four 2.5 cm viewports were used for directing the MOT beams into the chamber and four 2.5 cm diameter ZnSe viewports allowed us to transmit the 10.6 μm light from a CO_2 laser into the chamber (see Fig. 4.2 for the light beam geometry through the octagonal multi-port chamber). A 12.5 cm quartz view port was attached to another one of the six-way chamber. The ion pump was attached to the third flange where the fourth flange was attached to a valve which was used to attache the roughing and turbo pumps. A cluster flange with three angled 70 mm conflate flanges was also attached to the six way cross. One of these flanges has an electric feedthrough which is connected to the rubidium dispensers. Another one is used as a port for vacuum gauge.

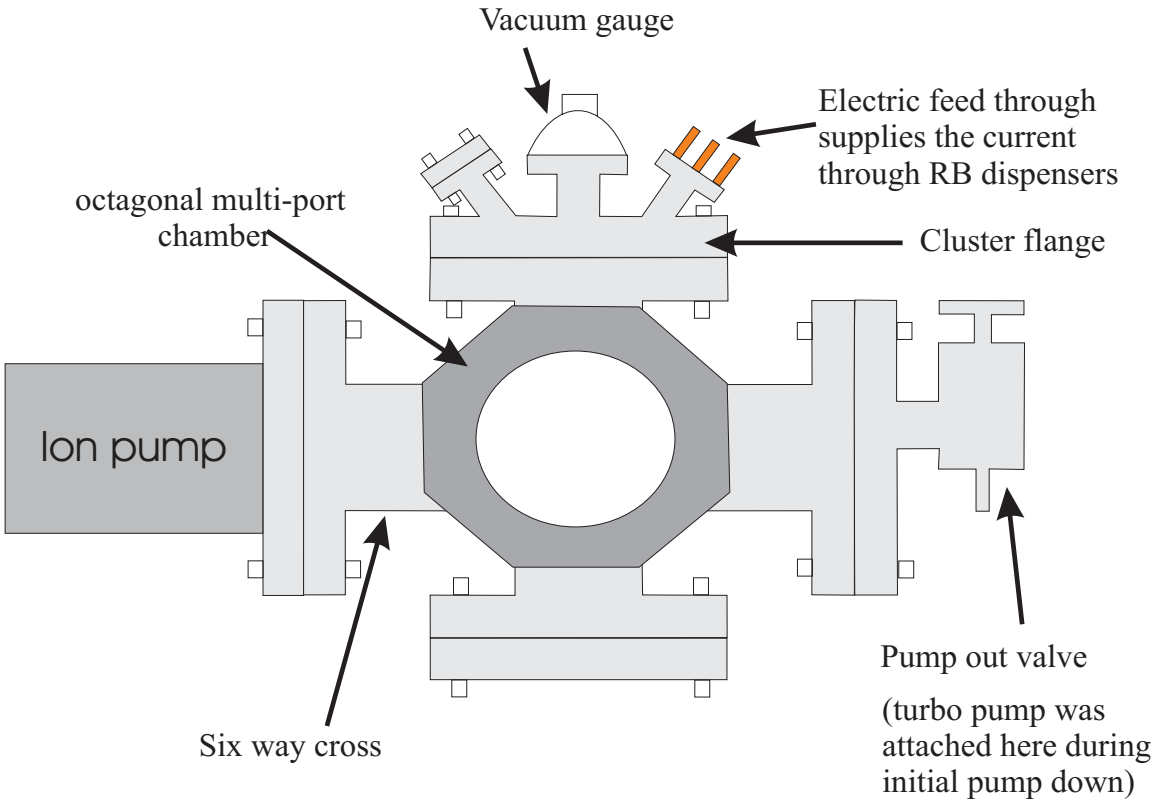

Figure 4.1. Vacuum chamber apparatus. The six-way cross is mounted behind the octagonal multi-port chamber in this schematic.

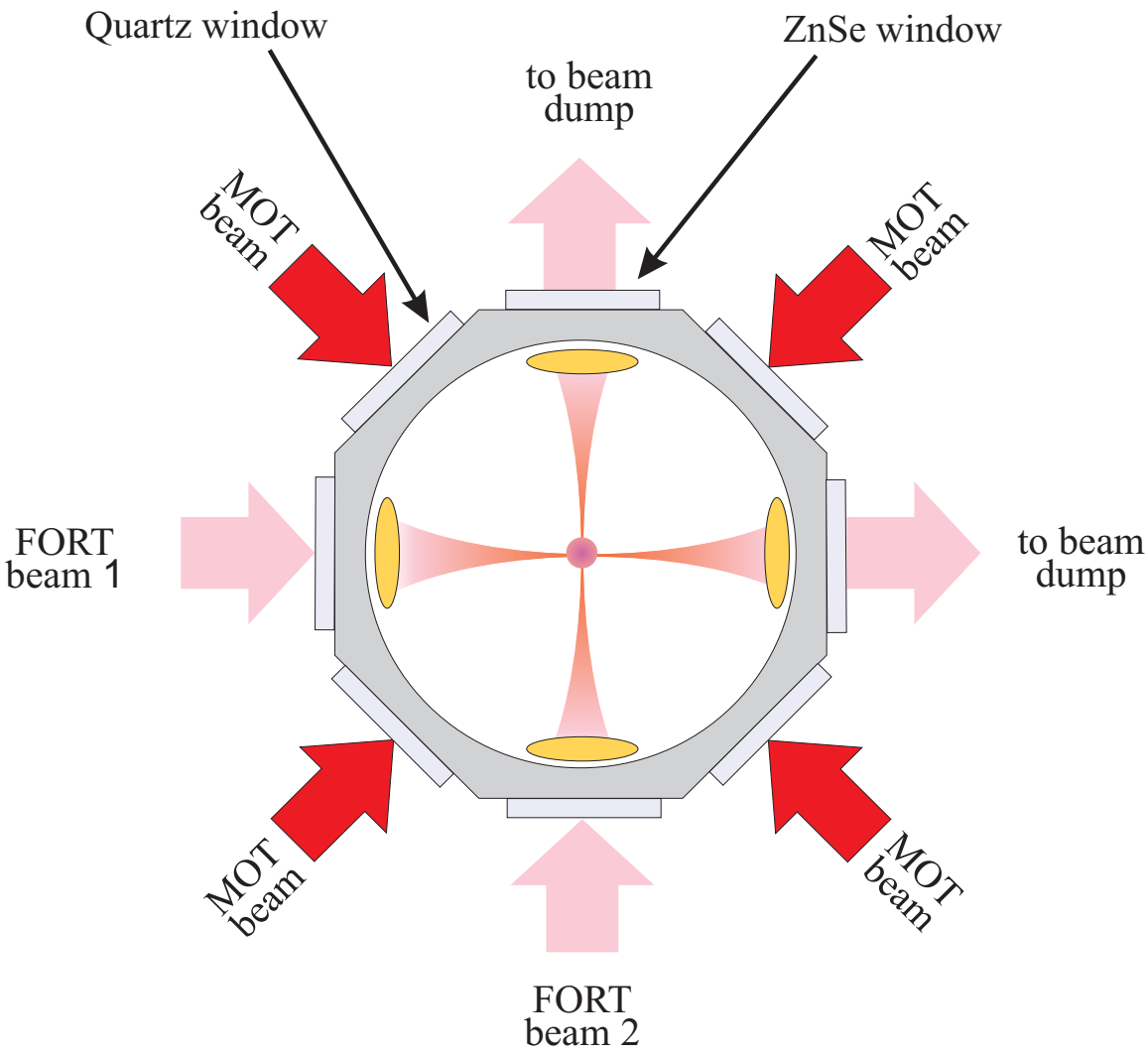

Figure 4.2. MOT and FORT beam geometry relative to the octagonal multi-port champer.

The ultra high vacuum required for the experiments was prepared using three different pumps. First a Travac-b rotary vane vacuum pump was used as a roughing pump. The pump speed was 1.6 m^3/hour. The roughing pump can pump gases and vapors and evacuate the vacuum chamber to a pressure of about 0.1 Torr. It took only a few minutes for the Travac-b to reach such a pressure.

A Turbo-molecular pump was switched on after this stage for pumping the chamber to lower pressures. We used a Turbovac model# 151 C to pump the vacuum chamber down to pressures in the high-vacuum range. While the roughing and turbo pumps were working we started to bake out the vacuum chamber. In order to thermally isolate the chamber we made a cage around it and covered it with pieces of a thermal blanket. Using electrical heaters the temperature was raised to 200° C. The system was left at this temperature for 3 days to ensure that most of the water and other impurities outgassed from the chamber's walls. The ultimate pressure that we were able to observe using the turbo-pump during bakeout was $\approx 10^{-8}$ Torr. In the next stage, a Varian Valcon Plus 55 ion pump was used for further pumping the chamber. After 1-2 weeks of operation the vacuum reached the low 10^{-11} Torr.

4.2 Rubidium Dispenser

To make a BEC we needed a sample of atoms at low temperature and high density such that the atomic deBroglie waves started to overlap. For the following reasons we used Rb87 atoms.

i) The excitation frequency from the lowest to the first excited state is in the near IR region which makes it relatively simple to generate light using cheap diode lasers.

ii) It is easy to generate an atomic vapor of Rb87 atoms since rubidium has high vapor pressure even at room temperature.

iii) The collisional properties of Rb87 atoms make it easy to evaporatively cool them to ultra low temperatures.

We used a rubidium dispenser in our vacuum chamber as a source for the atoms. Rubidium dispensers have been widely used to provide pure atom sources in atomic research systems. In these dispensers, rubidium atoms are released from a metal surface when it reaches a critical temperature as it is heated by an electric current. After the current is switched off, the dispenser cools below the critical temperature and stops dispensing. Heat loss dominated by radiation results in a fast switch-off time constant of less than 10 s. It is important to find the correct current to operate the dispenser. Too low a current and the MOT will be very small, while too high a current and the vacuum (and consequently the life time of atoms in the MOT) will be adversely affected. In our experiments we applied different currents to the dispenser depending on its age. The current starts at around 2 A for a new dispenser and gradually increases to 4 A near the end of its life when the dispenser does not produce Rb atoms efficiently. We chose the operation current I_{op} as one in which the MOT loading time was about 20 s ($P \approx 10^{-11}$). Our Rb dispenser was a commercial product from SAES Getters (RB/NF/4.8/17FT10+10). To use a new dispenser it had to be run at high currents for several minutes to remove an oxide layer. Also, it is important to run a high current through the dispensers during the bake out to allow the absorbed water and any other impurities to outgas. These dispensers usually worked for about a year before they needed to be replaced with a new one. We installed three dispensers in the vacuum chamber in order to provide enough Rb87 for experiments during at least four years.

4.3 Optical system: Overview

Developing a stable laser optical subsystem was one of the most important parts in building the Bose-Einstein condensate apparatus. From the MOT to BEC creation and imaging, precision and rapid control of different laser frequencies and powers is required. All of the equipment necessary to prepare the cooling light beams was placed on a single optical table separated from the vacuum chamber. Since we

have two different experiments running in the lab the setup was designed to be cost effective by sharing some of the lasers between both experiments. In the following we will explain details of the optical setup which enables us to perform atom trapping and cooling experiments.

In our setup, a MOT cooling beam at 40 mW was created using a series of semiconductor laser diodes. A grating stabilized "Toptica Photonics DL 100" diode laser with 15 mW output power from was used as a master laser. This laser was locked to a frequency near the $F = 2 \rightarrow F' = 3$ transition of Rb87 atoms. The output of the master laser was directed to a high power home made diode laser (slave 1) to force this laser to follow the master laser. The output power of the slave 1 laser was about 110 mW and was divided into two parts. We used injection locking [70] with a double-pass acousto-optical modulator (AOM) configuration to force the slave to follow the master with a small frequency offset. The double pass configuration allowed us to change the frequency offset of the light used to inject the slave over a wide range (up to 80 MHz). By extending this principle we were able to inject two additional slave lasers following slave 1. Each of these slaves was used for one of the two MOT experiments.

Another grating stabilized "Toptica Photonics DL 100" diode laser was used as a repumping laser. The output from the repumping laser was locked on the $F = 1 \rightarrow F' = 2$ transition. This light was divided into two parts to provide repumping light for both MOT experiments. Each of these beams was transferred to the vacuum tables by an optical fiber after double passing through an acousto-optical modulator (repumping AOM). The repumping AOM for the BEC experiment was driven by an RF power supply whose amplitude could be controlled in order to vary the amount of light in the AOM's first diffraction order. This was critical to allowing efficient loading of the FORT.

4.4 Operating principles of the diode laser head DL 100

In the DL 100, light emitted from the front face of the laser diode was collimated by a multi-element lens with a very short focal length (diffraction limited) and then scattered from a diffraction grating. The grating was adjusted in the Littrow setup where the first diffraction order of the grating was reflected back to the laser diode as feedback. As the feedback of the grating is considerably higher than the feedback from the laser diode front face, the laser resonator consisting of the rear face and the grating starts oscillating. The free spectral range of this new resonator with a length of a few centimeters is substantially smaller than the one of the laser diode which has an internal cavity length of approximately 100 μm. The line width, therefore, is reduced to a typical value of 1 MHz compared to a 100 MHz line width for a free-running laser diode.

4.5 Design of the diode laser head DL 100

A Peltier element, which stabilizes the laser head temperature, is located on a solid base block which serves as a heat reservoir. The laser base plate was installed on top of the Peltier element by plastic screws. This electrically and thermally isolates the laser base plate from the base block. The laser, collimator, and grating holder are attached to the laser base plate by metal screws. A thermistor is cemented into the laser base plate in order to achieve an accurate temperature reading.

The laser diode is inserted into a drilled hole provided in the laser and collimator holder aligned by a ring and fixed by two screws.

4.6 Design of the home made diode lasers

The home made diode lasers used as slaves were similar to the DL 100 except for the elimination of the diffraction grating. Also, we used high power Sanyo diode lasers with 120 mW output power. The current in the diode laser was supplied

by a Thorlabs LDC500 Laser Diode Controller. A Thorlabs TEC2000 Temperature controller was used to monitor and stabilize the laser diodes' temperature (for a detailed discussion on the current and temperature controller circuits see reference [71]). For the later experiments three such diode lasers were used in the setup. One of them was injection locked directly to the master laser. Thus we made a copy of the master laser with very high power. This power was enough to be divided into two parts for both the BEC and Cold Atom apparatuses. After dividing, each beam travelled through a double pass AOM configuration. Depending on the AOM frequency shift, 5-10 mW of power remained in each beam after the double pass. This provided enough power to inject into another one of the slave diode lasers.

4.7 Optical isolation of the master diode lasers

Stray reflection of light from optical components into a laser can result in feedback which interferes with the stability of the laser. Considering the fact that we need to stabilize the diode laser frequency within a few MHz such reflections should be blocked before reaching the diodes. This is accomplished by using optical isolators. Although these isolators are factory made, it is useful to briefly review their operational concept. Optical isolators are passive, non reciprocal devices that utilize the phenomenon of magneto-optic rotation to isolate the source from reflections in an optical system. The heart of the optical isolator is a Faraday rotator, for example, Yttrium Iron Garnet-YIG (LPE and bulk) or Terbium Gallium Garnet-TGG single crystals.

In 1842, Michael Faraday discovered that the plane of polarized light rotates while transmitting through glass (or other material) that is contained in a magnetic field. The direction of rotation is dependent on the direction of the magnetic field, and not on the direction of the propagating light (non-reciprocal). This capability allows the realization of many schemes to manipulate laser light in ways that are otherwise impossible or, at least, much more difficult to implement. By far, the most

common application of Faraday rotators is their use in optical isolators, devices used to protect laser sources from harmful back reflections. A basic optical isolator is shown in Figure 4.3. Light from a linearly polarized laser source enters an aligned beam-splitting polarizer from the left. It then proceeds through a Faraday rotator which is tuned to provide a 45° rotation of the polarization direction for the particular laser wavelength. A second polarizer is added to the assembly on the opposite end of the rotator and aligned at 45° with respect to the original polarizer (see Fig. 4.3 (a)). This last polarizer is necessary because the polarization of light reflected back towards the laser source may not be the same as that in the forward direction. Any orthogonal polarization component accidentally produced will now be rejected by the polarizer-rotator combination shown in Fig. 4.3 (b). In Figures 4.3 (a) and (b) we have traced the changes through the isolator of the diode beam and reflected beam respectively.

4.8 Optical isolation of the slave diode lasers

Since the slave diode lasers need to be injection locked to the master laser a conventional isolator can not be used in its setup or no light from the master would get to the slave. A small change in the isolator can allow the injection beam to propagate into the diode laser while still eliminating any stray reflected light. Figure 4.4 (a) illustrates the concept of such a setup. As shown in Fig. 4.4 (a) there is a half wave plate in front of the first polarizer which is set to rotate the polarization plane of the laser beam by 45 degrees. The first polarizer is rotated by the same amount to pass through the maximum amount of the light. The Faraday rotator adds another 45 degrees to the polarization direction such that the beam passes through the last polarizer. The optical paths and each equipments' effect on the polarization of the injection and reflected light is shown in Fig. 4.4(b) and (c).

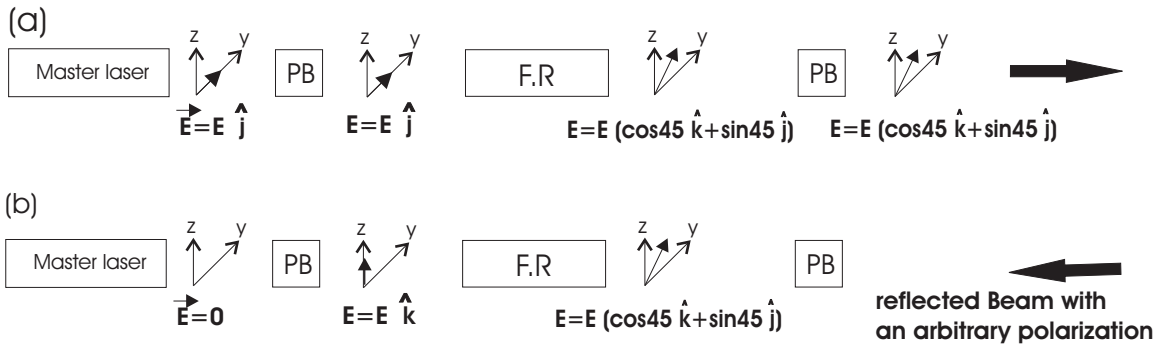

Figure 4.3. Isolator set up.

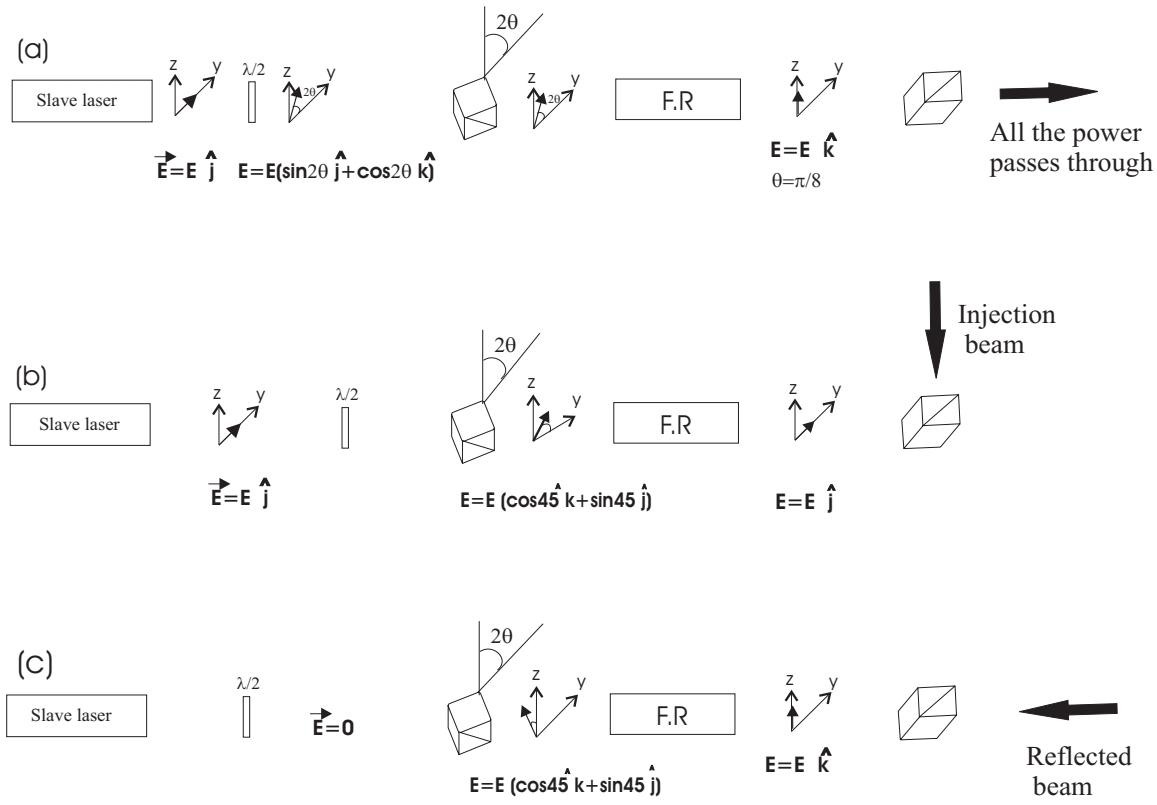

Figure 4.4. Isolator set up.

4.9 Frequency control

For our experiments it was crucial that we had precise control of the laser frequency and intensity. Three different frequencies for the laser beams were needed on the way towards realizing a condensate. These were:

i) Light with -15 MHz detuning from the $F = 2 \rightarrow F' = 3$ transition to make the MOT (MOT beam).

ii) Light with -80 MHz detuning from the $F = 2 \rightarrow F' = 3$ transition for optical molasses cooling of the atoms in the MOT.

iii) Light resonant with the $F = 2 \rightarrow F' = 3$ transition for imaging the trapped atoms and the condensate.

iv) Light tuned from the $F = 1 \rightarrow F' = 2$ for repumping (this is discussed in more detail in the following section).

Furthermore, there were two intensity requirements that had to fulfilled during the experiments:

i) High intensity (> the saturation intensity) for the MOT beams was required in order to create a highly populated MOT. We will see later that the loading efficiency from the MOT to the FORT was only about 10% so that a MOT with large number of atoms was important in order to realize a condensate using all-optical methods.

ii) Fast switching of the light beams. The experiments should be performed much faster than the time scales in which mechanical shutters typically respond.

These requirements were met by using AOMs in the optical set up. We used a master AOM to manipulate the slave laser frequency. However, the beam was deflected at an angle proportional to the frequency shift. Such a change in the direction of the light was highly undesirable particularly because the light was directed into the slave diode laser for injection locking. In order to overcome this problem the modulator was set in a double pass configuration as shown in Fig. 4.5. Here the modulator was placed at the center of a one-to-one telescope and thus in the focal plane of each lens. In this configuration the deflected beam was perpendicular to the

retro-reflecting mirror, independent of the angle of deflection and thus independent of the frequency shift. This double pass, through the quarter wave plate in between the lenses, rotates the polarization of the reflected beam 90° compared to the original beam. Therefore, the polarizing cube in front of the first lens was able to separate the incoming and reflected beams. The frequency shift and the light paths are given in Fig. 4.5. In our set up the master AOM was a 80 MHz center-band frequency deflector with a 20 MHz band width. In practice this allowed us to sweep the frequency of the slave light over about 80 MHz. Furthermore, to build a switch for the MOT beams the output light of the slave laser passed through another modulator, the slave AOM. The slave AOM modulated the frequency by a fixed amount of -80 MHz. The first order diffraction after the slave AOM was coupled to a fiber optic cable and transported to the vacuum table. Since the power in the deflected beam was a function of the RF power, switching off the RF reduced the power through the fiber to near zero in less than a μs. The master laser was locked to the cross-over transition of the $F = 2 \rightarrow F' = 2 - 3$. By changing the frequency of the master AOM the slave laser frequency was manipulated. This process was controlled by a Labview program.

4.10 Repumping laser set up

There is small probability that the slave laser will excite transitions other than the $F = 2 \rightarrow F' = 3$. Atoms excited to the $F' = 1$ or $F' = 2$ state can spontaneously decay to the $F = 1$ state. Such a process prevents the atoms from interacting with the trapping beams and rapidly destroys the trap. Therefore, in the conventional approach to realize a Rb87 MOT a repumping laser is also used which is locked to the $F = 1 \rightarrow F' = 2$ transition. This light returns atoms in the $F = 1$ state to the cycling transition necessary for efficient MOT operation. However, there are other considerations for the repump light when loading an optical trap. On the road towards realizing a condensate we had to load as many atoms as possible from the

MOT to the optical trap. The efficiency of this process could be enhanced greatly if the repumping beam power was reduced after loading the MOT. To have control of the repumping beam power the repump laser was locked to the cross-over transition of $F = 1 \rightarrow F' = 1 - 2$. A double pass AOM arrangement was then used to shift the frequency up to the $F = 1 \rightarrow F' = 2$ transition. For this AOM we used an RF driver whose power could be controlled with a low voltage signal from a computer. This allowed us to vary the repumping beam power.

4.11 Saturated absorption spectroscopy

In laser cooling experiments, two methods are generally used to lock the laser frequency to the desired hyperfine transition. These are saturation absorption spectroscopy and DAVLL locking. In the work of this thesis saturated absorption spectroscopy was used. This technique will now be explained.

First consider the hyperfine structure of the isotope of Rb87, a structure which results from the electronic spin interactions with the spin of the nucleus. The saturation absorption spectroscopy setup to and the energy level structure of Rb87 are shown in Figs. 4.6 and 4.7. Since the hyperfine structure covers a frequency range smaller than the Doppler broadened spectrum, we must use more than one laser beam to distinguish the fine spectral lines. When the laser comes to the beam splitter, most of it will pass through (becoming the saturating beam) and only a small part of it will be reflected (this is called the probe beam). The saturated and probe beam nearly overlap each other but travel in opposite directions inside the rubidium cell. The absorption cross section for an atom with the velocity component $\overrightarrow{v_z}$ on a transition $|1> \rightarrow |2>$ is [72]

$$\sigma(\omega, v_z) = \sigma_0 \frac{(\gamma/2)^2}{(\omega - \omega_0 - kv_z)^2 + (\gamma/2)^2} \tag{4.1}$$

where σ_0 is the maximum absorption cross section at the center of the atomic transition. Due to saturation, the population density of the lower level, $N_1(v_z)dv_z$, decreases within the velocity interval $dv_z = \gamma/k$ while the population density, $N_2(v_z)dv_z$, of the

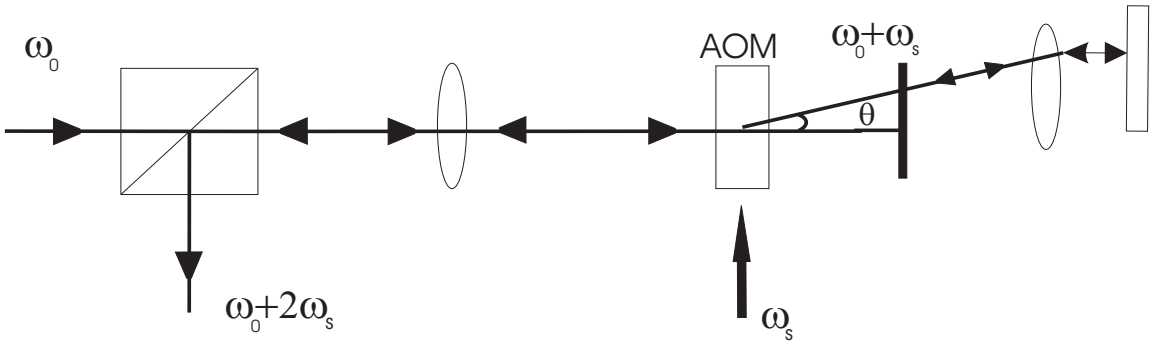

Figure 4.5. Double-pass set up.

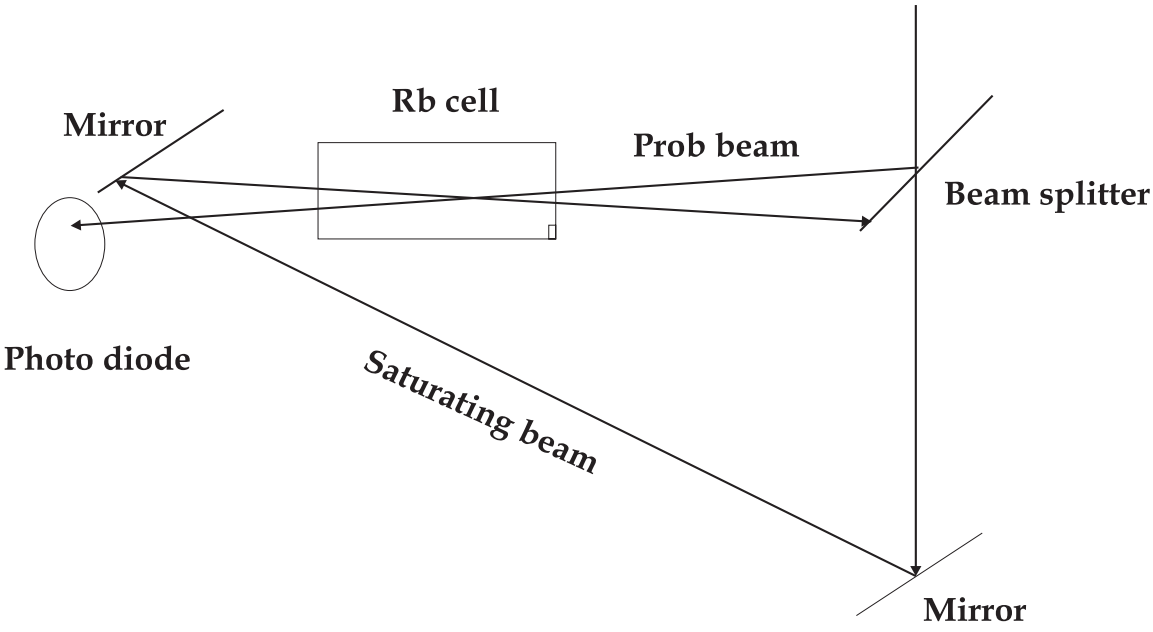

Figure 4.6. Schematic of the saturation absorption spectroscopy setup.

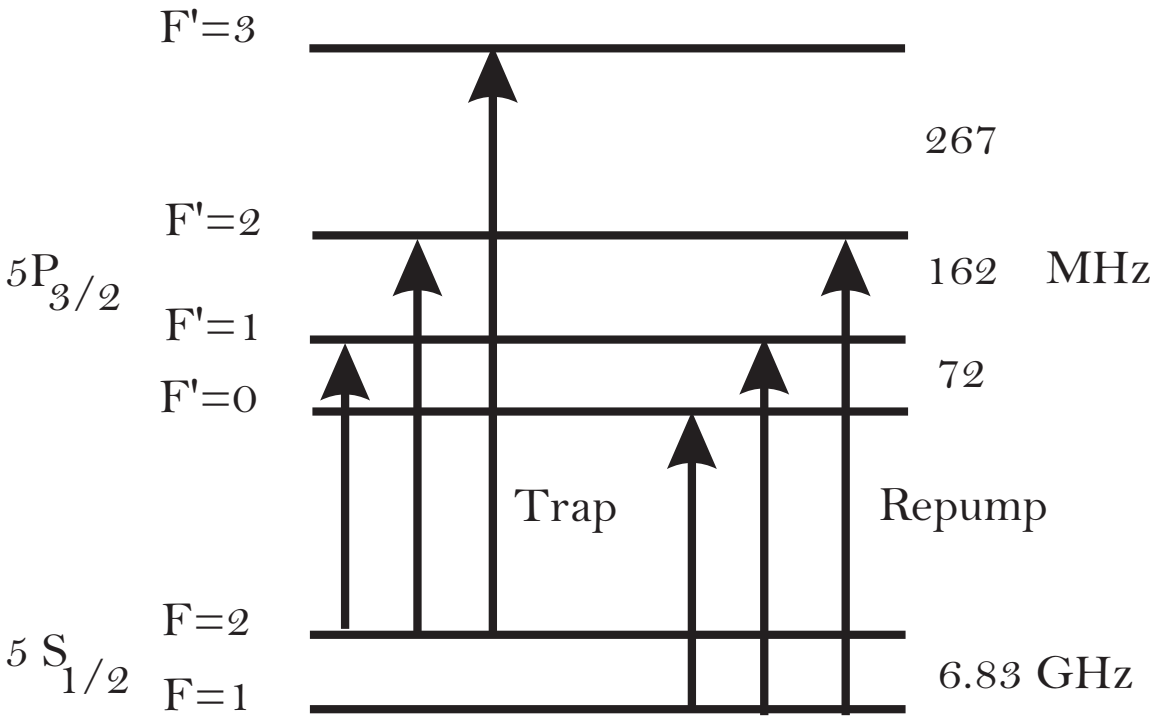

Figure 4.7. Energy level structure of the Rb87 D2 line. The master laser was locked to the cross-over transition of $F = 2 - F' = 3$ where the repumper laser was locked to the cross-over transition of the $F = 1 - F' = 2$.

upper level $|2\rangle$ increases correspondingly. On the other hand atoms with velocity components in the interval v_z to $v_z + dv_z$ give the contribution

$$d\alpha(\omega, v_z) = \delta N(v_z)\sigma(\omega, v_z) \tag{4.2}$$

to the absorption coefficient $\alpha(\omega, v_z)$. Therefore the saturation beam burns a hole in the absorption coefficient profile (Lamb dip).

The probe beam is sufficiently weak to cause no extra saturation. Therefore the absorption coefficient for a tunable probe beam is an unsaturated Doppler profile $\alpha_0(\omega)$ with a saturation dip at the probe frequency $\omega = \omega_0$. The hyperfine structure of Rb87 determined by saturating absorption spectroscopy is given in Fig. 4.8.

4.12 Polarization

The next step was to set the polarizations of the six MOT beams. The orientation of the respective circular polarizations were determined by the sense of the current and orientation of coils used to produce the magnetic field gradient. The four beams which propagate through the chamber perpendicular to the coil axis should all have the same circular polarization (relative to the beam direction) while the two beams which propagats along the coil axis should have the opposite circular polarization to the first four beams. Although in principle it is possible to initially determine and set all polarizations correctly with respect to the field gradient, in practice it is much simpler to set the polarizations relative to each other and then try both directions of current through the coils to determine which sign of magnetic field gradient makes the trap work. A polarization analyzer was built to set the circular polarizations (see Fig. 4.9). The analyzer consisted of a polarizing beam splitter and a quarter wave plate. To initially set the wave plates' orientation we used the fact that double passing a linearly polarized beam through a quarter waveplate rotates the polarization 90 degrees if the polarization direction makes a 45 degree angle with the waveplate axis. Light was sent through the beam splitter cube and was reflected after the wave plate. The waveplate was then rotated to maximize the power of ray 3 in Fig. 4.9 (a). To

make the trapping beams circularly polarized the light was passed through the wave plate of the analyzer. Then another quarter wave plate was installed in front of the analyzer and rotated to maximize the beam which was either passing through the beam splitter cube or reflecting from it Fig. 4.9 (b). Removing the analyzer left the trapping beam circularly polarized before going through the chamber. At the other side of the vacuum chamber the beam passed through another quarter wave plate and reflected back on itself. Therefore, inside the chamber in each direction, beams have a σ^+-σ^- scheme. The intersection region between the laser beams inside the chamber was about 2.2 cm^3. This was the volume in which the MOT was realized.

4.13 Magnetic coils

To provide the magnetic field required for the MOT, we built a set of water cooled anti-Helmholtz coils. Each of the coils had a diameter of 22.5 cm with 86 turns of wire carrying 12 A of current. The separation between the coils was 12.5 cm. These coils made a magnetic field with a gradient of approximately 7 G/cm. To cancel out the effect of the Earth's magnetic field we used a pair of Helmholtz coils in each direction (nulling coils). Finally, using this setup we trapped around 40 million atoms in the MOT.

4.14 Time-of-flight

This section presents one of our early experiments that used a time-of-flight (TOF) technique to extract the velocity distribution in the MOT and consequently its temperature. The optical arrangement is shown in Fig. 4.10. The magnetic field and laser beams creating the MOT were turned off and the atoms in the MOT fall down under the influence of gravity. Using the TOF, the velocity distribution was determined by observing the amount of light absorbed from an on resonant laser beam as a function of time. This beam propagated horizontally about 10 cm below the MOT.

Fig. 4.11 shows typical data taken for a TOF experiment. A Gaussian fit to the velocity distribution shows that the trapped atoms had a thermal temperature of 19μK. In the BEC experiments we used a direct imaging method (with a camera) for all of these measurements. This method is explained fully in the next section.

4.15 Optical Dipole Trap

The light for the optical trap originated from a 50 Watt RF excited CO_2 laser. The setup used for creating two beams is shown in Fig. 4.12. The output beam of the laser passed through an AOM. The zeroth order of the output from the AOM was then directed to a beam dump and the first order toward another AOM. Two 2.5 cm diameter ZnSe viewports allowed us to transmit the the CO_2 laser beams into the vacuum chamber. The focusing arrangement for the CO_2 beam consists of a 2$\times$ beam expander followed by a 3.75 cm focal length lens which is placed within the vacuum. The AOM's are driven by amplified 40 MHz RF signals. The 40 MHz RF signal for the first AOM passed through two MiniCircuit electronics attenuators, model ZAS-3, before entering the amplifier. The controllers of the attenuators were connected to separate analog terminals controlled by a computer. Depending on the voltage applied to the controllers the RF power changed, giving computer control of the total power and hence the optical trap's well depth. Therefore the evaporative cooling was performed using this AOM. Another advantage of using the attenuators in the setup was that the trap could be switched off in less than 1 μs which was crucial for the consistency of the time of flight experiments.

In the same way, the efficiency of the second AOM was controlled in order to change the ratio of the power in the FORT beams. This streamlined the control of the optical trap geometry (single or crossed beam configurations). The main complexity that arrived from introducing the attenuators was that the total power was not proportional to the control voltage. Thus accurate control of the ramp-down required us to measure the power versus control voltage in order to build a lookup table .

4.16 CO_2 beam optics and detection

Unfortunately, the usual optics for the MOT were not useful for CO_2 beams because of the high absorption of glass and quartz at the 10.6 μm wavelength of the laser. One of the best materials with a low absorption coefficient at this wavelength was Zinc-Selenide (ZnSe). Although the technology for mass production of this material is well developed the optical components are usually more expensive than those for visible wavelengths. When working with CO_2 beams proper eye goggles should always be used and caution taken, since only a fraction of a Watt is enough to seriously damage the eyes. We used thermal plates to detect and align the beam. A thermal image plate displays IR laser beams through the use of thermal-sensitive phosphors. These phosphors fluoresce when illuminated by an ultraviolet light (3600A). The intensity of the fluorescence decreases with increasing temperature. When an IR laser beam strikes the thermally sensitive surface, the absorbed energy raises the surface temperature and produces a corresponding thermal image. The pattern produced appeared as a dark image on a bright fluorescent background. Different sensitivity ranges were obtained by using different phosphors and by varying the amount of thermal insulation between the phosphors and the anodized aluminum heat sink. Any long wavelength, ultraviolet light could be used to illuminate the surface, but Macken Instruments' Lamp Model 22-UV was the one that we used. Its small size and high-illumination level permitted it to be conveniently positioned in the working area.

4.17 CO_2 beam alignment

Since the CO_2 beam frequency is far-off-resonant from the electronic transition frequency of the Rb atoms, it was very difficult to align the beam with the MOT. Initially we aligned the CO_2 laser trap with the MOT using the following method. We aligned a 780 nm laser beam (probe beam) on top of a He-Ne laser. The probe beam

was aligned such that it destroyed the MOT when we allowed it into the chamber. By burning a hole in a piece of paper with the CO_2 laser beam, we could overlap the CO_2 beam along the same path as the He-Ne beam and therefore ensure the beam passed close to the MOT. Since the Rayleigh length is short and the focus is tight, this method does not locate the focus of the beam on the MOT at first try. For final alignment, the CO_2 beam was turned on and off periodically and the MOT moved using the nulling coils until the fluorescence intensity changed in the MOT. However, later on when we improved the setup to load more atoms in the MOT the intensity fluctuation was not observable anymore and the method was not very useful.

To overcome this difficulty, we devised a method which allowed us to observe the position of the CO_2 laser beam in real time directly on an inexpensive CCD camera that normally monitors the MOT. To accomplish this, it was necessary to improve the contrast between the atoms trapped in the MOT and those trapped in the FORT. Several techniques will work; for example, increasing the detuning of the MOT light from resonance or reducing the intensity of the MOT light. A similar effect is obtained if these operations are performed on the re-pumping light. With any one of these methods, the brightness of the MOT and the effect of its near resonant light on pushing atoms out of the FORT can be reduced. However, there can still be enough near-resonant light present in the MOT beams to cause atoms that are contained in the FORT to fluoresce and hence make the FORT beam visible. Using these techniques greatly simplifies alignment of the CO_2 laser beam, turning a task which could previously take several days into one that can be performed in few minutes [73].

4.18 Imaging system

Because of the poor response of the eye at 780 nm, the trapped atoms can be seen with the unaided eye only if the lab is very dark. Therefore an observing device is required for aligning. One can use a standard IR fluorescent card or a piece of

white paper (on which an image of the MOT can be formed) if the room is darkened. However, it is highly convenient to have a CCD TV camera to monitor the MOT inside the vacuum chamber. The security cameras work well for this purpose. They show the cloud of trapped atoms as a bright white glow.

Quantitative measurements of the cloud properties is more involved. In general there are two methods for quantitative measurements, fluorescent and absorption imaging [74]. In fluorescent imaging atoms are driven to saturation and the scattered photons are imaged. The absorptive technique, which is used in our lab, is also based on the resonant interaction of the light with the atoms. The atoms are exposed to a 50 to 60 μs pulse from a 1 cm diameter weak laser beam, 120 nW, on resonant with the $F = 2 \rightarrow F' = 3$ transition. The intensity of the beam will be reduced by the scattering of photons from the beam by the atoms. Thus the atoms effectively cast a shadow in the beam which can be imaged on a high resolution CCD camera. In order to calculate the number of atoms we use the fact that the absorption rate for a low intensity laser beam travelling in the z-direction is [38],

$$\frac{dI}{dz} = -\sigma n I, \tag{4.3}$$

where σ is the scattering cross section, n is the density of atoms and I is the imaging beam intensity. The solution of Eq. (4.3) is $I(x,y) = I_0(x,y)exp(-\sigma\tilde{n})$ where $\tilde{n}$ is the column density. In order to find $I(x,y)$ usually we take 3 images. One image is taken when there is no laser light to account for background noise. This gives us an intensity we denote I_b. Two more images of the beam are taken with, I_1, and without, I_0, the atomic cloud. The intensity profile $I(x,y)$ is then given by,

$$I(x,y) = \frac{I_0 - I_b}{I_1 - I_b}, \tag{4.4}$$

The number of atoms can be obtained by integrating over the column density which in terms of the digital images we have taken is given by,

$$N = -\frac{S}{\sigma} \sum_{pixels} \ln(I), \tag{4.5}$$

where the sum is over all of the pixels and S is the scaled area of a pixel which is $13\mu m^2$ for our CCD camera. Fig. 4.13 depicts our setup for the imaging system. A 4* microscopic objective was used to magnify the image [75,76]. A gaussian fit to the intensity profile determines the cloud size. The temperature of the cloud was determined by imaging the cloud after different expansion times and determining the ballistic expansion rate of the cloud. Although the imaging system was primarily used to observe the BEC and FORT, it can also take images of atoms in the MOT. Fig. 4.14 shows one such picture taken from the MOT. However, the discussion for determining the cloud size is not valid for a BEC since Bose statistics affects the cloud profile.

4.19 BEC

We have built the vacuum chamber for atom trapping and cooling to realize BEC. After 1-2 weeks of operation the vacuum reached 10^{-11} Torr. The FORT lifetime was 5 to 6 seconds at this pressure range. Using this setup the first BEC of Rb87 atoms was observed on August 2004. To realize a condensate the MOT was formed with a 20 G/cm magnetic field gradient, and by two 2.5 cm diameter, 20 mW beams. The FORT and MOT alignment was accomplished using the method in Ref. [73] which was also explained earlier in this Chapter. The following procedure was used to load the FORT from the MOT. First the MOT was loaded for 25 seconds from the background vapor while at the same time the CO_2 laser remained switched on. Then, as a key step in efficiently loading the FORT, the repump intensity, 1.9 mW, was reduced by a factor of about 10 to make a temporal dark SPOT [77,78]. This reduction in the repump power occurred 50 to 100 ms before switching off the MOT trapping beams. Alongside reducing the repump power, the trapping beam detuning was changed to -80 MHz for further laser cooling. This also ensured that our atoms always saw the MOT beams as negatively detuned even after considering the differential ac-Stark shift between the ground and excited states [77,79,80]. Finally, the main MOT beams

were extinguished (which was accomplished by using fast mechanical shutters) and the MOT magnetic field was ramped to zero in a 10 ms time frame. The earliest time that we could image the FORT was 100 ms after releasing the MOT. This ensured that any untrapped atoms had sufficient time to fall away from the FORT under the influence of gravity. Time-of-flight measurement showed the temperature of the trapped atoms in the FORT was $\approx 70\mu$K. Also, the phase space density was $\approx 10^{-3}$ which was enough to initiate the evaporative cooling. For evaporative cooling we used a trial and error method by maximizing the phase space density at each step of the evaporative cooling stage. This was cautiously done by changing the amount of the reduction in the FORT power and the wait time in each step for rethermalization and then observing the phase space density. Our final result was in very good agreement with exponential decay of the FORT beam power with a time constant of 2 seconds. Note that this was shorter than the FORT life time. In the latest version of the experiment the FORT power is ramped down with a program which uses a power law form. Figures 4.17, 4.18 and 4.19 depict the observed evolution of phase space density, cloud temperature and FORT population versus the evaporation time. To create these figures atoms were released from the FORT and imaged 10 ms after each evaporation step.

As the evaporation proceeded the remaining thermal cloud got colder and at around 400 mW of laser power, the bimodal distribution arises. At a trap power of 200 mW the cloud was almost pure condensate with $\approx 30 \times 10^3$ atoms. Figure 4.20 shows a typical absorption image of the condensate. For comparison the condensate is shown with two other absorption images of the cold atoms before and at the BEC transition.

In the following chapters we present other experiments that we have conducted using the setup that has been described here.

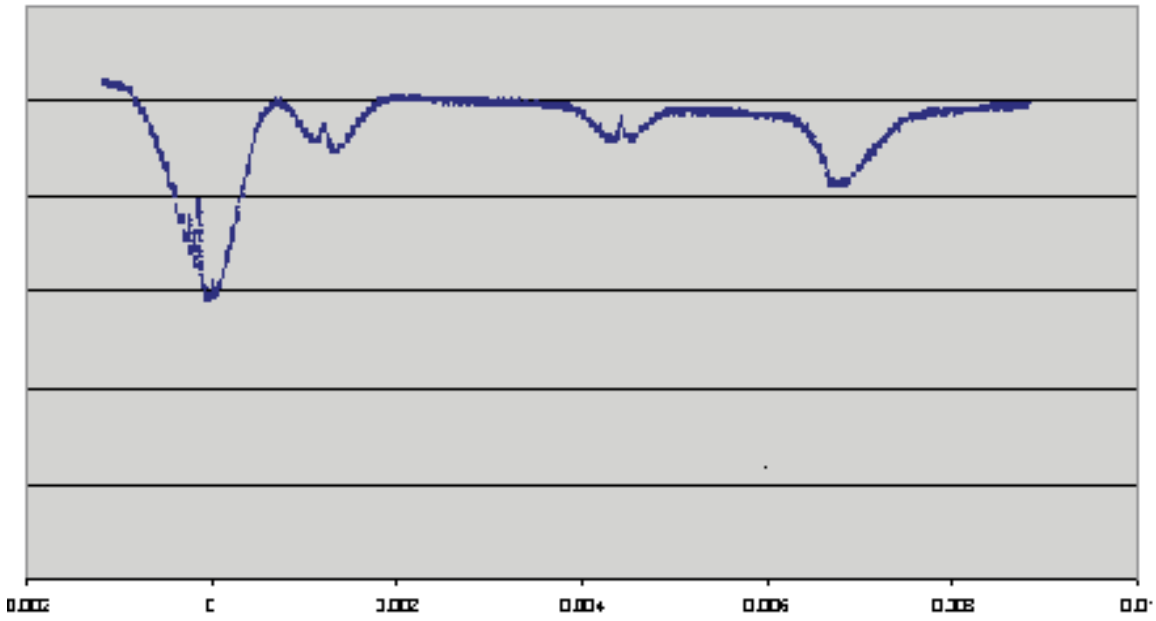

Figure 4.8. The D2 line hyperfine structure of Rb85 and Rb87 observed using saturation absorption spectroscopy.

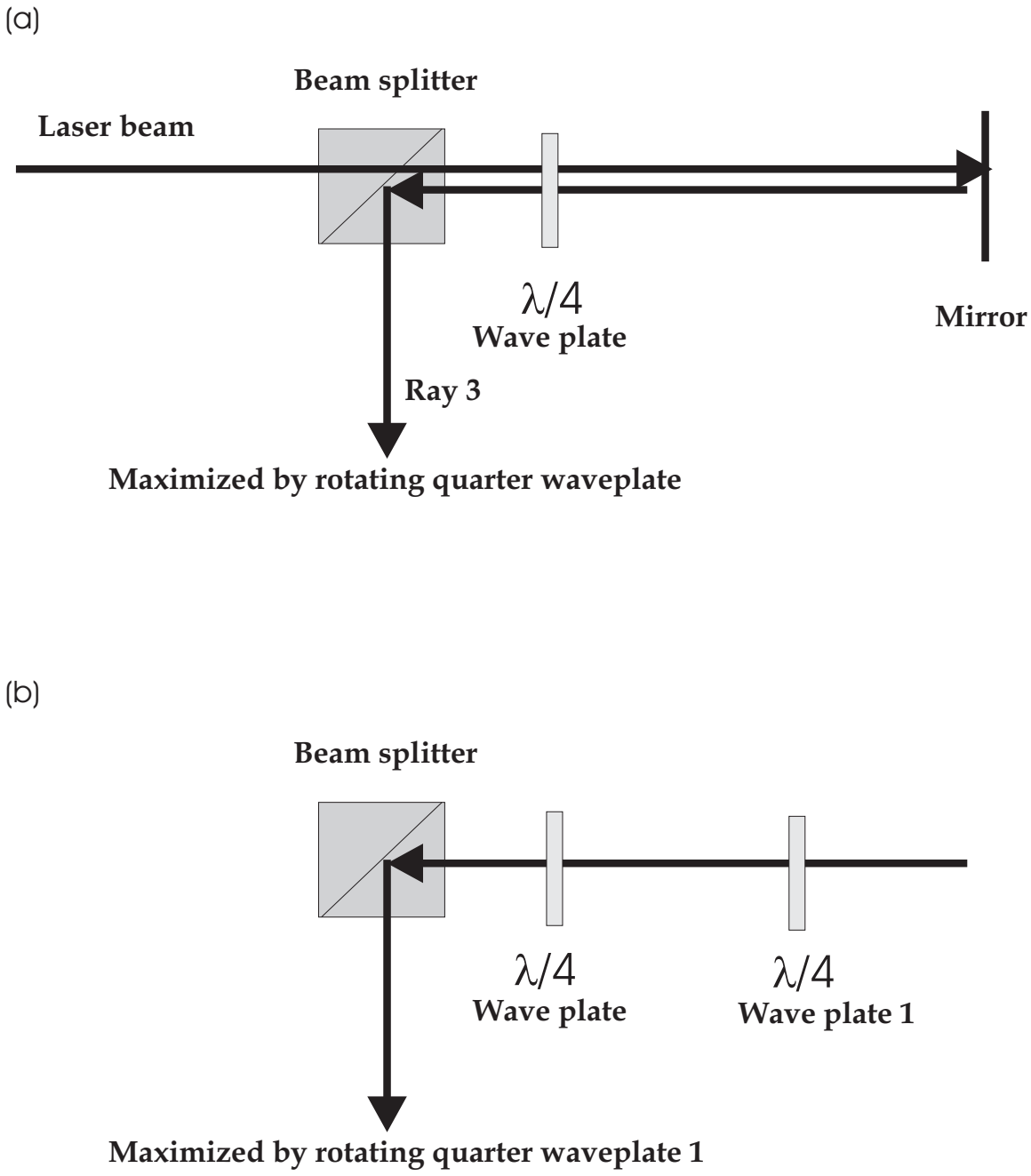

Figure 4.9. (a) Schematic to set the circular polarization analyzer. (b) Making a laser beam circularly polarized using the circular polarization analyzer.

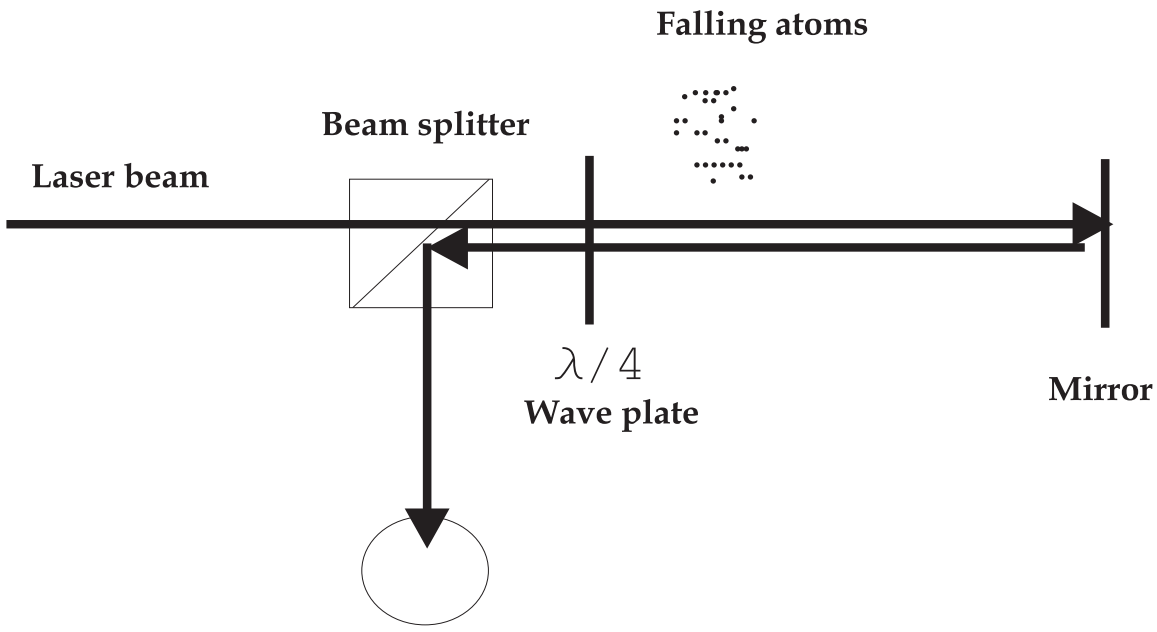

Figure 4.10. The time-of-flight apparatus (TOF). The location of the two counter-propagating laser beams resonant with $F = 2 \rightarrow F' = 3$ transitions in Rb87. The beam propagats horizontally about 10 cm below the MOT.

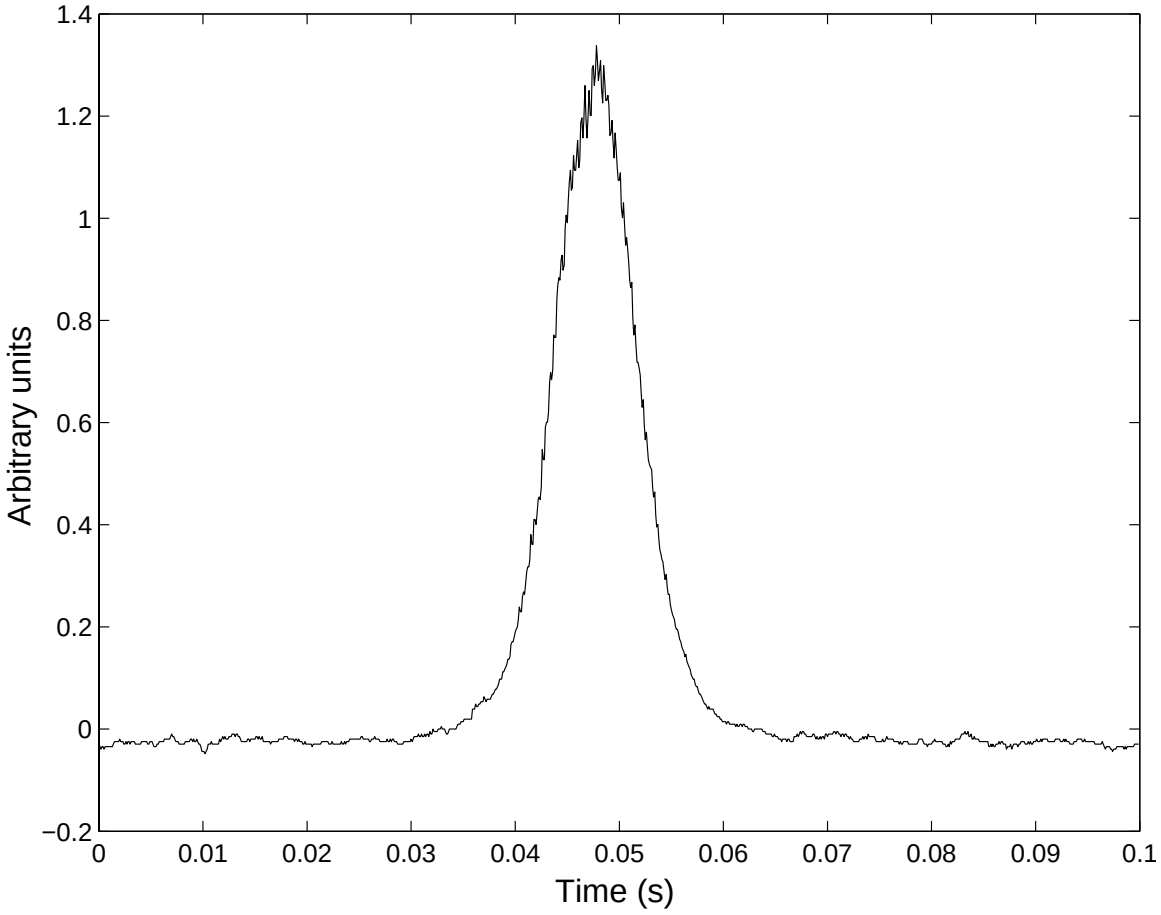

Figure 4.11. Observed TOF data. The FWHM is 9.2 ms which corresponds to a thermal temperature of $19\mu K$.

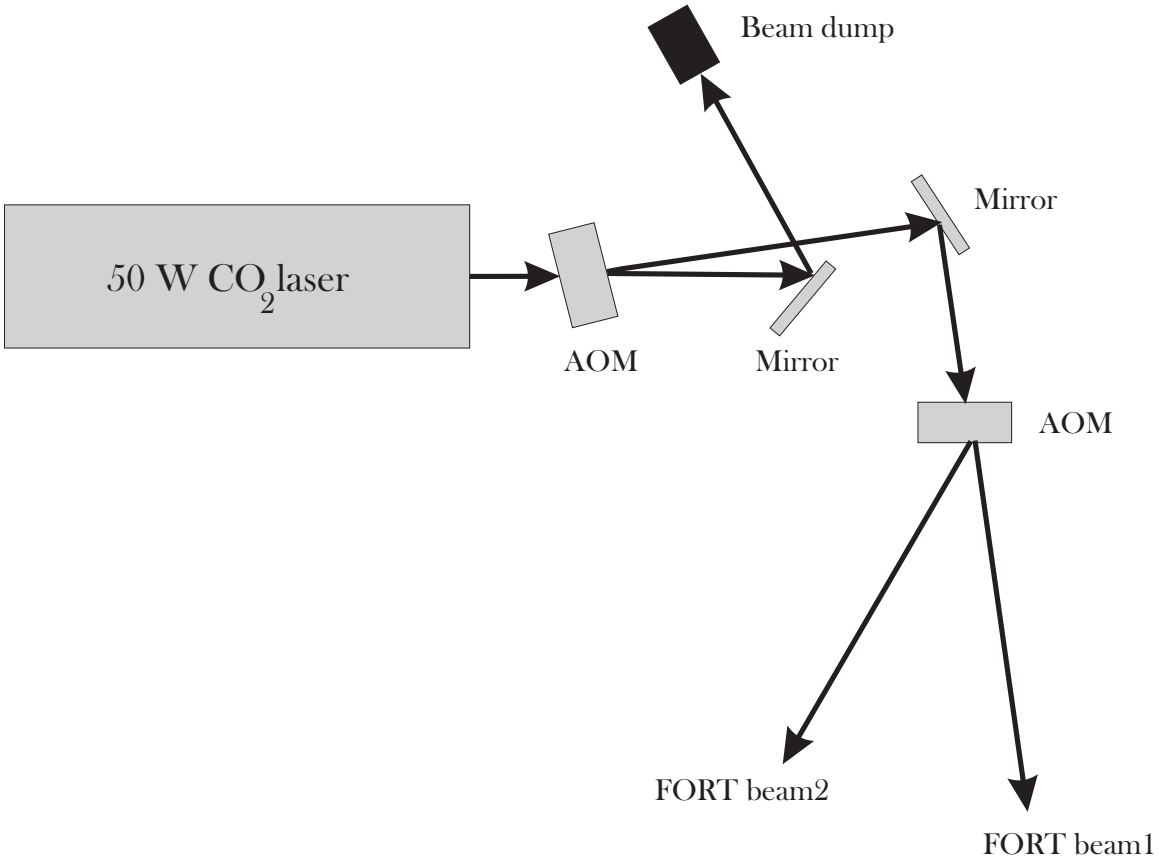

Figure 4.12. Optical arrangement used to create the CO_2 optical trap beams.

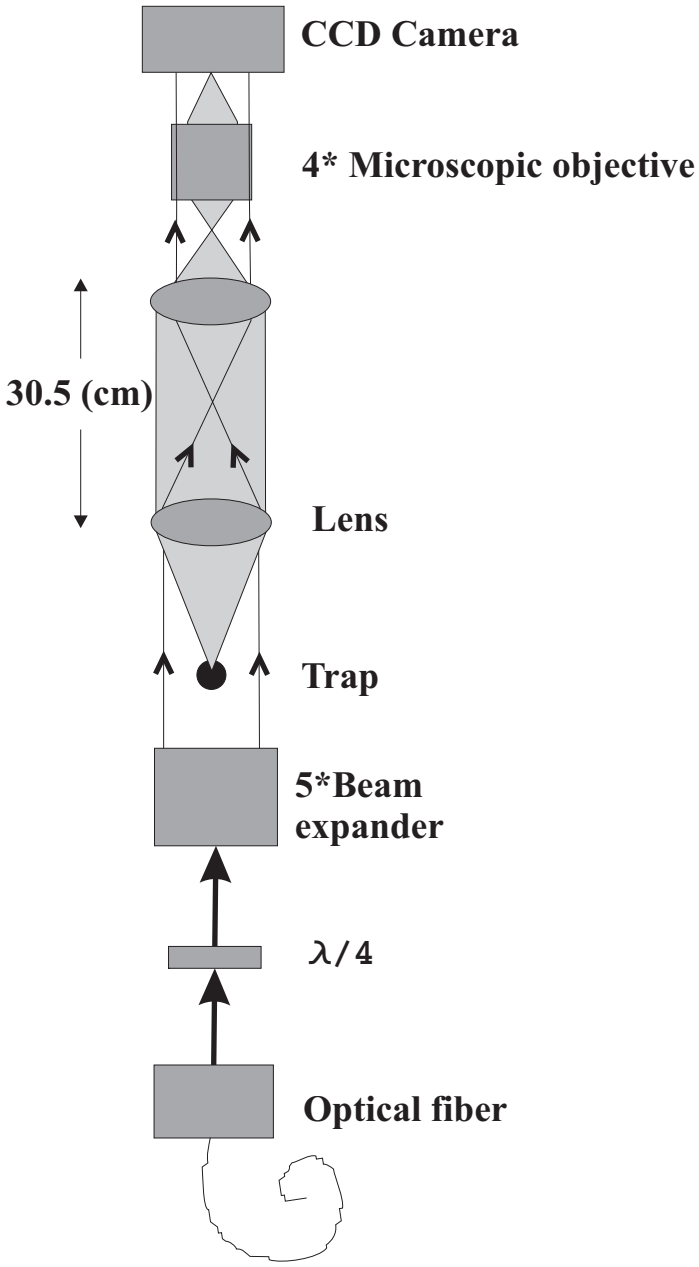

Figure 4.13. Setup for the imaging system.

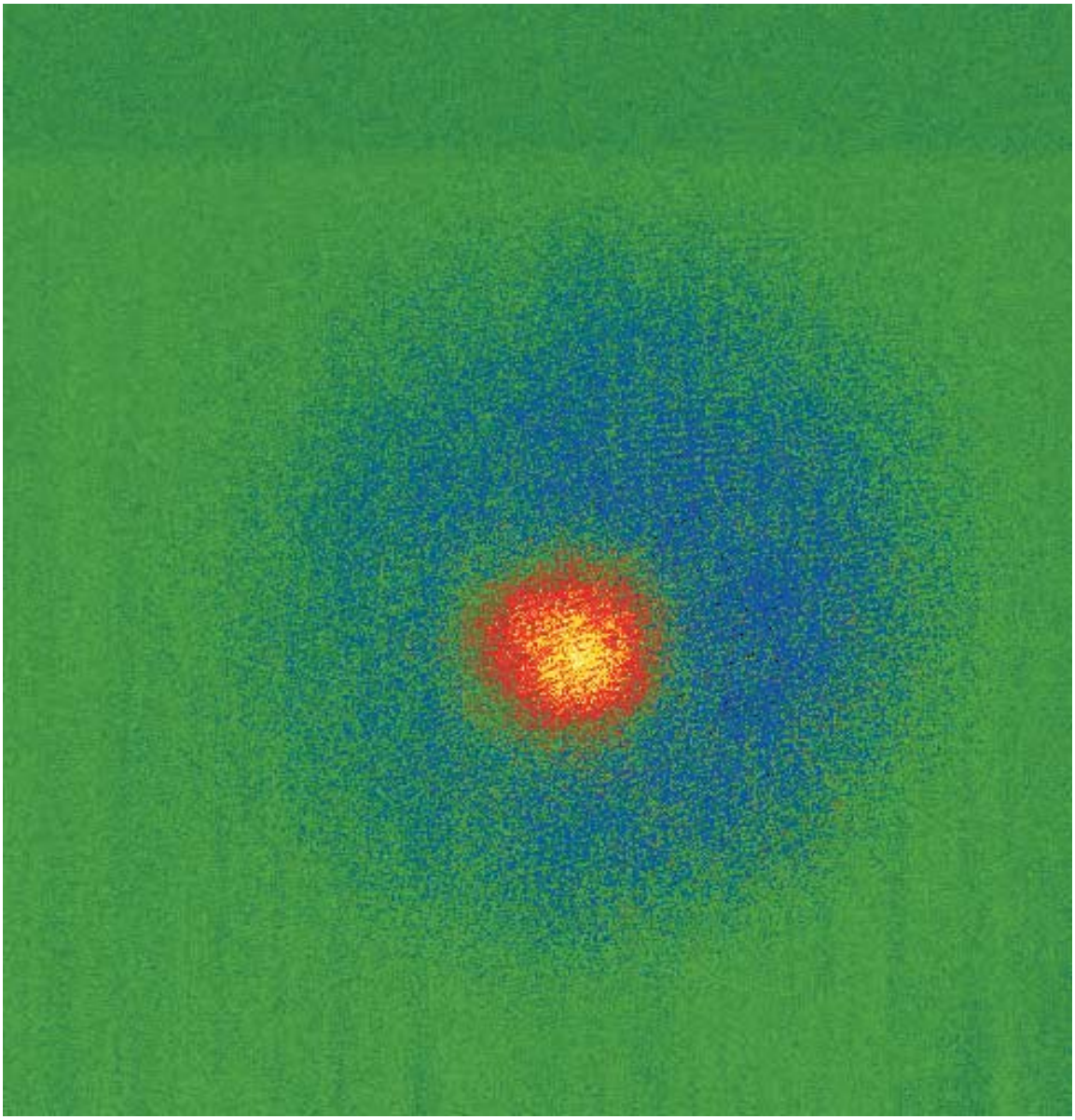

Figure 4.14. Absorption image of the loud of atoms in the MOT. The current in the magnetic coils was 10 A, which produced a magnetic gradient of about 6 G/cm. Approximately 10^7 atoms are trapped in the MOT.

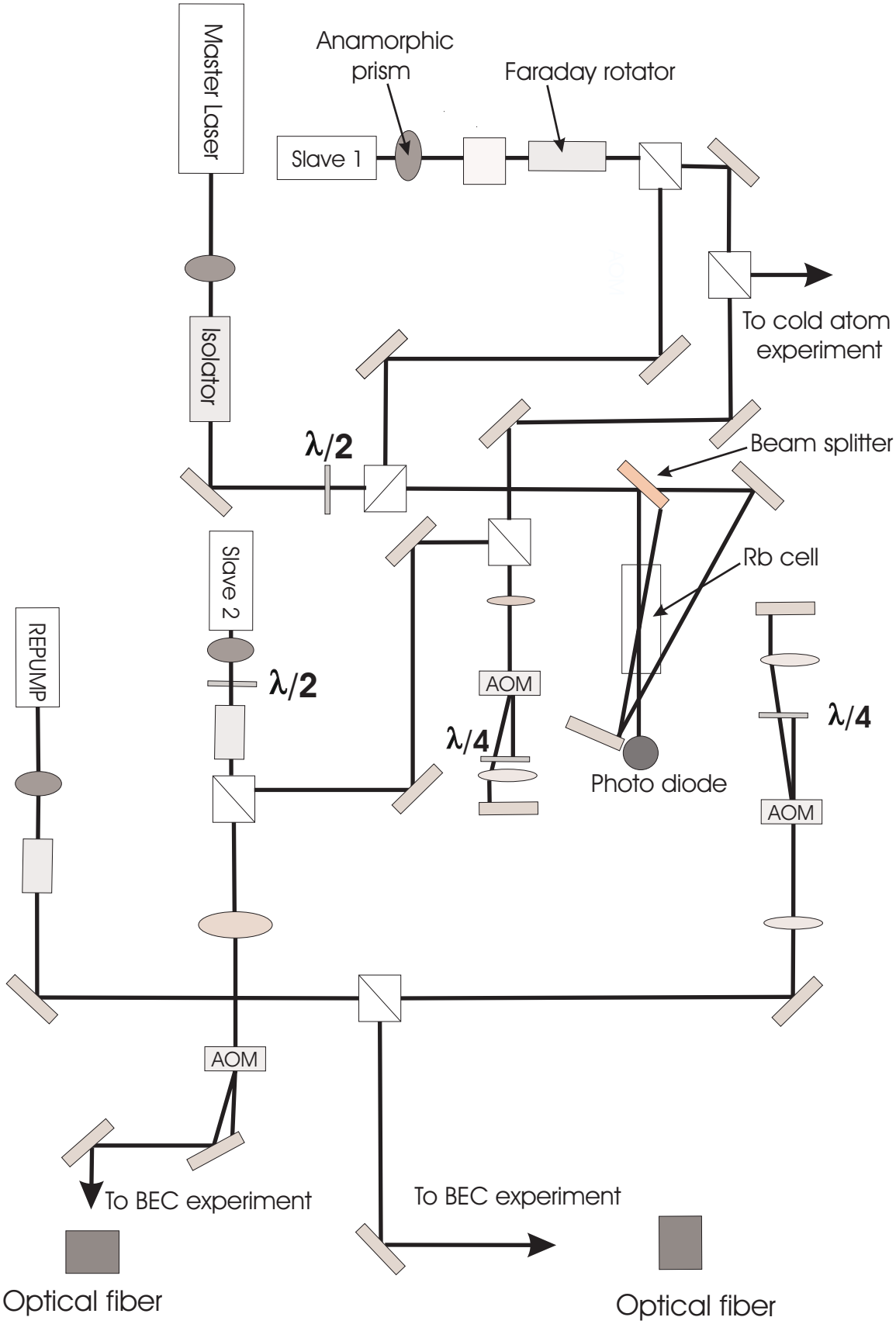

Figure 4.15. The optical table setup.

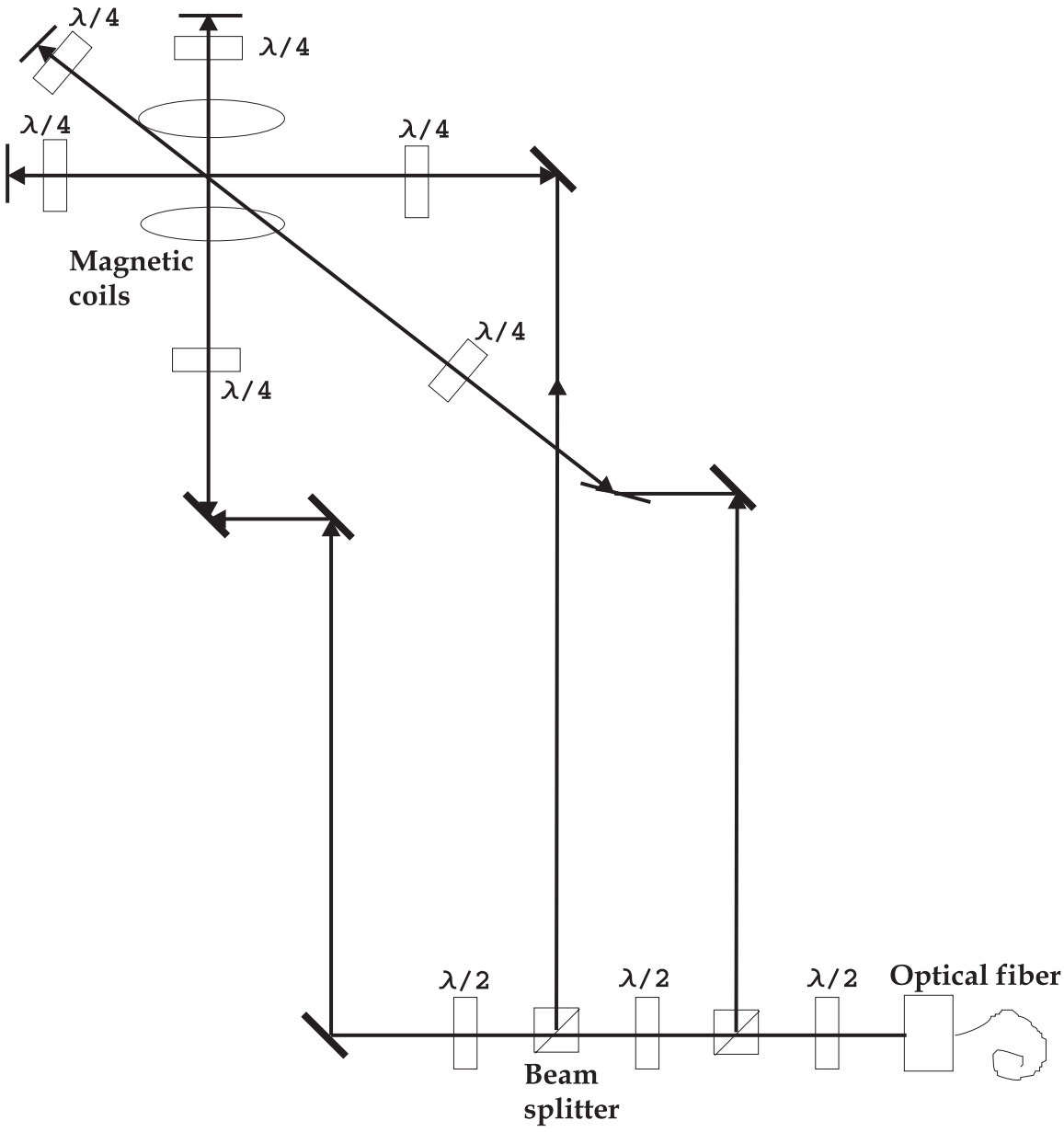

Figure 4.16. Schematic of the experimental setup for trapping and cooling atoms.

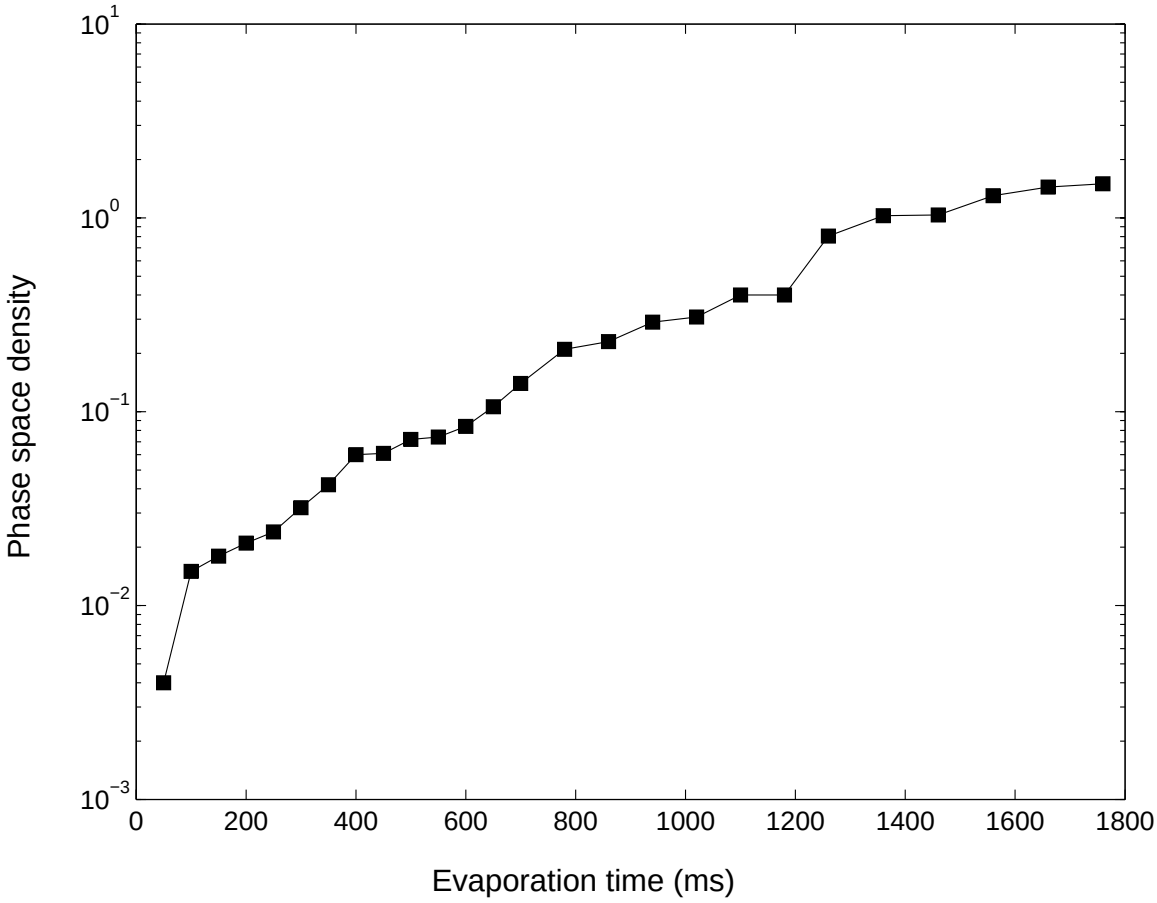

Figure 4.17. Observed phase space density versus evaporation time. Note that the FORT phase space is in log scale.

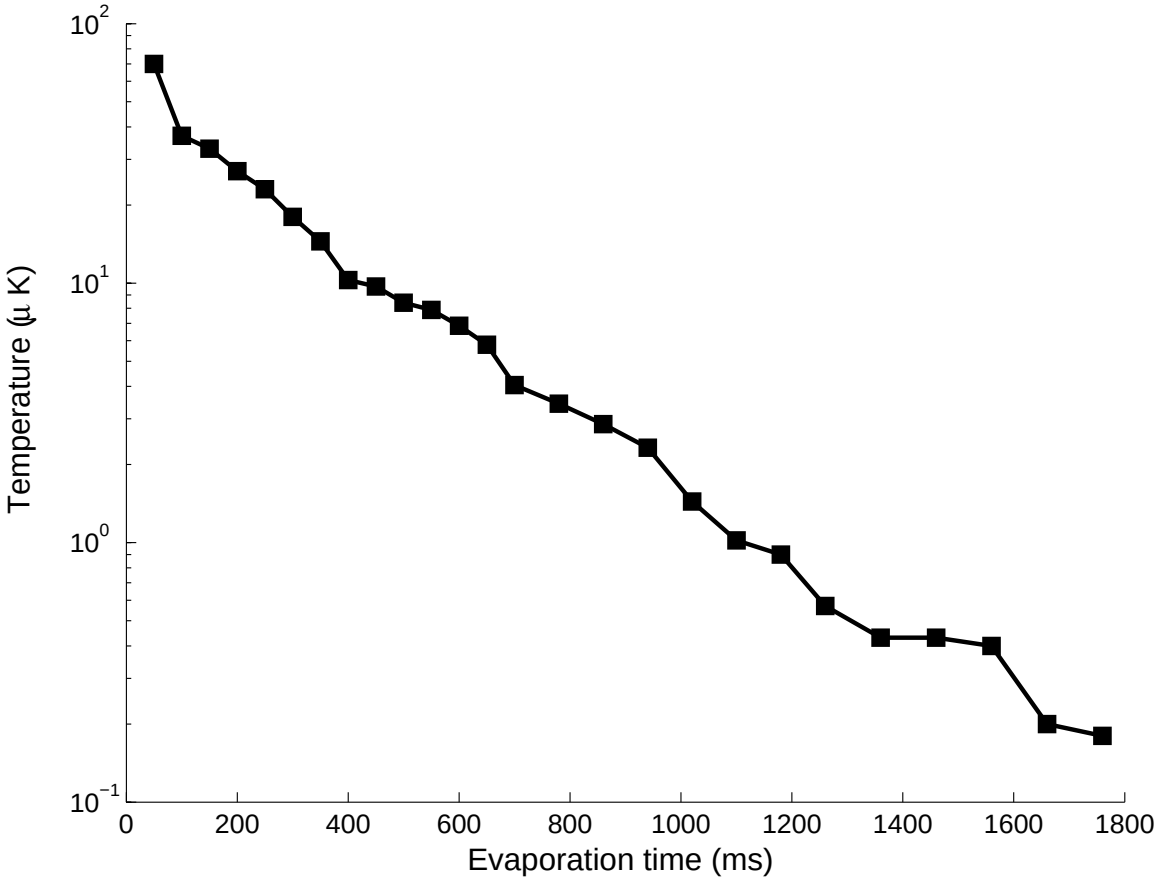

Figure 4.18. Observed temperature of the remaining cloud in the FORT versus evaporation time. The temperature was calculated using the expansion rate of the cloud for a 10 ms time of flight data. Note that the FORT temperature is in log scale.

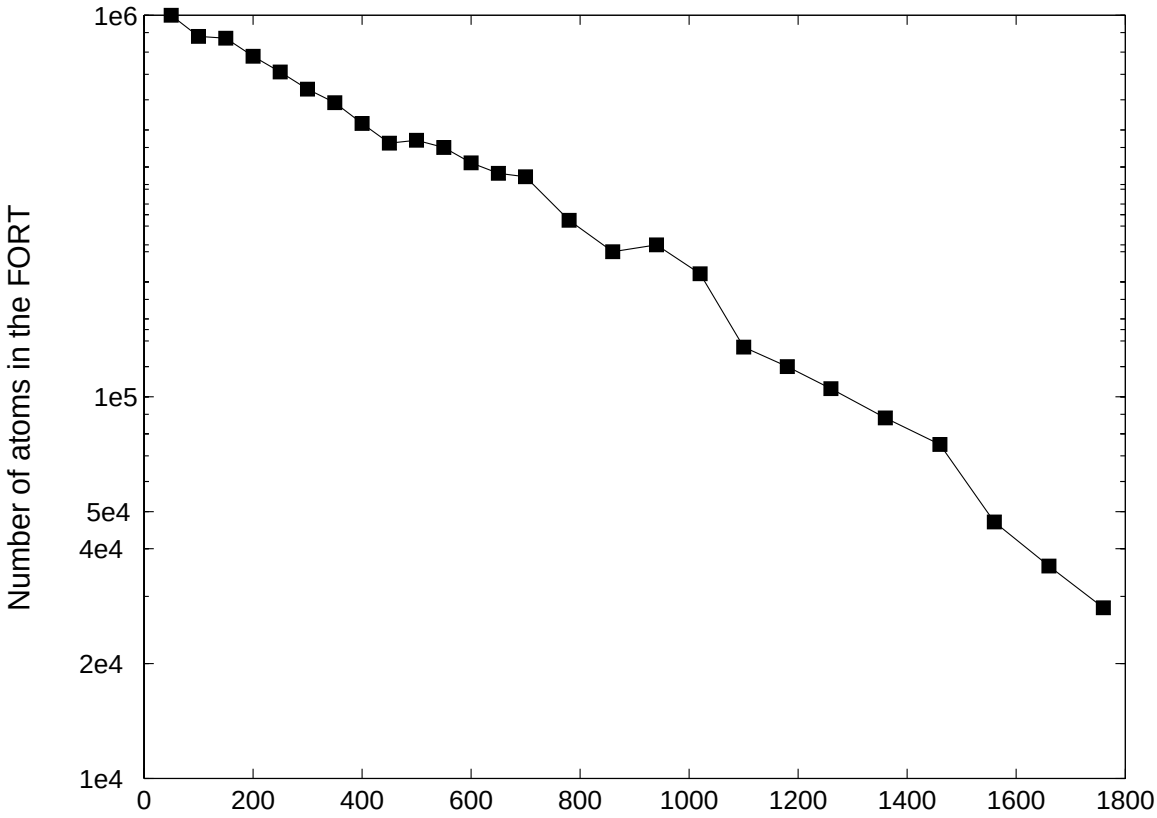

Figure 4.19. Observed FORT population versus evaporation time. Note that the FORT population is in log scale.

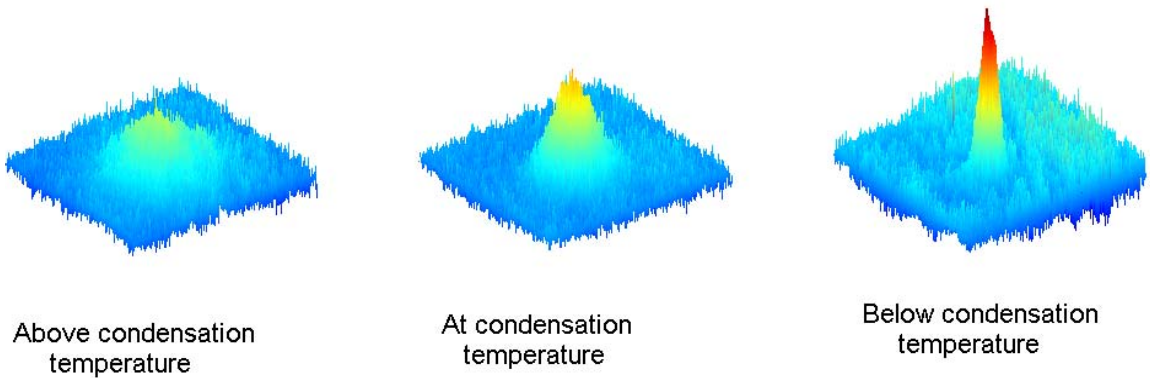

Figure 4.20. Atomic cloud after 6 ms expansion above, at, and below the condensation transition. The FORT had 2×10^6 atoms after loading from MOT with a 70 μK temperature. At the end of evaporative cooling the BEC had 10×10^3 atoms.

CHAPTER 5

GEOMETRICAL EFFECTS IN THE LOADING OF AN OPTICAL ATOM TRAP

The trapping of atoms using light that is far-detuned to the red of an atomic resonance has been the subject of study for almost a decade now [81,82]. Recently a resurgence of interest in these far off-resonant optical traps (FORTs) has led to the all-optical production of BECs of rubidium [31], cesium [32] and ytterbium [83]. A FORT has been used to produce a degenerate Fermi gas of lithium [84] and has even formed the basis for the first all-optical atom laser [85]. These optical traps offer several advantages over the traditional magnetic traps that are used to produce BEC; the trapping is not limited to a particular Zeeman sub-state, and the geometry of the trap can be readily adjusted. Furthermore, the tight confinement that is possible in a FORT produces high initial elastic collision rates leading to the possibility of rapid evaporative cooling. However, the efficient loading of a FORT with atoms still remains a challenge.

Typically in rubidium FORT experiments, a far off-resonant laser beam from a CO_2 laser is focused into a collection of atoms that accumulate in a MOT. Although there has been previous work on the mechanisms important in the loading of a FORT [86], there are still many aspects of this process that are not well understood. In particular the role of the FORT geometry has received scant attention. As we will see, the FORT volume plays a critical role in determining the number of atoms loaded. However, increasing this volume can lead to reductions in the density and consequently a less useful trap for evaporative cooling. We suggest a way around this problem using a time-averaged potential [87,88].

In this chapter we begin by examining the background to trapping atoms by far off-resonant laser light, giving a simple theory which allows us to understand the key parameters affecting the loading efficiency of the FORT from a MOT. We proceed to present a detailed experimental study of the loading process, looking at the effect of the FORT depth and spatial extent in section 5.3. In section 5.4 the concept of time-averaged potentials is introduced and we report the results of our experiments.

5.1 Theoretical model

In our experiment, rubidium atoms in a MOT are exposed to a focused CO_2 laser beam. Since the wavelength of this light (10.6 μm) is far to the red of the rubidium D2 transition (780 nm), the interaction of the atoms with the laser light is quasi-electrostatic. This produces an energy shift of the atomic ground state given by Eq. (3.27), $U = -\frac{1}{2}\alpha_g |E|^2$, where α_g is the ground state static polarizability and $|E|^2$ is the time average of the square of the laser light's electric field. For a Gaussian laser beam propagating in the z direction this quantity can be expressed as Eq. (3.29),

$$|E(x,y,z)|^2 = E_0^2 \frac{w_0^2}{w^2(z)} \exp\left(\frac{-2(x^2+y^2)}{w^2(z)}\right) \tag{5.1}$$

where $w(z) = w_0 \left(1 + (\frac{z}{z_R})^2\right)^{\frac{1}{2}}$. Here w_0 is the beam waist, z_R is the Rayleigh length, and E_0 is the electric field amplitude. The atoms experience a potential minimum at the focus of the laser beam and can become trapped. Unfortunately, the capture range and depth of such a trap is rather limited, so it is necessary to load the optical trap from a MOT. Clearly the efficiency of such a process is of great interest since it is highly desirable that the FORT contain as many atoms as possible. This loading process has been theoretically investigated from several different perspectives. For example, O'Hara and co-workers solved a Fokker-Planck equation (see [86] and references therein), while Kuppens *et al.* [77] used a phenomenological approach to investigate the process. In the present work we build on the simple model introduced in [89] rather than engaging in a full 3D dynamical treatment of the problem. As will be seen,

this straightforward approach helps us to understand the effect of the geometrical configuration on the FORT population.

We assume that the atomic cloud of the MOT has a Maxwell-Boltzman distribution and that the atoms in the dipole trap eventually come into thermal equilibrium with the MOT [23,89]. Therefore the FORT population is given by,

$$N = \int n\, f(\mathbf{r}, \mathbf{p})\, d\mathbf{r}\, d\mathbf{p}\, g(\epsilon) \tag{5.2}$$

where n is the particle density and $f(\mathbf{r}, \mathbf{p})$ is the distribution function for the atoms with $\mathbf{r}$ and $\mathbf{p}$ their spatial and momentum vectors. In Eq. (5.2) the ratio of the density of states for the gaussian potential created by the CO_2 laser, to the density of states of the MOT potential is represented by $g(\epsilon)$, where ϵ is the energy. Atoms with energy less than the maximum potential U_0 can be trapped in the FORT and therefore the integration is truncated over all $(\mathbf{r}, \mathbf{p})$, for which,

$$U(\mathbf{r}) + \frac{|\mathbf{p}|^2}{2m} > U_0 \tag{5.3}$$

where m is the mass of an atom. Hence the integration boundaries of $\mathbf{r}$ and $\mathbf{p}$ are coupled together through Eq. (5.3) and the evaluation of N involves a complicated integration. Perhaps the most critical parameter in this equation is $g(\epsilon)$ which varies between zero (for a δ-function like potential) and one (for a very shallow FORT potential). To study Eq. (5.2) we assume that in the overlap region between the MOT and the FORT the particle density is constant and is equal to the MOT peak density. To further simplify the equations we also treat $g(\epsilon)$ as a constant, g_0, over the overlap region. These assumptions transform Eq. (5.2) into,

$$\begin{aligned} N &= n_0 V_0 \frac{4 g_0}{\sqrt{\pi}} \int_0^{\sqrt{q}} u^2 \exp(-u^2) du \\ &= n_0 V_0 g_0 \left(\frac{4}{\sqrt{\pi}} Erf(\sqrt{q}) - \frac{8}{\pi} \sqrt{q} e^{-q} \right) \end{aligned} \tag{5.4}$$

where $u = |\mathbf{p}|/\sqrt{k_B T}$, $q = U_0/k_B T$. In Eq. (5.4) n_0 and V_0 are the MOT peak density and the overlap volume between the MOT and the FORT respectively. Therefore

$n_0 V_0$ is the total number of atoms in the overlap region and the remainder of the parameters define the loading efficiency. The integral in Eq. (5.4) saturates when q approaches infinity which corresponds to an infinite well depth. In fact, evaluation of this integral shows that for $q > 4$ the FORT population is approximately independent of the value of q. Therefore we introduce the concept of a saturation power, beyond which any increase in the CO_2 laser power does not appreciably affect the FORT population. For a MOT containing Rb^{87} atoms with a typical temperature of 0.2 mK, the saturation power for a CO_2 laser beam focused to a 35 μm waist is expected to be about 25 Watts. To achieve a higher FORT population, increasing the overlap volume V_0 would seem to be a sensible step. However, larger V_0 leads to a shallower potential well which can reduce the intensity and hence the loading efficiency. This should not present a problem provided that the intensity in the trap remains greater than the saturation level. In what follows we will present the results from experiments in which we varied this volume in two different ways.

5.2 Experiment

5.2.1 Experimental setup

We used the same vacuum chamber that was described in chapter 4 to perform this experiment. The horizontal 2.5 cm diameter ZnSe viewports are used to transmit the 10.6 μm light from the CO_2 laser into the chamber. The focusing arrangement for the CO_2 beam consisted of a beam expander followed by a 3.75 cm focal length lens which was placed within the vacuum. As shown in Fig. 5.1(b), the FORT beam was directed into the chamber horizontally. This light originated from a 50 Watt RF excited CO_2 laser. The total laser power is controlled by passing the output light through an AOM. This reduces the laser power to roughly 36 Watts. The first order of the AOM was then directed to the vacuum chamber. We used the same procedure as explained in the conclusion of Chapter 4 to load the FORT. Then both the MOT

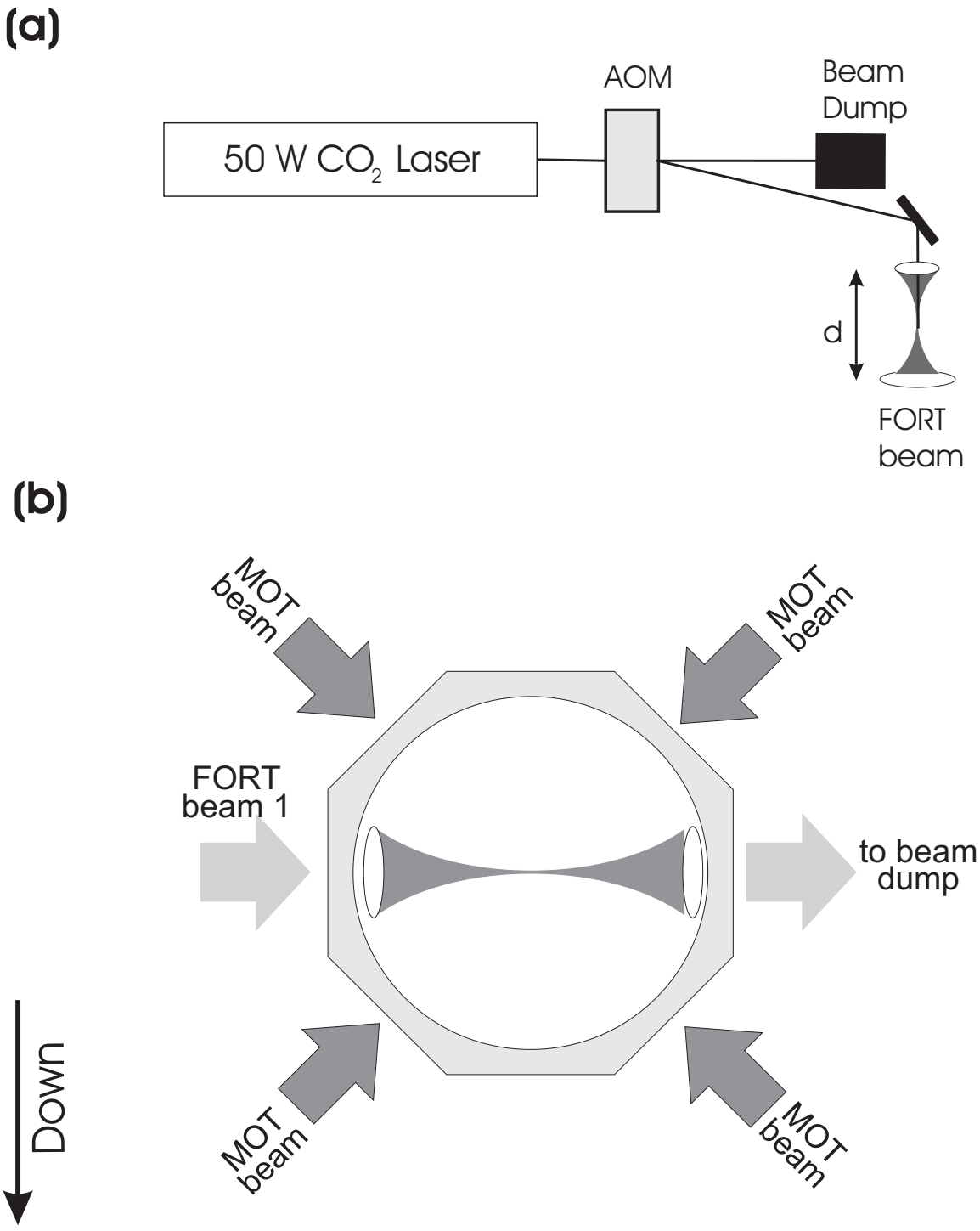

Figure 5.1. Experimental schematic. The optical arrangement used to create the CO_2 FORT beam is depicted in (a). In (b) the geometry of the FORT and MOT beams with respect to the vacuum chamber is illustrated. Additional MOT beams which propagate into and out of the plane of the paper are not shown.

and the FORT were destructively imaged using a resonant probe laser which passed through the atom cloud and was incident on a CCD camera. The number of trapped atoms was determined by integrating the optical density across the atom cloud. When imaging the FORT, the CO_2 laser beam was switched off at least 1 ms before the image was taken to allow the cloud of atoms to expand to a size which was above the resolution of the optical system.

5.2.2 Saturation power

We investigated the sensitivity of the FORT's loading efficiency to the total power in the optical trap. We began by focusing the CO_2 laser beam into a $35 \pm 5\,\mu$m waist which coincided with the MOT center. Several experiments were performed in which the FORT was loaded using different CO_2 powers. The results of these experiments are shown in Fig. 5.2. These data clearly show that the number of atoms trapped in the FORT increases slowly as the power becomes larger until about the 20 Watt level. Above this power very little change in the number of atoms can be seen, since U_0 is much larger than the mean energy of the atomic cloud.

An additional point is that the differential ac Stark shift between ground and excited states effects the efficiency of loading into dipole traps. This effect has been reported by Scheunemann[79] *et al.* as an improved loading efficiency in the wings of the optical trap compared to its center. However, for the parameters of present work (beam waist of 15 to 30 μm and power 36 Watts) the frequency shift induced by the differential ac Stark effect is between -62 to -15 MHz. Since the cooling frequency is detuned by -80 MHz from $F = 2 - F' = 3$ transition, the MOT light always remains red detuned for the atoms. Therefore, one would conclude that at even higher CO_2 laser power one would expect a decrease in FORT population.

Considering the growing interest in optical trapping and making BEC using all optical methods, it is useful to note that if one is developing a cost effective setup for an experiment that will be used for evaporative cooling (and consequently needs

a beam waist of around 30 μm), it is unnecessary to invest in a laser with a power of more than about 50 Watts (25 Watts per beam).

5.2.3 Effect of the FORT volume on the FORT population

In Section 5.2 we theoretically considered the effect of the overlap volume on the FORT population. To experimentally observe this dependency we performed an experiment in which the number of atoms in the FORT was measured as a function of the beam waist of the laser beam. This was achieved by passing the CO_2 laser beam through a beam expander before the vacuum chamber. The beam expander consisted of two lenses with 6.35 and 12.7 cm focal lengths whose separation could be varied by mounting the second lens on a translation stage. The ABCD matrix method [90] was used to calculate the beam waist corresponding to a specific separation of the lenses. To perform the experiment the lens separation was initially set to a minimum and the FORT was loaded. The remaining data points were obtained by regular increments of the second lens position. The experimental results are presented in Fig. 5.3. It is clear from these data that there is a significant reduction in the number of atoms trapped in the FORT for smaller beam waists. Note that the FORT population should in principle increase with w^3. However, this is likely not observed (see section 5.4) because the saturation power also increases with w. For example, the saturation power is about 71 Watts at a 70 μm beam waist.

5.3 The time-averaged-optical trap

The Theory of section 5.2 and the experimental results of Section 5.3 both emphasize the sensitivity of the optical trap's population to its volume. In the following section we introduce a dynamical technique to increase this volume. This method is based on sweeping the FORT beam back and forth while it is overlapped with the MOT. Provided the motion of the beam is rapid enough, such an oscillatory motion creates a time-averaged potential with a large volume. This can capture atoms which

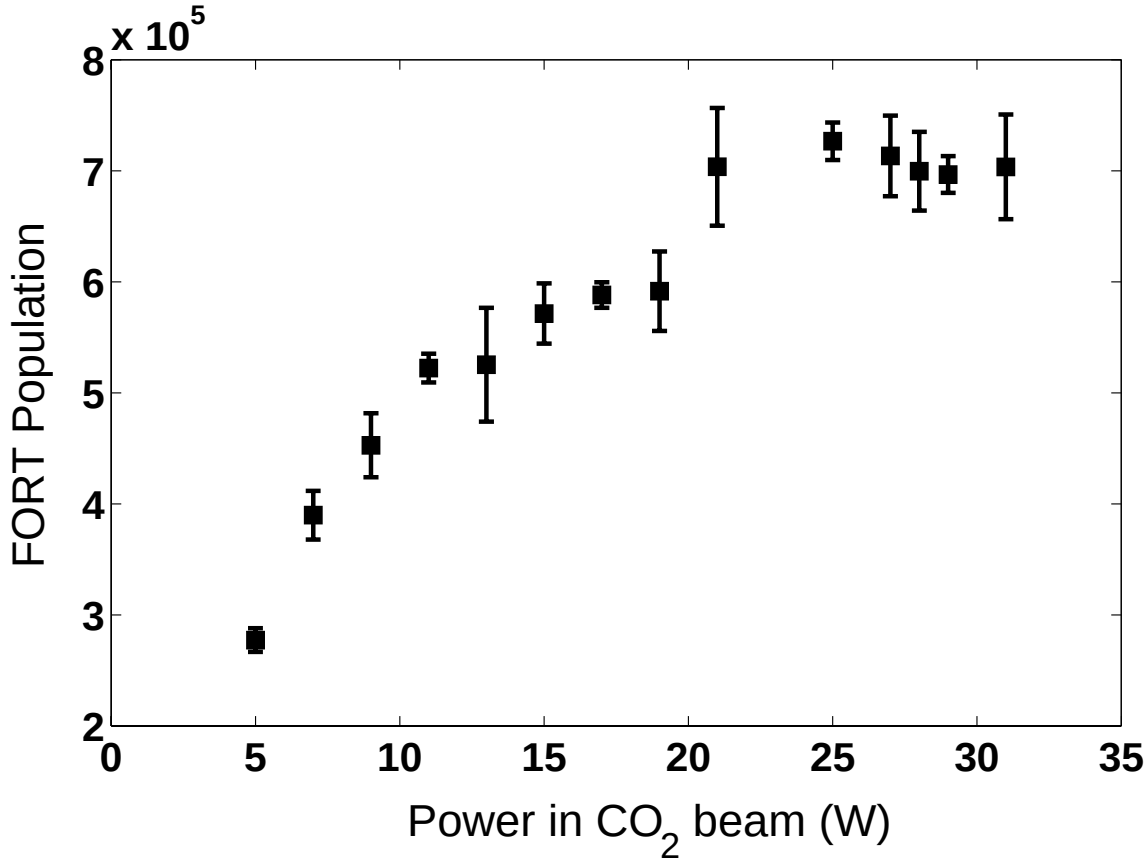

Figure 5.2. Experimental data showing the number of atoms contained in the FORT vs. power in the CO_2 beam. The power is focused to a $35 \pm 5\,\mu$m waist. The MOT population was $\approx 2 \times 10^7$

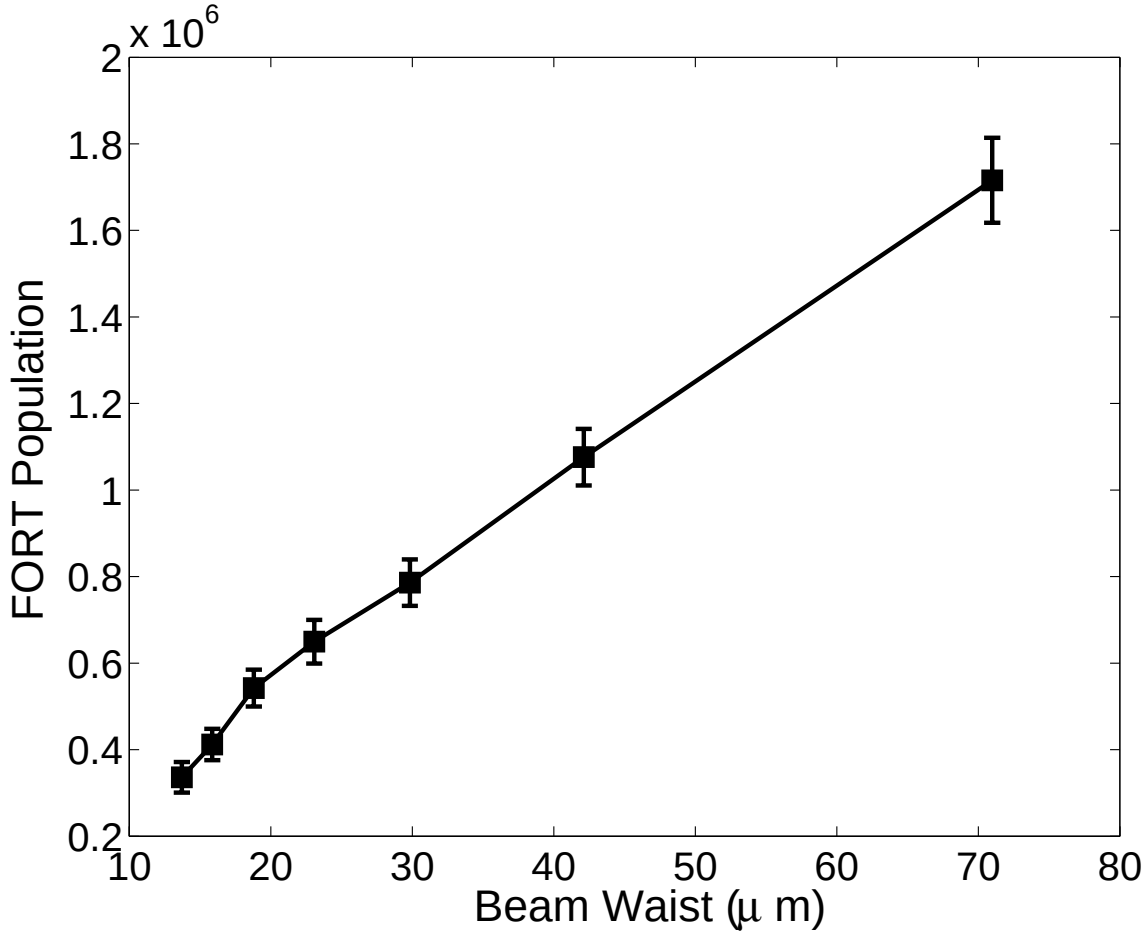

Figure 5.3. Experimental data showing the number of atoms vs. beam waist. The total power in CO_2 beam was 36 Watts.

are out of reach of a static FORT. Hence, these oscillations are expected to produce a significant increase in the number of atoms that can be loaded.

In order to create a time-averaged potential we used the fact that the angular position of the first order AOM beam is proportional to the RF frequency supplied to the AOM. Therefore a frequency change, $\Delta\nu$, from the original 40 MHz will produce an angular deviation of the beam given by $\Delta\theta = \lambda\Delta\nu/v_a$, where λ is the wavelength of the light and v_a is the velocity of the acoustic wave in the AOM. The 40 MHz signal from the function generator was modulated with a triangle function which changed the frequency with a period T and amplitude $\Delta\nu$. Such a technique may be important in situations where a large volume trap is loaded with many atoms and then adiabatically transformed to a tighter geometry for efficient evaporative cooling. It is worthy of note that even though this procedure increases the time-averaged size of the CO_2 beam on the final lens, the size of the beam focus also increases. This is the opposite to what would be expected for a real increase in beam size on the final lens. In the following subsections we study the properties of the time-averaged optical traps.

5.3.1 Repump light intensity

A well established part of the procedure for loading an optical trap is the strong reduction in the repump power a few milliseconds before turning the MOT beams off[77]. The reduction in the power of the repump laser, together with the energy shift induced by the electric field of the CO_2 laser, means that atoms trapped in the FORT have a significantly reduced probability of being kicked out of the FORT by the primary MOT light. We performed a series of measurements in order to study the correlation between the trap loading and repump light power for different FORT potentials. Figure 5.4 represents the experimental results for two different traps. Data points with a square symbol represent observations for no frequency sweep, open circles are for time-averaged traps with $\Delta\nu = 2$ MHz. As expected, the population of

the time-averaged potentials has a similar correlation with repump light power as a static FORT, where the population maximum is reached at a specific repump power and then falls to some saturated level for higher powers. The maximum loading of the time-averaged potentials also occurs at the same repump power as for the stationary FORT. This behavior was observed for all of the other sweeping frequencies which were examined.

5.3.2 Sweeping period

We also studied the effect of the sweeping period on the number of atoms in the FORT, N. The experiment was carried out by changing the period, T, of the triangle modulation function applied to the AOM by the function generator. The data in Fig. 5.5 shows N for three different $\Delta\nu$'s taken at different sweeping periods. This figure shows that the sweeping period at which N saturates depends strongly on the sweeping frequency. Furthermore, the FORT population rapidly falls for long sweeping period. These results indicate that the shoulder of the N curves (the edge of the saturation region) is inversely proportional to $\Delta\nu$. Such behavior can be explained by noting that the longer the period and the smaller $\Delta\nu$ becomes, the more the atoms are placed in a regime where they can adiabatically follow the motion of the laser beam. This effectively negates the time averaging effect and prevents a larger volume FORT being realized.

5.3.3 Sweeping amplitude

The number of atoms trapped in the FORT for different $\Delta\nu$ is given in Fig. 5.6. All data were taken with a sweeping period of $T = 30\,\mu$s. Since we ultimately wish to use this procedure to capture as many atoms as possible in order to do evaporative cooling, we switched to an experiment with a much smaller CO_2 beam waist. The beam waist was $20 \pm 5\mu$m and the CO_2 beam had 20 Watts power. Figure 5.6 shows that the FORT population reaches a maximum at $\Delta\nu = 1$ MHz with approximately a

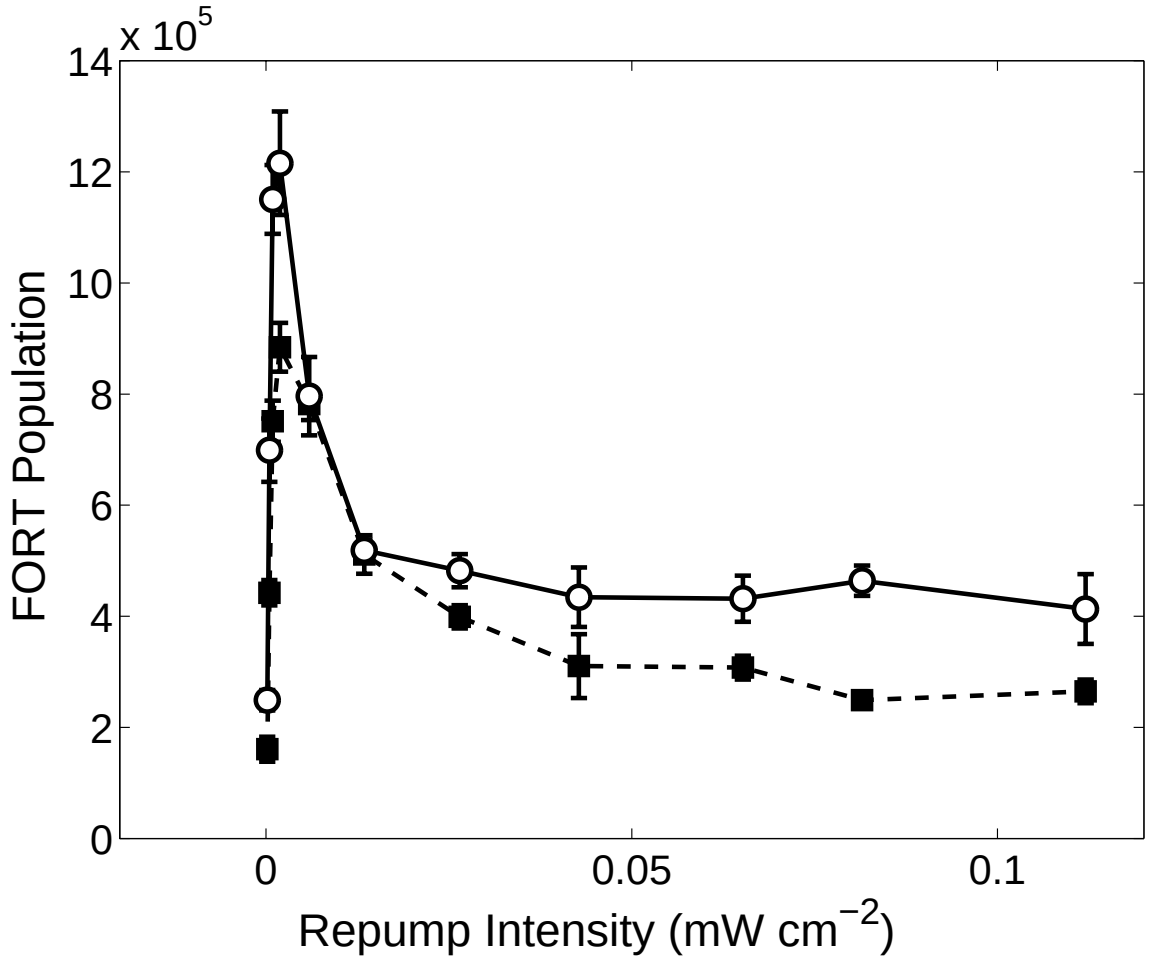

Figure 5.4. Experimental data showing the number of atoms trapped in the FORT versus the intensity of the repump light during the FORT loading. The beam waist was $35 \pm 5\mu$m and power in the FORT beam was 36 Watts. The initial repump intensity used to make the MOT was 0.16 mW/cm^2. The square and open circle symbols represent the data for $\Delta\nu = 0$ and 2 MHz respectively. The procedure for loading FORT was same as discussed in subsection 5.3.1

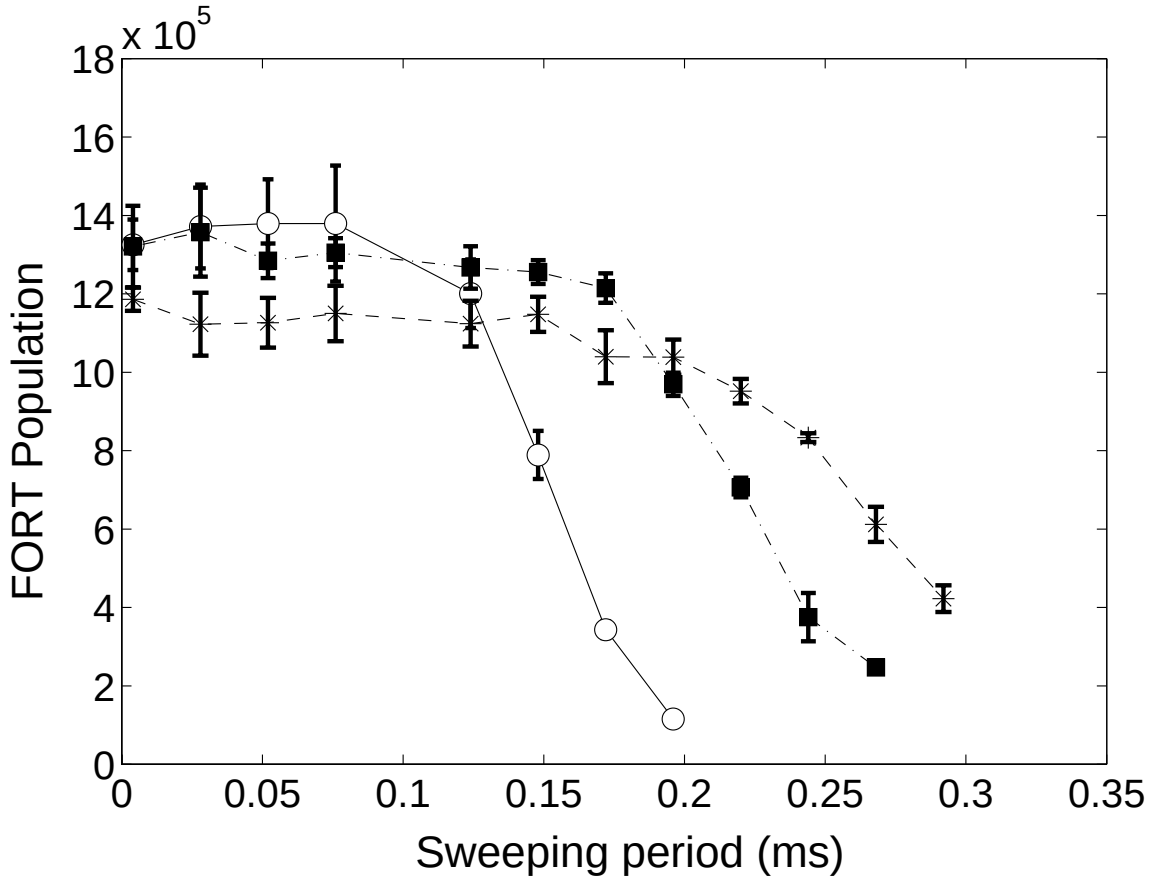

Figure 5.5. Experimental data showing the number of atoms vs. sweeping period. The beam waist was $35 \pm 5\mu$m and power in the FORT beam was 36 Watts. The open circle, square, and star symbols represent the data for $\Delta\nu = 1$, 2 and 3 MHz respectively.

100% improvement in the population compared to the stationary FORT. For sweeping frequencies more than $\Delta\nu = 3$ MHz, the number of atoms falls even below the static trap ($\Delta\nu = 0$ MHz) population. We believe this decrease is a result of the reduction of the average well depth below the saturation level, which is inversely proportional to the sweeping amplitude. Consequently only very cold atoms should stay in the trap. This has been confirmed by the experiment that will be discussed in the next subsection.

The next step after loading the time-averaged-trap was to transfer the atoms into a tight FORT for efficient evaporative cooling. This was achieved by linearly damping the sweeping amplitude over 6 ms after switching off the MOT beams. The FORT population at the end of the damping is shown by filled circles in Fig. 5.6. The data indicate that almost none of the atoms are lost from the FORT during the damping process. Effectively this damping is a realization of an acousto-optically controlled 1D zoom lens for the optical trap. We note that recently Kinoshita *e*t al. have achieved an all optical BEC using a mechanical 2D zoom lens [33].

5.3.4 Trap temperature

The ballistic expansion rate of the atomic cloud was used to deduce its thermal temperature. The experiment was carried out by abruptly turning off the FORT beam. The expanding cloud was destructively imaged after several different expansion times for each of several different sweeping amplitudes. The corresponding data are shown in Fig. 5.7 for radial expansion rate. These figures show that the cloud trapped by time averaged potentials with a bigger $\Delta\nu$ had a slower expansion rate and consequently a lower temperature.

These temperatures are given by the open circles in Fig. 5.8 and indicate that the time-averaged traps confine colder samples of atoms. In another series of experiments the cloud temperature was measured after damping the sweeping amplitude to zero. The final temperature for each $\Delta\nu$ is shown by square symbols in Fig. 5.8.

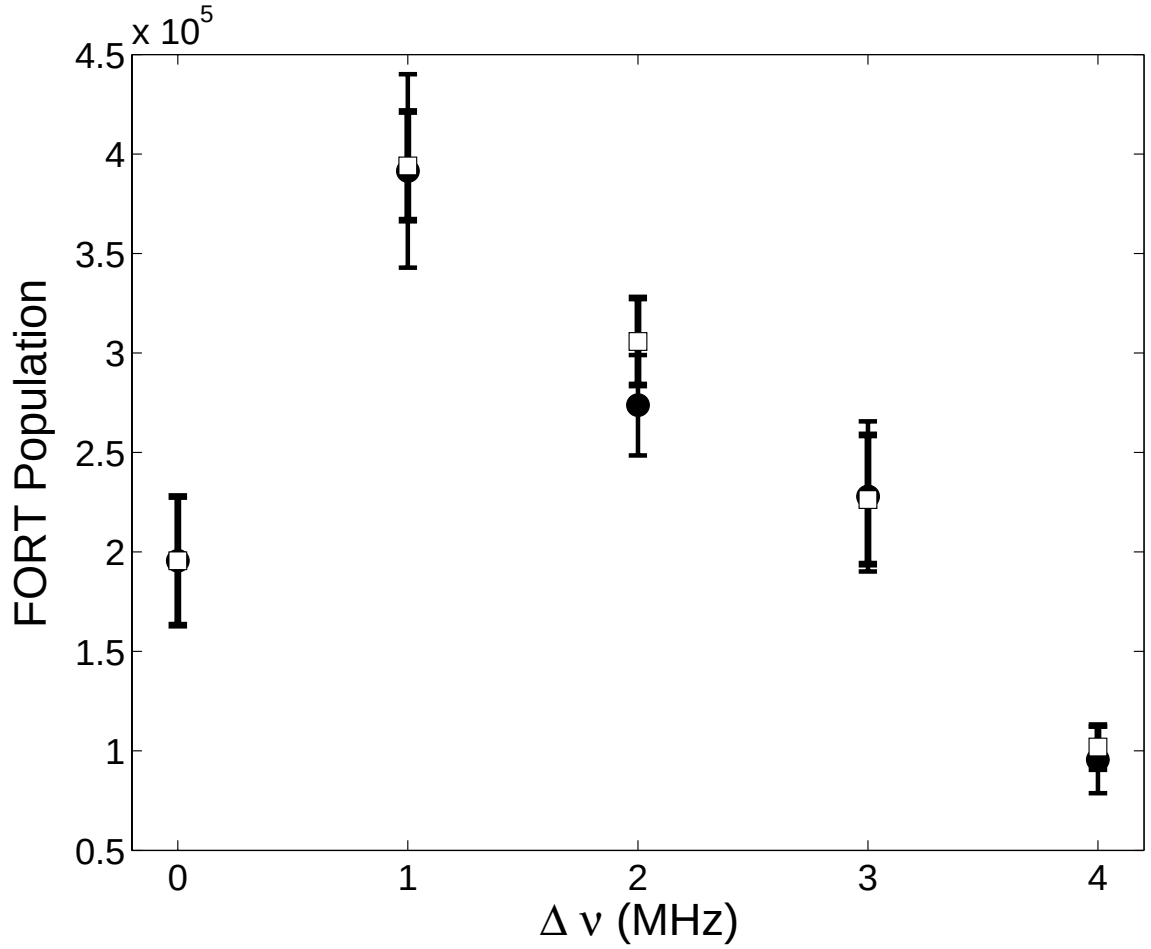

Figure 5.6. Experimental data showing the number of atoms vs. $\Delta\nu$. The beam waist was $20 \pm 5\mu$m and power in the FORT beam was 20 Watts. The square and circle symbols are the FORT population before and after damping respectively. Note that at several $\delta\nu$ the two data sets overlap.

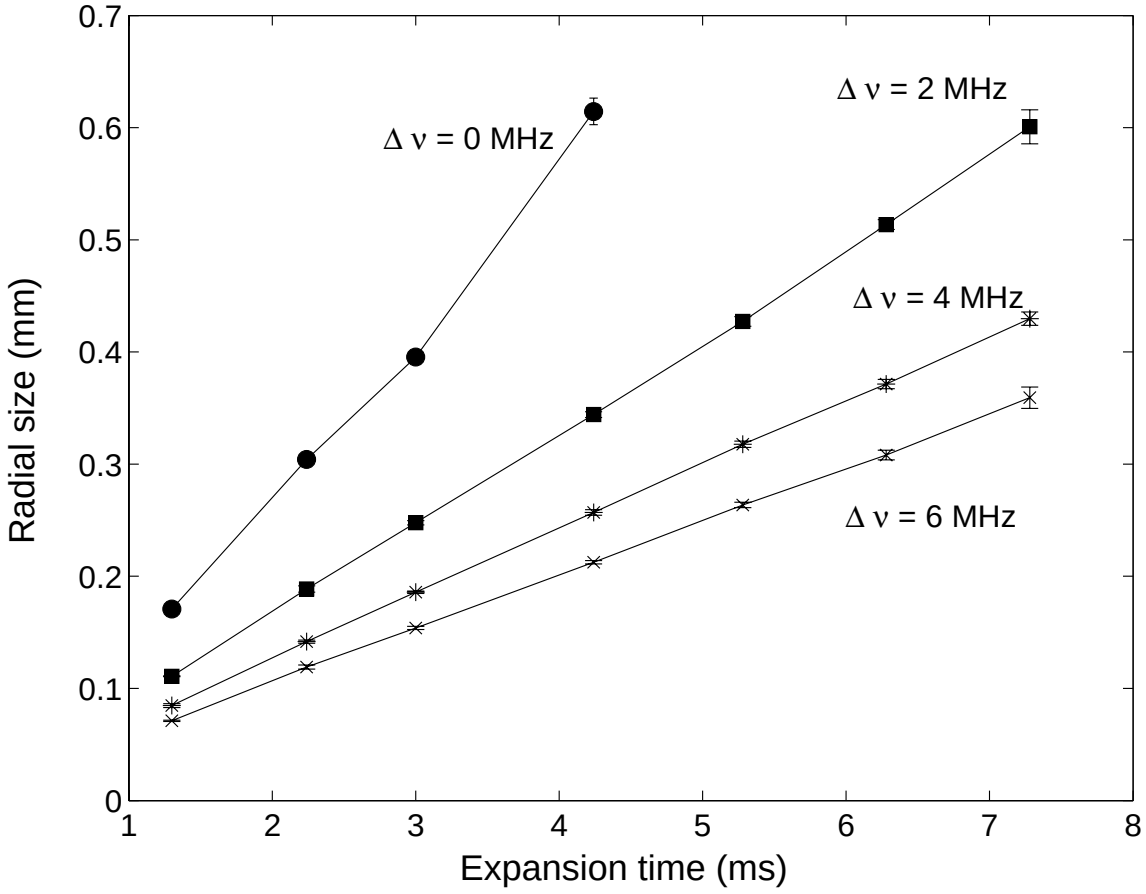

Figure 5.7. Experimental data showing the radial size of the expanding cloud as a function of expansion time for various sweeping frequency.

The data shows a rise in the cloud's temperature after damping. However, the final temperature is still lower than the temperature of atoms loaded into a static FORT. This behavior can be explained by noting that the trap well depth is inversely proportional to the sweeping amplitude squared for time averaged potentials, so that the time averaged traps' well depth is smaller than the stationary beam. According to the theoretical discussion of Section 5.2 this restricts the time-averaged FORT to capturing atoms with lower energy in the overlapped volume. Consequently the time averaged potentials in our experiments collected a colder sample of atoms. Furthermore, while damping the sweeping amplitude the well depth increases. Since the potential is attractive the extra negative potential energy will be converted to kinetic energy of the atoms which was observed as an increase in the expansion rate of the cloud.

Comparing the results of Fig. 5.6 and Fig. 5.8 we conclude that the phase space density after damping the sweeping should increase at least in proportion to the number of atoms gained over the static beam case. This increase can be critically important for reaching the BEC transition.

5.4 Conclusion

In this chapter we have shown that the volume of an optical dipole-force trap is one of the most important factors in determining the number of atoms loaded into such a trap. To increase this volume a time-averaged optical trap was realized. Our observations show that the time-averaged traps can not only capture more atoms compared to their static counterparts, but that the atomic clouds trapped within them have a considerably lower temperature. By slowly damping the sweeping amplitude almost all of the atoms were transported to a static trap. Although damping raised the cloud temperature, interestingly, it was always lower than the temperature of the cloud loaded directly into a static trap. Therefore, the ratio of the phase space densities of a damped time-averaged potential and a static trap was increased by

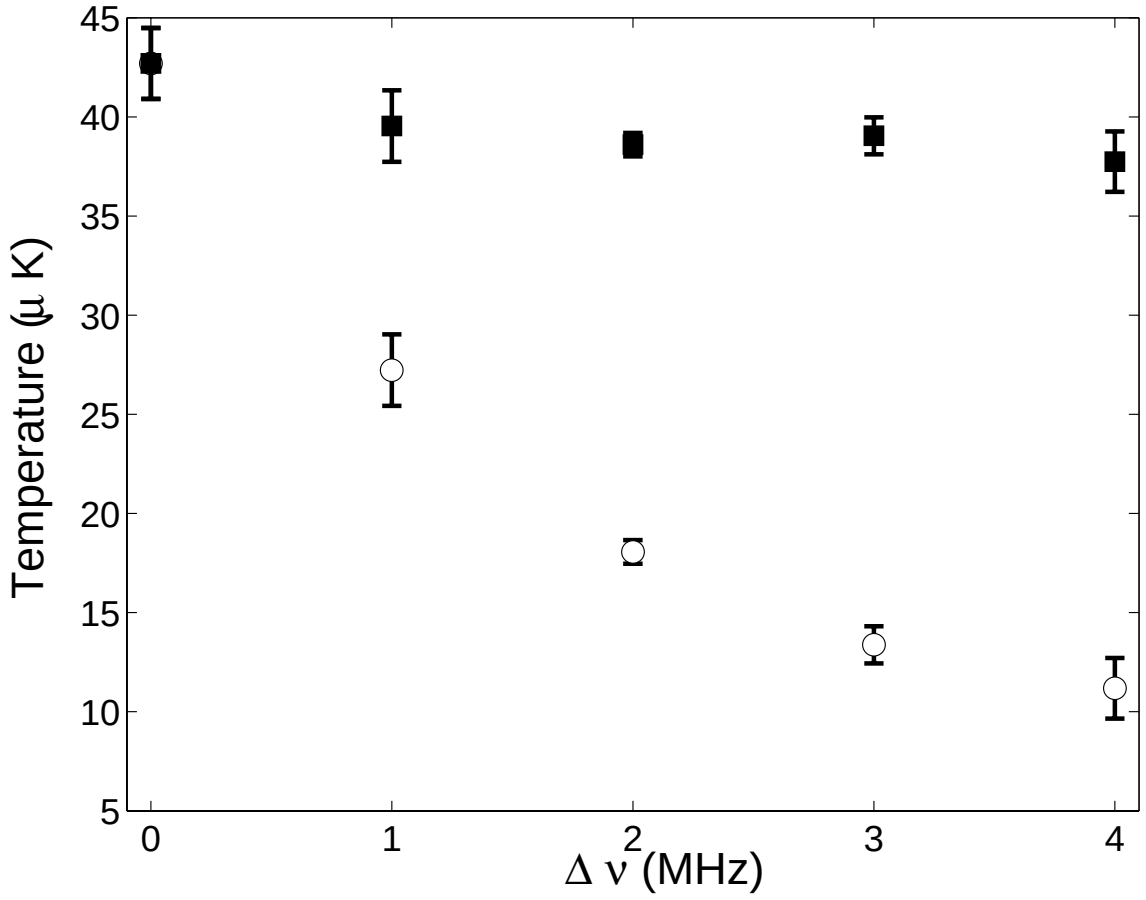

Figure 5.8. Temperature of the atomic cloud vs. frequency sweep. The open circle and square symbols are the cloud temperature before and after damping the sweeping amplitude.

a factor given approximately by the ratio of the trap populations. We have also experimentally confirmed that above a certain laser power (which will depend upon the volume of the trap) there is very little increase in the number of atoms that can be loaded in a FORT. One possible avenue for future investigation is the realization of a crossed beam time-averaged trap. This would allow for the loading of atoms using even larger volume FORTs while still maintaining a tight trap for efficient evaporation. This may be important for creating Bose-Einstein condensates using rapid evaporation from a highly focused, near-resonant laser trap.

CHAPTER 6

MULTIPLE MICRO-OPTICAL ATOM TRAPS WITH A SPHERICALLY ABERRATED LASER BEAM

Quantum information research is another interesting avenue for potential application of optical traps. For example the proposal of Brennen*et al.* [91] for quantum logic gates using neutral atoms in optical lattices, provided a way around the decoherence problem which affects schemes involving charged particles. They showed that entanglement between a collection of trapped neutral atoms can be created with a laser using the induced electric dipole-dipole interaction. The main difficulty associated with their scheme has been the need to construct a lattice FORT with sufficient separation between unit cells to address them individually and with a sufficient volume to load many atoms at each trapping site. These challenges have been the focus of another series of experimental efforts. For example, using a holographic phase plate, Boiron *et al.*[92,93] constructed an optical lattice with a period of 29 μm using a YAG laser. In other experiments, the Hannover group have developed a technique using arrays of microlenses to focus a red detuned laser beam and create a series of micro-traps for use as quantum memories [94–96]. Peil *et al.*[97] employed two independent optical lattices, whose spatial periods differ by a factor of three, to load a Bose-Einstein condensate of Rb87 atoms in sites having a separation of approximately 30 μm.

In most FORT experiments atoms are trapped at the intensity maxima formed by a focused laser beam in either a travelling or standing wave configuration. In this chapter, we demonstrate a new approach in which the peaks in the diffraction

pattern associated with spherical aberration in the vicinity of the focal plane of a lens are used to create a linear array of micro-traps. The primary spherical aberration pattern has been studied and well documented by several authors. For example, Evans and Morgan [98,99] theoretically produced the aberration pattern of a lens that was not corrected for spherical aberration in order to explain laser induced breakdown in gases, while Smith [100] experimentally verified the primary spherical aberration intensity distribution produced by a lens uncorrected for spherical aberration. The spherical aberration in our experiments is induced by the lenses in the path of a CO_2 laser beam. It will be seen that most of the contribution to the spherical aberration comes from the final lens (primary lens) which is employed to focus the CO_2 laser beam onto the atomic cloud. Varying the incident beam size on the primary lens enabled us to change the aberration pattern and hence control the separation of the micro-traps over a range of about a millimeter. One of the advantages of our set up is the use of a CO_2 laser as a far off-resonant light source. This considerably improves the coherence time compared to some of the atom optical experiments mentioned above which use YAG lasers to create dipole traps with micron size separation. Furthermore, the ability to vary the spacing between the micro-traps over a range of about a millimeter makes the addressing of the individual traps feasible using the techniques developed by Nägerl *et al.*[101].

This chapter is constructed as follows. In Section 6.2 we discuss the theory of the multiple trap potential that is used in simulations. Section 6.3 is devoted to the description of the experimental setup. In Section 6.4 we present the experimental data and compare them with our simulation results. Our suggestions and future plans for the use of these potentials appear in the conclusion section.

6.1 Aberration effect of a lens near the focal plane

In an ideal optical system, all rays of light from a point in the object plane would converge to a single point in the image plane, forming a clear image. The influences

which cause different rays to converge to different points are called aberration. In general, the aberration effects are divided into 5 classes as follows:

1) **Spherical aberration**

For lenses made with spherical surfaces, rays which are parallel to the optical axis but at different distances from it fail to converge to the same point. This situation is shown in Fig. 6.1. This effect is more pronounced for lenses with small focal length to aperture size ratio (f-number). In our experiment a lens with a 3.81 cm focal length and 2.54 cm diameter is used to focus the FORT beam. The f-number for this lens was small enough that spherical aberration should be taken into consideration when calculating the trapping potential that will be experienced by the atoms. 2) **Coma**

Coma is an aberration which causes rays from an off-axis point of light in the object plane to create a trailing "comet like" blur directed away from the optical axis. A lens with a large amount of coma may produce a sharp image in the center of the field, but become increasingly distorted toward the edges. Coma is an off-axis aberration which can affect the trapped atoms under certain configurations of the optical trap.

3)**Astigmatism**

Astigmatism is a result of different lens curvatures in different directions. Figure 6.3 shows such a condition for two vertical and horizontal beams. Considering the well developed technology designing the lenses we have not observed any effect on the FORT beam related to astigmatism.

4) **Curvature of field**

Curvature of field causes a planar object to project a curved (nonplanar) image, see Fig. 6.4 for more details.

5)**Chromatic Aberration**

A lens will not focus different colors in exactly the same place because the focal length depends on refractive index which in term depends on the light wavelength. Since we were using light with a single wavelength this aberration was not important.

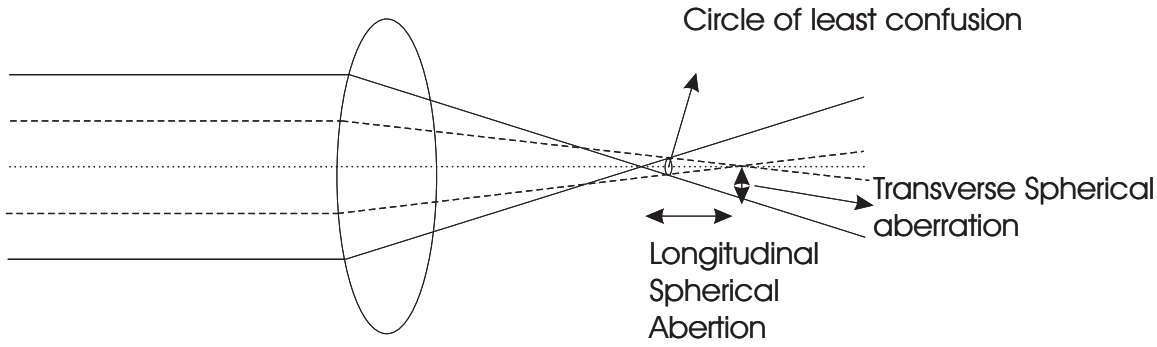

Figure 6.1. Schematic diagram showing the spherical aberration effect on the beam pattern near the focal plane of a lens.

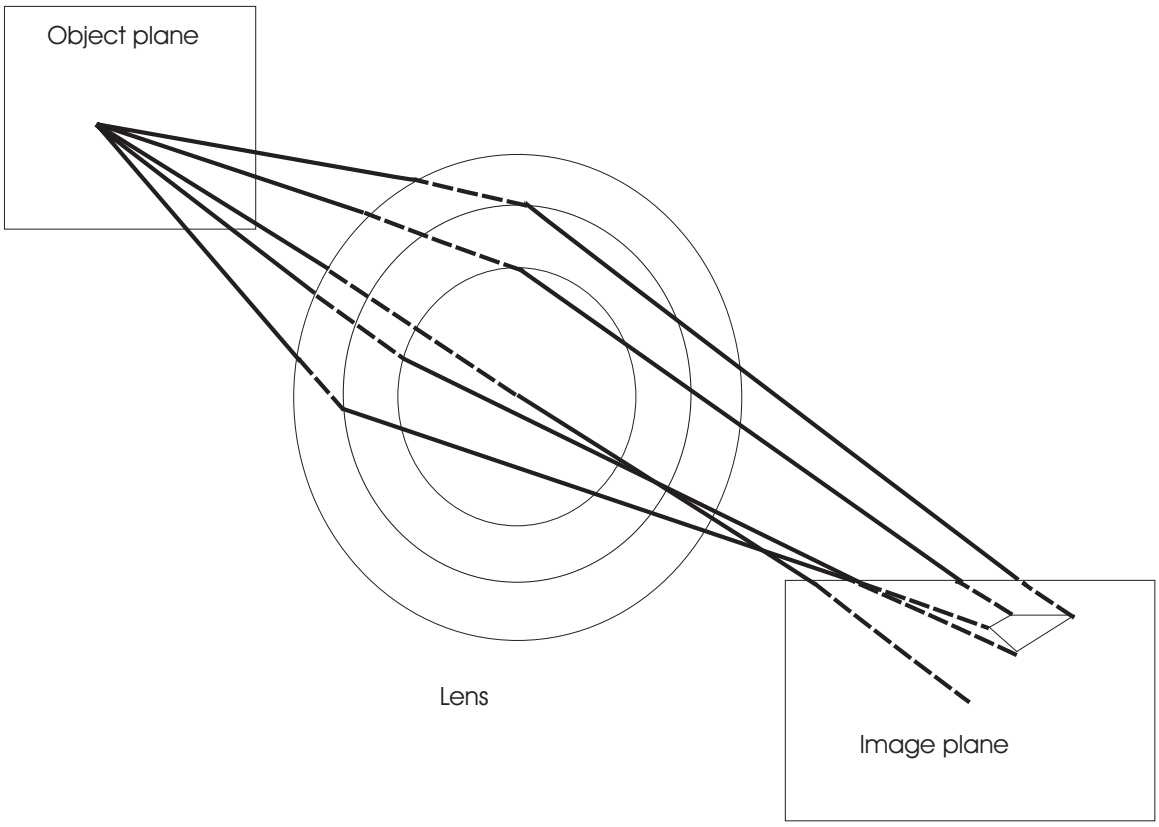

Figure 6.2. Coma effect on beam.

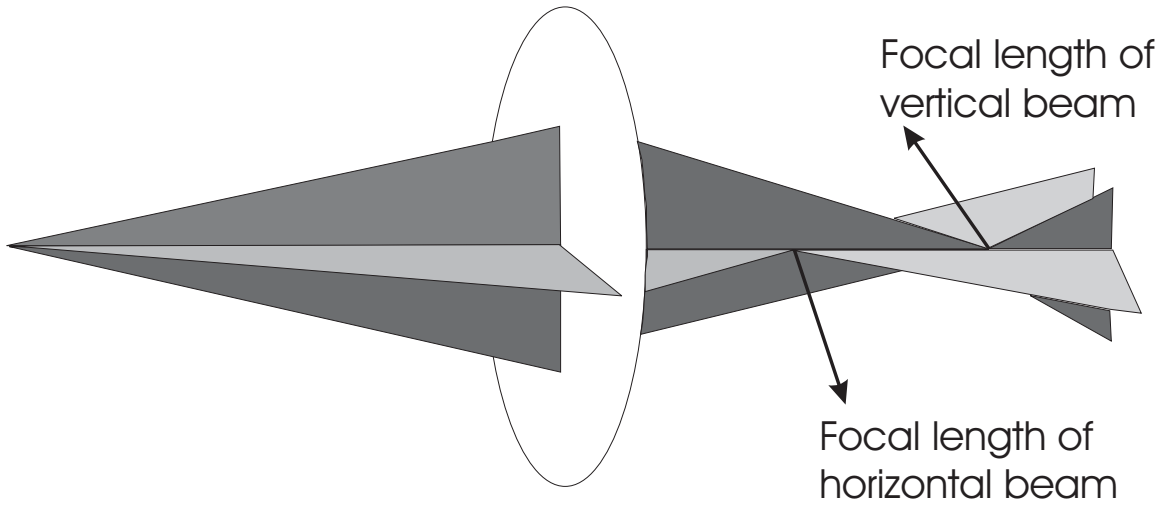

Figure 6.3. Astigmatism.

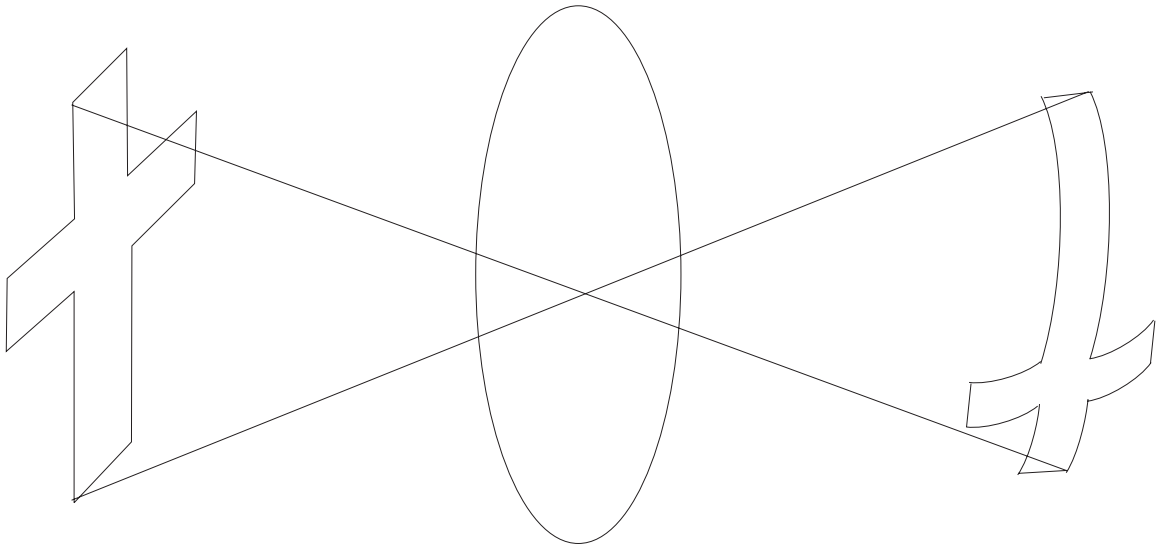

Figure 6.4. Curvature of field.

Although there are well established methods to design aberration-free lenses we would like to use a lens which is not corrected for spherical aberration and show the interesting features of such systems for tailoring optical potentials for atoms.

Since the potential well depth of any FORT is proportional to the intensity and therefore proportional to the electric field component of the laser light squared, $U = -\frac{1}{2}\alpha_g |E|^2$, and it changes in presence of the aberration, we now proceed to calculate the intensity distribution produced near the focus of the lens used in our experiment. As stated previously, for the parameters of our experiment, only spherical aberration and coma can strongly alter the beam pattern. Following Born and Wolf [102] and Yoshida and Asakura [103], the intensity close to the focus of a lens for an incident Gaussian beam is given by,

$$I(u,v) = \frac{1}{w^2}\left|\int_0^1 \rho\, \mathrm{d}\rho\, \mathrm{e}^{\frac{-\rho^2}{(w/a)^2}} \mathrm{e}^{-\mathrm{i}\left(\frac{u\rho^2}{2}+k\beta\rho^4\right)} J_0(v\rho)\right|^2, \tag{6.1}$$

where w is the spot size on the lens and ρ is the radial coordinate on the lens normalized to the radius of the lens, a. v and u are the scaled cylindrical radial and axial coordinates of the image space (with the origin for u at the Gaussian focus) and are given by $v = \frac{2\pi}{\lambda}\frac{a}{R}\sqrt{x^2+y^2}$ and $u = \frac{2\pi}{\lambda}\left(\frac{a}{R}\right)^2 z$. k is the vacuum wave number, given by $k = 2\pi/\lambda$, where λ is the wavelength of the light used. R is the radius of the Gaussian reference sphere from the lens, (x, y) are the cartesian coordinates in the Gaussian image plane and β is the primary spherical aberration coefficient, usually expressed in terms of a number of wavelengths. This coefficient is additive over all the elements used in an optical system. Our set up has three lenses in the path of the laser light (see Fig. 6.5). The first two lenses constitute a telescope and the third one (which is placed inside the vacuum chamber) we refer to as the primary lens.

Using the thin lens approximation, we calculate the primary spherical aberration produced by such a lens of focal length f to be [104],

$$\beta = \frac{w^4}{32f^3}\left[\left(\frac{n}{n-1}\right)^2 + \frac{(n+2)}{n(n-1)^2}\left(B + \frac{2(n^2-1)}{n+2}C\right)^2 - \frac{n}{n+2}C^2\right], \tag{6.2}$$

where n is the refractive index of the lens medium and B is the shape variable given by $B = (c_1 + c_2)/(c_1 - c_2)$ and $c_i = 1/r_i$; $i = 1, 2$; r_i are the radii of curvature of the lens surfaces. C is known as the conjugate variable and is defined as $C = (u_1 + u_2)/(u_1 - u_2)$, where u_1 and u_2 are the divergence angles of the gaussian beam before and after passing through the lens. These angles are given by $u_i = \lambda/\pi w_{0i}$; $i = 1, 2$, where w_{01} and w_{02} are the minimum beam waists of the beam before and after the lens. It should be noted that according to the usual sign convention, if the lens produces a converging beam, then u_2 is negative so that the denominator in the definition of C is not zero in our experiment.

In the experimental situation we wish to model, the separation of the telescope lenses is varied by moving the second lens in the optical system and keeping the other lenses fixed. Thus the first lens of the telescope contributes a constant amount to the total spherical aberration coefficient β as its w and C parameters are fixed. As the position of the second lens in the telescope is moved, the beam size on this lens and on the third (the primary) lens will change resulting in changes to the parameters w and C for these lenses. This leads to a variable contribution to β by these last two lenses and therefore a variable aberration pattern near the focus of the primary lens. We have found that for our experiment the primary spherical aberration of the lens varies from around 0.1 to around 18.2 wavelengths.

6.2 Experimental setup

In the following, we present an experimental setup which enabled us to create the spherical aberration pattern to form a series of micro optical traps. We used the vacuum chamber that is explained in Chapter 4. The primary lens was a meniscus lens with a 3.81 cm focal length and 2.54 cm diameter placed inside the vacuum chamber and is not corrected for spherical aberration*. This lens was mounted such

*Note that for some of the later experiments, this lens was replaced by an aspheric lens

that the convex side was towards the center of the chamber to maximize the spherical aberration effects. Before reaching the primary lens, the CO_2 laser beam passed through the telescope which was composed of two plano convex lenses with 6.35 cm and 12.7 cm focal lengths placed approximately 2 meters away from the chamber. This configuration allowed us to control the beam size at the lens inside the chamber by varying the separation of the telescope lenses. Consequently, we were able to change the spherical aberration pattern close to the gaussian focus.

The CO_2 light was directed into the vacuum system in a geometry such that it propagated at an angle of 45 degrees to the vertical. The total laser power was controlled by passing the CO_2 light through an AOM. The first order of the modulator was then directed into the telescope to expand the beam. The optical arrangement used in this experiment is as shown in Fig. 6.5. For our atomic source we used the MOT with 2×10^7 atoms. The parameters for the MOT were same as the ones explained in Chapter 4. The MOT and FORT were aligned using our method of contrast improvement described in Chapter 4. This is based on improving the contrast between the atoms trapped in the MOT and those trapped in the FORT by increasing the detuning of the MOT light from resonance.

The same method of the Chapter 5 was taken to load the FORT. When imaging the FORT, the CO_2 laser beams were switched off 3.5 ms before the image was taken to allow the cloud of atoms to expand to a size which was significantly above the resolution of the optical system.

6.3 Results and Discussion

Using the procedure described in Section 6.3 we have been able to load several micro-optical traps created by the aberration pattern of the meniscus lens. Interestingly, our observations show that there are approximately ten sites capable of holding the atoms when the beam diameter was similar to the size of the primary lens, which is in very good agreement with our simulation results. For a given amount of spherical

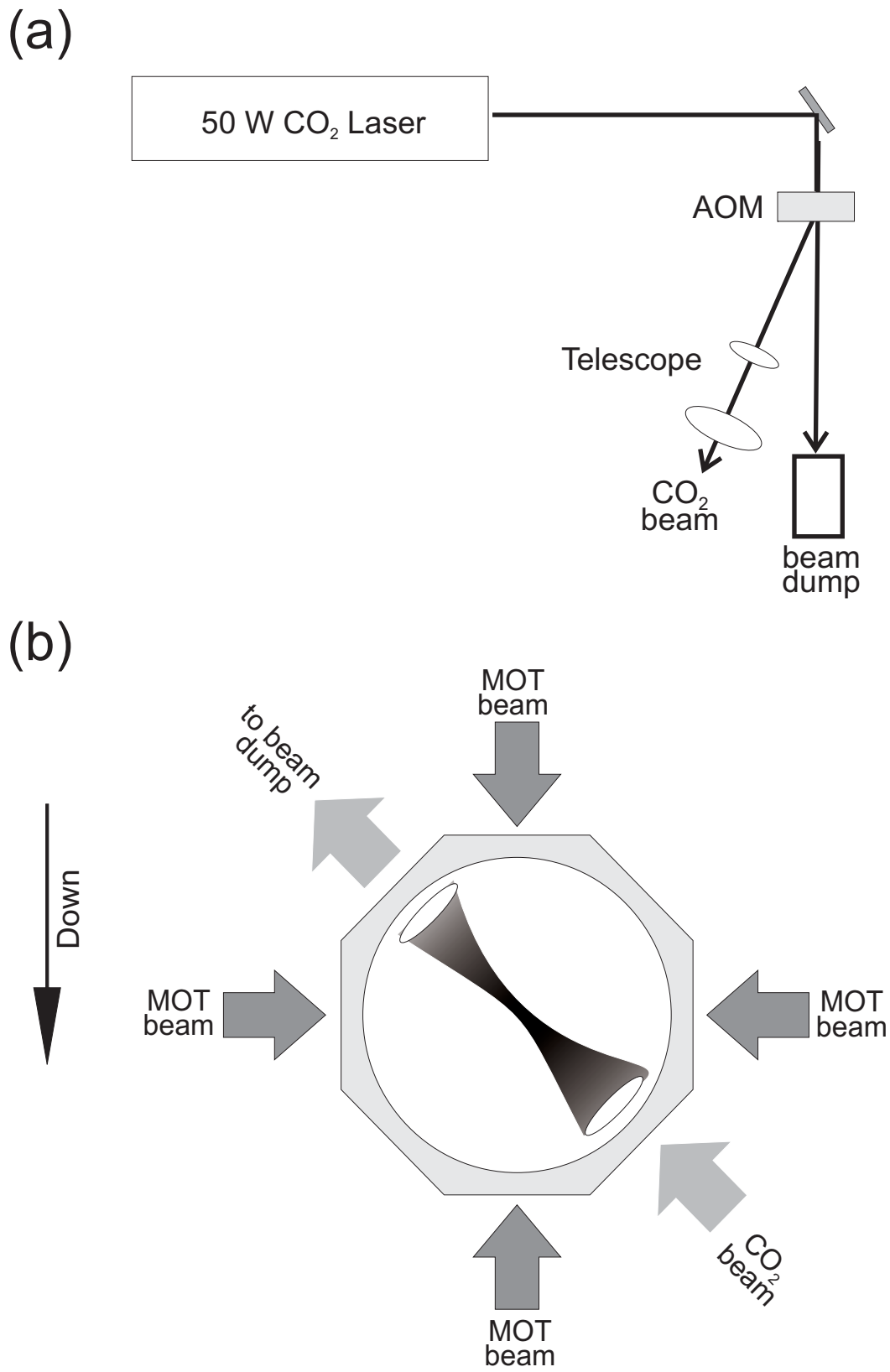

Figure 6.5. Experiment schematic, showing (a) the production of the FORT beams and its path before it enters the chamber, and (b) the beam geometry relative to the vacuum chamber.

aberration β, the separation between the micro-traps decreased as one moved away from the focus and towards the primary lens. Therefore the number of micro-traps being loaded from a MOT at a given time depends where the MOT and FORT overlappshows ed each other. Usually three micro-traps were loaded by placing the atomic cloud of the MOT close to the gaussian focus of the lens. This can be increased to four or five micro-traps by moving the MOT a few millimeters towards the lens (to move the MOT we changed the currents in the nulling coils designed to cancel out stray magnetic fields). Figure 6.6 shows three absorption images of the FORT and the corresponding simulated potentials at two extreme separations of the telescope lenses and one intermediate separation. The lower panels of Fig. 6.6 show that the central FORT and one micro-trap are loaded. This happens when there is higher spherical aberration β. Our simulations show that the separation between the peaks is greater when there is a high spherical aberration. So in the lower panels of Fig. 6.6, the spacial extent of the MOT is such that it could load only one micro-trap along with the central FORT. For the parameters of Fig. 6.6(c), we found from Eq. (6.2) that the spherical aberration β is around 18.2 wavelengths. The middle panel of Fig. 6.6 shows the central FORT and two micro-traps that are loaded when β is around 12.6 wavelengths. In the upper pictures, the spherical aberration is diminished by the small beam size on the primary lens so that only the highly populated central FORT remains. This higher population is due to the fact that for such cases the beam is not focused tightly so that the capture volume of the FORT is increased. In the absence of the spherical aberration the central FORT usually contained over 10^6 trapped atoms. In the presence of spherical aberration, the other micro-traps usually had 2×10^5 atoms at $70\mu K$ temperature.

According to our numerical simulations, the spherical aberration contributions from the telescope lenses can also alter the intensity pattern close to the focal plane of the primary lens. Our telescope lenses are not corrected for spherical aberration.

To demonstrate this point the meniscus lens was replaced with an aspheric lens corrected for spherical aberrations so that the primary lens did not alter the wave front because of the spherical aberration. Different combinations of lenses that made up the telescope were tested, however all of them showed a similar pattern. Thus, here we shall present only one setup in which we used two plano convex lenses, both with 12.7cm focal length. The separation of the telescope lenses was initially set equal to 24cm and was then decreased in 3mm steps. Figure 6.7 shows the observed intensities along the optical axis of the primary lens as the telescope separation was varied. An offset has been added to each profile to improve the readability. The sequence from the top is in order of increasing distance between the telescope lenses. This figure shows that a micro trap is created from the central FORT and starts to move away from it as we increase the separation of the telescope lenses. This is because as the beam size on the second lens increases so does the spherical aberration. From Fig. 6.7 it can be noted that after the seventh step of increment in the telescope separation a second micro-trap emerges from the central FORT and moves away. This happens while the first micro-trap has travelled far enough so that atoms are no longer loaded into it. The second micro-trap moves away with increasing telescope lens separation until the fifteenth step when a third micro-trap emerges from the central trap and starts to travel towards the second micro-trap. These two micro-traps coexist for a few more increments in the separation until the second micro-trap fails to load atoms. Since fewer atoms are loaded into the micro-traps of Fig. 6.7 compared to Fig. 6.6, we infer that the meniscus lens produces more spherical aberration than the telescope lenses.

6.4 Conclusion

We have shown that the intensity distribution produced by a lens that is not corrected for spherical aberration can be used to prepare a potential to realize micro-optical traps. A beam from a CO_2 laser focused with such a lens was employed to

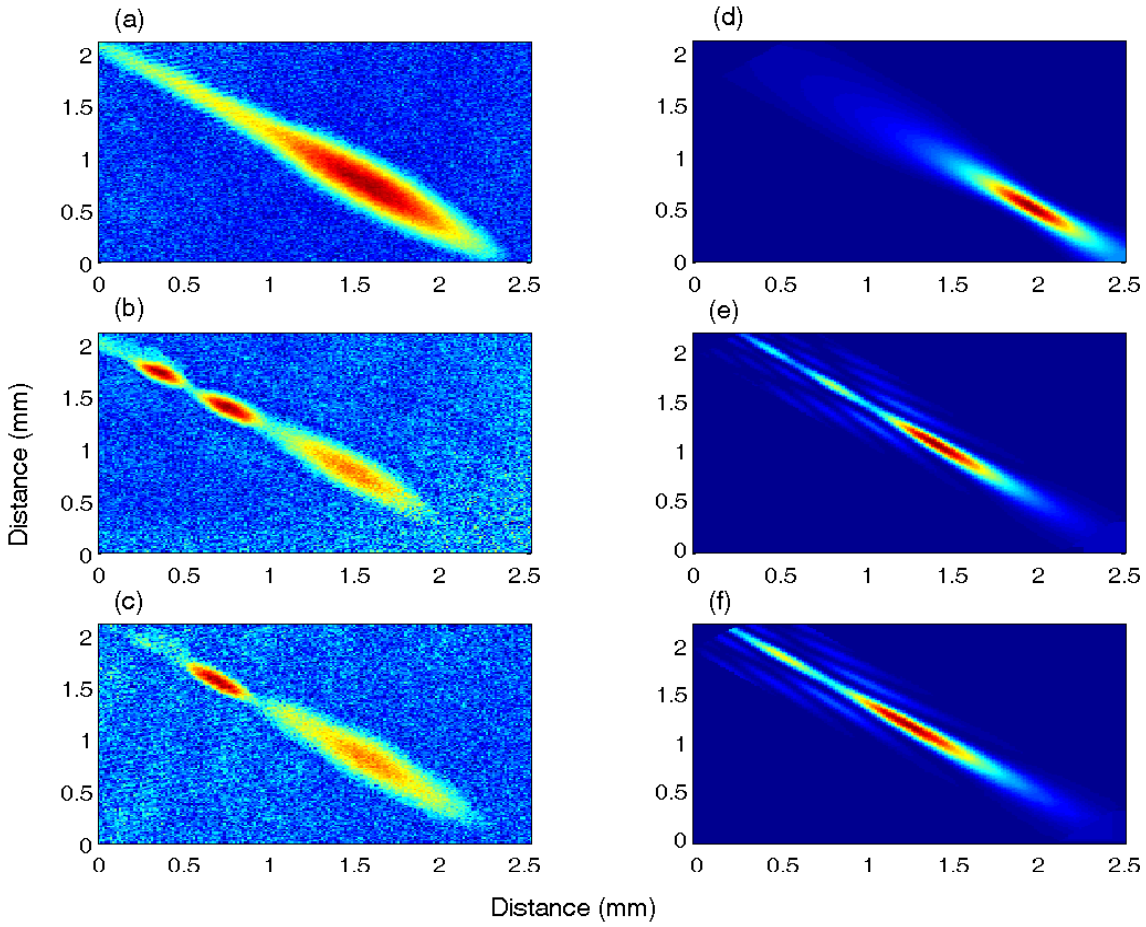

Figure 6.6. Experimental absorption images of the FORT (a), (b) and (c) with corresponding theoretical plots (d), (e) and (f). The abscissa and ordinate are distances in millimeters in each image. (a) and (d) The spherical aberration β is less than a wavelength because of the small size of the CO_2 beam on the primary lens. (b) and (e) The spherical aberration is around 12.6 wavelengths (c) and (f) The beam size on the primary lens is larger and produces strong aberration of around 18.2 wavelengths. Note that atom clouds in the experiment expanded for 3.5 ms before the image was taken.

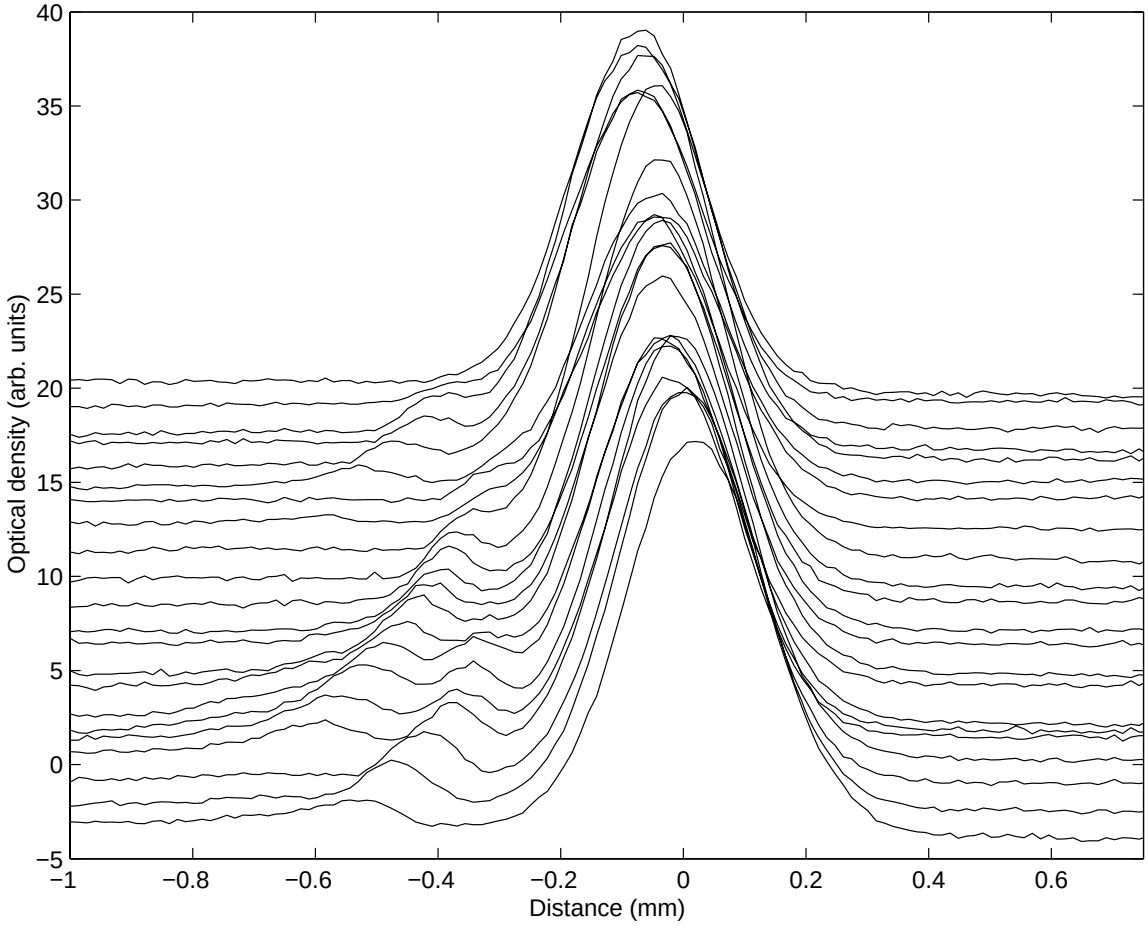

Figure 6.7. Experimentally observed intensity integrated perpendicular to the optical axis when the aberration is only due to the telescope lenses. Each curve is for various telescope lens separations.

load Rb 87 atoms into the micro-optical traps formed by the intensity maxima of the spherical aberration pattern. Such high density (10^{13} atoms/cm^3) samples of cold atoms are of interest for a wide range of experimental studies including evaporative cooling, cold collisions and quantum information processing with ultra cold Rydberg atoms [105]. Furthermore, the variable separation of the micro-traps could be used to control the dipole-dipole interactions between the atoms in adjacent trapping sites. Also increasing the separation of the micro-traps up to a few hundred microns makes the task of individually addressing the different micro-traps relatively straightforward with existing optical techniques. These properties are of great interest for quantum information processing proposals for neutral atoms. Another possible experiment would be to construct an atom interferometer using the micro-traps. One could take a BEC formed using evaporative cooling in a single focused laser beam and then, by changing the separation of the telescope lenses, split off a sub-group of BEC atoms. By simply setting the telescope separation back to the initial value the two BEC components could be recombined making an interference pattern which depends on the phase difference accumulated between the wavefunctions. An analysis of such an interference pattern releases information about the mechanisms affecting the phase of the transported BEC. For example, if the second CO_2 beam propagates in the vertical direction a phase will be induced to the wavefunction proportional to the change in the gravitational potential of the moving group. Therefore the final interference pattern contains information that could be used to probe gravity.

BIBLIOGRAPHY

1. S.N. Bose, Z. Phys. **26**, 178 (1924).

2. A. Einstein, Stizber. Kgl. Preuss. Akad. Wiss. 261 (1924).

3. A. Einstein, Stizber. Kgl. Preuss. Akad. Wiss. 3 (1925).

4. A. Griffin, arXiv:Cond-mat/9901123v1, (1999).

5. A. Migdall, J. Pradan. W. Phillips, T. Bergeman and H. Metcalf, Phys. Rev. Lett. **54** 2596 (1985).

6. S. Chu, J.E. Bjorkholm, A. Shkin, and A. Cable, Phys. Rev. Lett. **57** 314 (1986).

7. E. Rabb, M. Prentiss, A. Cable, S. Chu and D. Pritchard, Phys. Rev. Lett. **59** 2631 (1987).

8. C. Monroe, W. Swann, H. Robinson, and C. Wieman, Phys. Rev. Lett. **65** 1571 (1990).

9. K.B. Davis, M.O. Mewes, M.A. Joffe, and W. Ketterle, in Fourtheenth International Conference on Atomic Physics Boulder , Colorado, 1994, Book of Abstracts, 1M-3.

10. W. Petrich, M.H. Anderson, J.R. Ensher and E.A. Cornell ,in Fourtheenth International Conference on Atomic Physics Boulder , Colorado, 1994, Book of Abstracts, 1M-7.

11. W. Petrich, M.H. Anderson, J.R. Ensher, and E.A. Cornell, Phys. Rev. Lett. **74** 3352 (1995).

12. M.H. Anderson, J.R. Ensher, M.R. Matthews, C.E. Wieman and E.A. Cornell, Science **269** 198 (1995).

13. K.B. Davis, M.-O. Mewes, M.R Andrews, N.J. Van Druten, D.S Durfee, D.M Kurn, and W. Ketterle, Phys. Rev. Lett. **75** 3969 (1995).

14. W.D. Phillips, Rev. Mod. Phys. **70** 721 (1998).

15. E.A. Cornell and C. Weiman, Rev. Mod. Phys. **74** 875 (2002).

16. Paul D. Lett, Richard N. Watts, Christoph I. Westbrook, and William D. Phillips, Phys. Rev. Lett. **61** 169 (1988).

17. A. Aspect, E. Arimondo*, R. Kaiser, N. Vansteenkiste, and C. Cohen-Tannoudji, Phys. Rev. Lett. **61** 826 (1988).

18. M. Kasevich and S. Chu, Phys. Rev. Lett. **69** 1741 (1992).

19. Andrew J. Kerman, Vladan Vuletic, Cheng Chin, and Steven Chu, Phys. Rev. Lett. **84** 439 (2000).

20. Dian-Jiun Han, Steffen Wolf, Steven Oliver, Colin McCormick, Marshall T. DePue, and David S. Weiss, Phys. Rev. Lett. **85** 724 (2000).

21. C.S. Adams, H. Lee, N. Davidson, M. Kasevich, and S. Chu, Phys. Rev. Lett. **74** 3577 (1995).

22. K.M. O'Hara, M.E. Gehm, S.R. Granade, S. Bali, and J.E. Thomas, Phys. Rev. Lett. **85** 2092 (2000).

23. H. Engler, T. Weber, M. Mudrich, R. Grimm, and M. Weidemller, Phys. Rev. A. **62** 031402(R) (2000).

24. Tetsuya Ido, Yoshitomo Isoya, and Hidetoshi Katori, Phys. Rev. A. **61** 061403(R) (2000).

25. D. J. Han, Marshall T. DePue, and David S. Weiss, Phys. Rev. A. **63** 023405 (2001).

26. D.M. Stamper-Kurn, H.-J. Miesner, A.P. Chikkatur, S. Inouye, J. Stenger, and W. Ketterle, Phys. Rev. Lett. **81** 2194 (1998).

27. D.M. Stamper-Kurn, M.R. Andrews, A.P. Chikkatur, S. Inouye, H.-J. Miesner, J. Stenger, and W. Ketterle, Phys. Rev. Lett. **80** 2027 (1998).

28. H.-J. Miesner, D.M. Stamper-Kurn, J. Stenger, S. Inouye, A.P. Chikkatur, and W. Ketterle, Phys. Rev. Lett. **82** 2228 (1999).

29. D.M. Stamper-Kurn, H.-J. Miesner, A.P. Chikkatur, S. Inouye, J. Stenger, and W. Ketterle, Phys. Rev. Lett. **83** 661 (1999).

30. B.P. Anderson and M.A. Kasevich, Science **282** 1686 (1998).

31. M.D. Barrett, J.A. Sauer, and M.S. Chapman, Phys. Rev. Lett. **87** 010404 (2001).

32. Tino Weber, Jens Herbig, Michael Mark, Hanns-Christoph Nägerl, Rudolf Grimm, Science **299** 232 (2003).

33. Toshiya Kinoshita, Trevore Wenger, and David S. Weiss, Phys. Rev. A. **71** 011602(R) (2005).

34. T.W. Hänsch and A.L. Schawlow,Optics Comm. **13** 68 (1975).

35. R. Shankar, "Principles of Quantum mechanics", Plenum publishing group, second edition (1994).

36. Marvin H. Mittleman,"Introduction to the Theory of Laser-Atom Interactions", Plenum Press, (1982).

37. Amnon Yariv, "Quantum electronics", Wiley (1967).

38. Harold J. Metcalf and Peter van der Straten, "Laser Cooling and Trapping", Springer (1999).

39. P. Lett, R. Watts, C. Westbrook, W. Phillips, P. Gould, and H. Metcalf, Phys. Rev. Lett. **61** 169 (1988).

40. J. Dalibard and C. Cohen-Tannoudji, J. Opt. Soc. Am. B **6**, 2023-2045 (1989).

41. P.J. Ungar, D.S. Weiss, S. Chu, and E. Riis, J. Opt. Soc. Am. B **6** 2058-2071 (1989).

42. T. Walker, D. Sesko, C. Wieman, Phys. Rev. Lett. **64** 408 (1990).

43. T. Walker, P. Feng, "Advances in Atomic, Molecular and Optical Physics", vol. 34, edited by B. Bederson and H. Waltter (Academic press, San Diego, 1994) p. 124.

44. Y. Castin, J. Dalibard, and C. Cohen-Tannoudji,"Bose-Einstein Condensation", edited by A. Griffin, D.W. Snoke and S. Stringari (Cambridge University Press, Cambridge, 1995) p.173.

45. H. Hess, Bull. Am. Physc. Soc. **30** 854 (1985).

46. H.F. Hess, Phys. Rev. B. **34** 3476 (1986).

47. H. Hess, G.P. Kochanski, M.J. Doyle, N. Masuhara, D. Kleppner, and T. Greytak, Phys. Rev. Lett. **59** 672 (1987).

48. W. Petrich, M.H. Anderson, J.R. Ensher, and E.A. Cornell, "Fortheenth International Conference on Atomic Physics", Boulder, Colorado, 1994, Book of Abstracts, 1m-7.

49. C.C. Bradly, C.A. Sackett, J.J. Tollet, and R.G. Hulet, Phys. Rev. Lett. **75** 1686 (1995).

50. K.B. Davis, M.-o. Mewes, M.A. Joffe, M.R. Andrews, and W. Ketterle, Phys. Rev. Lett. **74** 5202 (1995).

51. S. Chu, J.E. Bjorkholm, A. Ashkin, and A. Cable, Phys. Rev. Lett. **57** 314 (1986).

52. J.D. Miller, R.A. Cline, and D.J. Heizen, Phys. Rev. A. **47** R4567 (1993).

53. J.M. Doyle, J.C. Sandberg, I.A. Yu, C.L. Cesar, D. Kellepner, and T.J. Greytak, Phys. Rev. Lett. **67** 603 (1991).

54. J.M. Doyle, J.C. Sandberg, I.A. Yu, C.L. Cesar, D. Kellepner, and T.J. Greytak, Phys. B. **13** 194 (1994).

55. O.J. Luiten, M.W. Reynolds, and J.T.M. Walraven, Phys. Rev. A. **53** 381 (1996).

56. K.B. Davis, M.O. Mewes, and W. Ketterle, Appl. Phys. B. **60** 155 (1995).

57. M. Holland, J. Williams, K. Coakley and J. Cooper, Quantum Semiclass. Op. **8** 571 (1996).

58. H. Wu, C.J. Foot, J. Physics. B. **29**, L321 (1996).

59. K.M. O'Hara, M.E. Gehm, S.R. Granade, and J.E. Thomas, Phys. Rev. A. **64**, 051403(R) (2001).

60. Vanderlei Bagnato, David E. Pritchard, and daniel Kleppner, Phys. Rev. A. **835**, 4335 (1987).

61. G. Cennini, G. Ritt, C. Geckeler, and M. Weitz, Appl. Phys. B. **77** 773 (2003).

62. A.L. Fetter and J.D. Walecka, "Quantum theory of many-particle systems", (McGraw-Hill 1998).

63. N.N. Bogoliubov, J. Phys. (USSR) **11** 23 (1947).

64. E.P. Gross, Ann. Phys. (N.Y.) **4** 57 (1958).

65. E.P. Gross, J. Math. Phys. **4** 195 (1963).

66. E.P. Gross, Nuovo Cimento **20** 454 (1961) and L.P. Pitaevskii, So. Phys.-JETP, **13** 451 (1961).

67. L.P. Pitaevskii, So. Phys.-JETP, **13** 451 (1961).

68. M. Edwards and K. Burnett, Phys. Rev. A. **51** 1382 (1995).

69. A.D. Bandrauk and H. Shen, J. Phys. A. **27** 7147 (1994).

70. A.E. Siegman, "Lasers" (University Science Books 1986).

71. K.B. MacAdam, A. Steinback, and C. Wieman, Am. J. Phys. **12** 1098 (1992).

72. Wolfgang Demtroder, "Laser Spectroscopy, Basic Concept and Instrumentation" second edition, (Springer 1998).

73. P. Ahmadi, V. Ramareddy and G.S. Summy, New J. Phys. **7** 4 (2005).

74. W. Ketterle, D.S. Durfee, and D.M. Stamper-Kurn, Making, probing and understanding Bose-Einstein condensates. cond-mat, 9904034v2, (1999).

75. D. Boiron, A. Michaud, J.M. Fournier, L. Simard, M. Spenger, G. Grynberg, and C. Salomon, Phys. Rev. A. **57** R4106 (1998).

76. I.F. Silvera and J.T.M. Walraven, Phys. Rev. Lett. **44** 168 (1980).

77. S.J.M. Kuppens, K.L. Corwin, K.W. Miller, T.E. Chupp, and C.E. Wieman, Phys. Rev. A. **62** 013406 (2000).

78. W. Ketterle, K.B. Davis, M.A. Joffe, A. Martin, and D.E. Pritchard, Phys. Rev. Lett. **70** 2253 (1993).

79. R. Scheunemann, F.S. Cataliotti, T.W. Häsch, and M. Weitz, J. Opt. B. **2** 645 (2000).

80. P.F. Griffin, K.J. Weatherill, S.G. MacLeod, R.M. Potvliege, and C.S. Adams, physics/0504113 (2005).

81. C.S. Adams, H.J. Lee, N. Davidson, M. Kasevich, and S. Chu, Phys. Rev. Lett. **74** 3577 (1995).

82. S. Friebel, C. D'Andrea, J. Walz, M. Weitz, and T.W. Hänsch, Phys. Rev. A. **57** R20 (1998).

83. Y. Takasu,
K. Maki, K. Komori, T. Takano, K. Honda, M. Kumakura, T. Yabuzaki, and Y. Takahashi, Phys. Rev. Lett. **91** 040404 (2003).

84. S.R. Granade, M.E. Gehm, K.M. O'Hara, and J.E. Thomas, Phys. Rev. Lett. **88** 120405 (2002).

85. G. Cennini, G. Ritt, C. Geckeler, and M. Weitz, Phys. Rev. Lett. **91** 240408 (2003).

86. K.M. O'Hara, S.R. Granade, M.E. Gehm, and J.E. Thomas, Phys. Rev. A. **63** 043403 (2002).

87. N. Friedman, L. Khaykovich, R. Ozeri, and N. Davidson, Phys. Rev. A. **61** 031403(R) (2000).

88. V. Milner, J.L. Hanssen, W.C. Campbell, and M.G. Raizen Phys. Rev. Lett. **86** 1514 (2001).

89. K.M. O'Hara, S.R. Granade, M.E. Gehm, T.A. Savard, S. Bali, C. Freed, and J.E. Thomas, Phys. Rev. Lett. **82** 4204 (1999).

90. O. Svelto, 'Principles of lasers', (Plenum Press, New York) 1998.

91. G.K. Brennen, C.M. Caves, P.S. Jessen and I.H. Deutsch, Phys. Rev. Lett. **82** 1060 (1999).

92. D. Boiron, A. Michaud, J.M. Fournier, L. Simard, M. Sprenger, G. Grynberg, and C. Salomon, Phys. Rev. A. **57** R4106 (1998)

93. R. Newell, J. Sebby, and T.G. Walker, Opt. Lett **28** 14 (2003).

94. R. Dumke, M. Volk, T. Müther, F.B.J Buchkremer, G. Birkl, and W. Ertmer, Phys. Rev. Lett. **89** 097903 (2002).

95. G. Birkl, F.B.J. Buchkremer, R. Dumke, and W. Ertmer, Opt. Commun. **191** 67 (2001).

96. F.B.J Buchkremer,R. Dumke, M. Volk, G. Birkl and W. Ertmer, Laser Phys. **12** 736 (2002).

97. S. Peil, J.V. Porto, B.L. Tolra, J.M. Obrecht, B.E. King, M. Subbotin, S.L. Rolston and W.D. Phillips, Phys. Rev. A. **67** 051603 (2003).

98. L.R. Evans and C.G. Morgan, Nature **219** 712 (1968).

99. L.R. Evans and C.G. Morgan, Phys. Rev. Lett. **22**, 1099, (1969).

100. L.M. Smith, J. Opt. Soc. Am. A. **6** 1049 (1989).

101. H.C. Nägerl, D. Leibfried, H. Rohde, G. Thalhammer, J. Eschner, F. Schmidt-Kaler, and R. Blatt, Phys. Rev. A. **60** 145 (1999).

102. M. Born and E. Wolf, "Principles of optics", 7 ed., p.519, 'Cambridge University Press' (1999).

103. A. Yoshida and T. Asakura, Opt. Comm. **25** 133 (1978).

104. W.T. Welfold, "Aberrations of the symmetrical optical system", p.192, (Academic Press, London 1974).

105. M.D. Lukin, M. Fleischhauer, R. Cote, L.M. Duan, D. Jaksch, J.I. Cirac and P. Zoller, Phys. Rev. Lett. **87** 037901 (2001).

VITA

PEYMAN AHMADI

Candidate for the Degree of

Doctor of Philosophy

Thesis: Investigating optical atom traps for Bose-Einstein condensate

Major Field: Physics

Biographical:

Personal Data:Born in Zanjan, Iran, on July 7, 1974, the son of Ali and Rogeyyeh Ahmadi.

Education:Graduated from Shariati High School, Zanjan, Iran in May 1989; received Bachelor of Science degree in Physics from Tabriz University, Tabriz, Iran in May 1996. Received Master of Science degree in Physics from Institute for Advanced Studies in Basic Science, Zanjan, Iran in December 1998. Completed the requirements for the Doctor of Philosophy degree with a major in Physics at Oklahoma State University in July 2006.

Professional Memberships:American Physical Society.

Name: Peyman Ahmadi Date of Degree: July, 2006

Institution: Oklahoma State University Location: Stillwater, Oklahoma

Title of Study: Investigating optical atom traps for Bose-Einstein condensate

Pages in Study: 110 Candidate for the Degree of Doctor of Philosophy

Major Field: Physics

Scope and Method of Study:The purpose of this research was to make a Bose Einstein condensate (BEC) of Rb87 atoms using an all optical method. Specific attention was given to replacing the traditional magnetic traps with dipole traps created by high power, far off resonant CO_2 laser beams (FORT) for trapping and evaporative cooling.

Findings and Conclusions: Three major steps where identified necessary to realize a BEC: a) preparing a source of cold atoms (magneto optical trap (MOT)), b) loading atoms from the MOT to the FORT, c) evaporative cooling the atoms in the FORT to nanoKelvin temperatures. Successful accomplishment of these steps lead us to create BEC. While investigating step b), we found that the power in the CO_2 laser does not affect the FORT population after a certain power is achieved. Also a strong correlation between the CO_2 beam waist and the loading efficiency was observed. These findings led us to employ the concept of a time averaged potential to increase the trap's population. The basic idea was to sweep a tightly focused CO_2 beam while it was overlapped with the MOT. By sweeping the CO_2 beam rapidly, atoms could not react to the beam movement and therefore felt a time-averaged potential. These ideas were supported with the observation of lower temperatures for the trapped atoms in the time-averaged FORTs compared to the atoms trapped in the stationary FORT. By adiabatically damping the sweeping amplitude most of the atoms could be forced to accumulate into a non-time averaged trap with a tight waist. Using this technique a 100% increase in the loading efficiency of the FORT was observed.

Our numerical simulations showed that spherical aberration creates local intensity maxima along the CO_2 beam propagation direction which are capable of trapping atoms. This prediction was confirmed by the experimental observation of well separated micro-optical traps. We found that the separation of the micro-optical traps could be changed making them a suitable system for the study of quantum computation with neutral atoms.

ADVISOR'S APPROVAL Dr. Gil Summy